博士論文

Theoretical Control of Thermal Properties Based on Nanostructure Design

（ナノ構造設計に基づく熱物性の理論的制御）

畑　智行

Theoretical Control of Thermal Properties Based on Nanostructure Design

Tomoyuki Hata

Department of Chemical System Engineering

Graduate School of Engineering

The University of Tokyo

January 2017

PREFACE

Heat has been understood as a form of energy over a long period of researches, conversely meaning that microscopic motion can appear as “microscopic heat”. Motion in nanomaterials consists of various elements, structures, and topologies, which results in unique thermal properties accordingly. While some of them cause material degradation, we can utilize some of the others as new energy sources. Active control of such properties will not only improve the performance of existing nanomaterials but also pioneer new material design, which is a purpose of this thesis “Theoretical Control of Thermal Properties Based on Nanostructure Design”. The survey is especially interested in how nanostructures affect the thermal properties; where the thesis has recourse to computational simulations, providing a direct way to observe both of heat transfer and material structures microscopically. The analysis begins with the simple low-dimensional structures, focusing on the difference between two types of interactions in nanosctuctures, namely, the strong bonded one and the weak long-ranged one. It shows that the combination of two interactions shall lead to new materials with controllable thermal properties, and this guideline is clearly validated with studies of inorganic-organic hybrid structures.

The above overview is introduced in Chapter. 1 of the thesis, and the rest is organized as follows. Chapter 2 introduces a basic concept of phonons related to the lattice thermal conductivity. It also provides detailed information of thermal transport calculations and practical methods used in the following studies. Chapter 3 and Chapter 4 study the thermal effects of bonded and long-ranged interactions respectively, holding up carbon nanotubes as examples. The former investigates single-walled carbon nanotubes and their strained carbon-carbon bonds due to twisted tube

structures, namely, the chirality. The latter describes the study about the thermal properties of double-walled carbon nanotubes affected by the long-ranged inter-layer interactions. The comparison between two researches shows a definite importance of the composite nanostructures, which is validated in Chapter 5 with organic-inorganic hybrid perovskites. Specifically, we can understand the thermal properties of the composites, as the properties characterized by the components are modified by the hybrid interactions systematically. Based on this understanding, Chapter 6 finally develops the thermal design by using the hybrid perovskites with anion substitutions. Chapter 7 summarizes the thesis and proposes future subjects toward general and flexible control of thermal transport phenomena.

This work has been supported by a supervisor, collaborators, current and past members of Yamashita & Ushiyama group. Here I should show acknowledge for them.

I would first like to thank my supervisor, Professor Dr. Koichi Yamashita. He gave me a lot of opportunities to study a wide variety of research field and provided enough time to decide the research topic and direction. It helps me to acquire skills and spirit for reaching in the forefront of material engineering. Special thanks also to Associate Professor Dr. Hiroshi Ushiyama, who guided me in my senior bachelor year and supported my daily life afterwards. Professor Dr. Kazunari Domen, Professor Dr. Atsuo Yamada, Associate Professor Dr. Ryuji Kikuchi, and Professor Dr. Satoshi Watanabe gave me a lot of advices and comments about this thesis as the second examiners.

Most of works in this thesis are supported by the gentle collaborators, who were in Yamashita & Ushiyama group, and would not have been possible without their help and guidance. Dr. Tatsuhiko Ohto, an assistant professor in Osaka University, was my senior. He introduced me to the solid-state physics and studies about transport phenomena. His previous works about electron transport through molecular junctions are definitely arouses my interest and become my motivation

to the first work about the phonon transport in single-walled carbon nanotubes. Dr. Hiroki Kawai in Toshiba Corporate Research & Development Center was also my senior, and gave me a lot of time to discuss about the transport phenomena and computational physics. His careful review of my research often found out significant issues and improved the quality of my works. Dr. Ryota Jono, a project assistant professor in the University of Tokyo, was a researcher in Yamashita & Ushiyama group, and joined the second work about double-walled carbon nanotubes. He taught me how important it is to provide new understandings and viewpoints in research work, and showed practical approaches to do it with working together. His extensive knowledge about molecular dynamics is also conducive to pursue my research, and from this experience I came up with ideas for the succeeded studies. Associate Professor Dr. Giacomo Giorgi in Università degli Studi di Perugia was a senior scientist in the group, and supervising the third work about organic-inorganic hybrid perovskites. He encouraged me to join in the new research topics about perovskites and kept an eye on my progress. Moreover, he introduced me to several Italian researchers, which results in the forth work in this thesis. I also remember well that he treated me kindly when I visited Italy and gave me an opportunity to present my research in Perugia.

I also would like to express my gratitude to the Italian collaborators. Dr. Alessandro Mattoni, a staff researcher in the Cagliari Unit of Istituto Officina dei Materiali, gently accepted my visit and prepared comfortable research environment. He instructed me a way to develop classical potentials and shared leading-edge knowledge with me. Dr. Claudia Caddeo also supported my research in Cagliari. Lively discussion with her about thermal transport is highly suggestive and made me motivated for the mentioned research.

The current and past members of Yamashita & Ushiyama group have supported my works indirectly and my deep appreciation should go to them likewise. Assistant Professor Dr.

Mikiya Fujii provided me many opportunities to discuss about our researches, interesting issues, and about life in Yamashita & Ushiyama group. His advices were sometimes encouraging and at other times severe, from all of which I have learned a lot of things. I was also deeply impressed with his sincerity, honesty, and great zeal both in research and in teaching. Dr. Yasumitsu Suzuki, Dr. Tomotaka Kunisada, Dr. Ayaka Kuroki, and Dr. Eriko Watanabe taught me basics and practical methods of calculations, which helped me a lot to start my works. I want to thank my colleagues: Mr. Katsuhiko Nishimra, Mr. Kenta Tsubakiyama, Mr. Takuya Aoyama, Mr. Yasuyuki Masuda, Mr. Yuhei Shimoda. We joined Yamashita & Ushiyama group at the same period and stimulated each other for a long time. I also thank my juniors: Ms. Ayako Kubo, Mr. Eisuke Kawashima, Mr. Masanori Kaneko, Mr. Rimpei Kindaichi, Mr. Shinagawa Chikashi, Mr. Hiroki Iriguchi, Mr. Ryosuke Kodama, Mr. Shintaro Hatamiya, Mr. Shunsuke Kurahashi, Mr. Tomoshi Imamura, and Mr. Shohei Koda. We spend a lot of time together, which always cheered me up and estranged me from a lorn research life.

Finally, I would like to thank my parents and grandparents for their support.

Tokyo January 2017

Tomoyuki Hata

CONTENTS

CHAPTER 1

GENERAL INTRODUCTION

The complexity for minimum component costs has increased at a rate of roughly a factor of two per year. Certainly over the short term this rate can be expected to continue, if not to increase. Over the longer term, the rate of increase is a bit more uncertain, although there is no reason to believe it will not remain nearly constant for at least ten years. That means by 1975, the number of components per integrated circuit for minimum cost will be 65000. I believe that such a large circuit can be built on a single wafer. — *Gordon Earle Moore*

Since 1947, when the transistor was invented in Bell Laboratories [1], electronic devices based on semiconductors rapidly become popular in our lives. For example, in Japan, a penetration rate of personal computers have reached around 80 %; 100％ for mobile phones; 60 % even for smartphones [2]. Such diffusion of devices are strongly led by industrial development in this field with drastic scaling laws, the most famous of which is “Moore's law” in the epigraph [3]. This suggestion of miniaturization and high integration is found in an article published by Gordon Earle Moore in 1965, and have been a definite goal both of high performance and low cost in all devices. While the development in device design still continue to achieve the scaled goal, it has been getting more and more difficult to do it for recent nanoscale devices. In International Technology Roadmap for Semiconductor 2007 [4], a new chapter is established in order to follow Moore's law by another option, namely, finding or designing new materials with excellent properties. Moreover a next-generation guideline called as “More-than-Moore” is also suggested, where the specialized design meeting respective demands is more emphasized than the simple scaling rules. The biggest

problem in continuous scaling is the fact that associated cost benefit has been reduced. At the moment, further miniaturization can be achieved by suppression of leakage current, low resistivity circuit, accurate switching, power saving, and so forth. The device design necessarily includes more delicate CMOS and memory structures, which needs highly precise lithography technology. Such technical requirement often spoils the cost reduction with scaling. Consequently, Moore's Law is losing its industrial driving force.

Particularly, the leakage current and resistance increase are quite serious. These phenomena result in heating of devices, which causes not only a waste of energy but also unstable operation: material breakage or thermal runaway in the worst case. Unfortunately, the increases of leakage and resistance are inevitably accompanied by reduced area of device layers. Even with functionalized materials, it is hard to solve this problem in terms of the electrical characteristics, which recently gives way to another attempt, viz., thermal design in nanoscale devices. Thermal design means handling of surplus heat; including suppression of temperature increase with facilitating a thermal flow, and protection of vulnerable places with shutting off the flow. At the same time, the surplus heat is the dominant form of waste energy and should be recovered with thermoelectric materials, where temperature differences are converged into electric voltage [5]. Such aggregation and distribution of heat shows diverse requirements of thermal properties, indicating the distinct importance in control and design of materials with desired thermal properties.

In order to do it, we should understand a correlation between material structures and thermal properties. Thermal conductivity is one of typical properties related to the thermal design in devices, and can be found in a diffusion equation of heat called as “Fourier’s law”:

$$J = -\kappa \cdot \Delta T \tag{1.1}$$

where J is the thermal flux, ΔT the temperature difference, and κ the thermal conductivity [6].

Even though Eq. (1.1) seems to be simple, κ are hard to be evaluated directly in experiments, because accurate measurement of thermal flow in materials is unfeasible. Only temperature and its change can be observed. Fourier's law should be deformed by separating heat diffusion into temperature diffusion and specific heat can be written as follows:

$$\frac{\partial T}{\partial t} = -\frac{\kappa}{C\rho}\frac{\partial J}{\partial x} = -\alpha\frac{\partial^2 T}{\partial x^2} \tag{1.2}$$

α is the thermal diffusivity; C is the specific heat, at constant volume in many cases; ρ the density; t the time; x the coordinates of sample materials [6]. α and C are measured separately, from which thermal conductivity can be evaluated. While there are several methods to observe the thermal diffusivity, their basics are common. It means to measure a temperature response to thermal stimulation and calculate diffusivity from the diffusion equation. Detailed methods are still improved, especially in development of non-contact measurement methods such as a thermal reflectance pump-probe method [7]. For specific heat measurements, a differential scanning calorimetry is widely used [8], where specific heat is evaluated indirectly by comparing amounts of heat required to increase temperatures in sample and reference substances. While such useful methods have been proposed, their results often involve unignorable measurement errors and are hindered to determine their properties. Various error factors should be considered: surface or internal roughness of samples, contact areas with heaters, changes of sample structures by temperature fields, and accuracies in fitting of response data. Their effects often get more serious in nanoscale measurements [9]. Although the non-contact methods are expected to reduce the above problems, it is much more difficult to quantify the thermal conductivities with taking account of detailed sample structures. Relationship between the transport properties and material structures are still obscure, not providing enough guidelines in searching or designing new thermal materials.

Evaluating the thermal conductivity by using computational simulations is one of the promising ways to overcome such experimental difficulties. Combination between theoretical and experimental studies would not only achieve the steadfast thermophysical property measuring but also develop an understanding of thermal properties in complex structures. In theory, the thermal conductivity can be separated into two contributions with different carriers.

$$\kappa = \kappa_c + \kappa_l \tag{1.3}$$

where κ_c is called as the electron thermal conductivity indicating the contribution of energy transfer via transports of free electrons, and κ_l is the lattice thermal conductivity corresponding to the effect of lattice vibrations, viz., phonons. The later is rather important in insulators or semiconductors, which are often used in thermal circuits or thermoelectric materials. With the simplest approximation, κ_l can be described as

$$\kappa_l = \frac{N}{3}\overline{C_l v_g^2 \tau} \tag{1.4}$$

where N is the number of phonon modes, C_l the lattice specific heat, v_g the phonons' group velocities, τ the relaxation times, and the superscript line indicates an average for modes [5]. Several computational methods are proposed to calculate κ_l, for example, ones based on the non-equilibrium Green's functions (NEGF), non-equilibrium molecular dynamics (NEMD), Boltzmann equation, and Green-Kubo formula. Each approach has different strong and weak points, and an appropriate choice of them enables us to evaluate the lattice thermal conductivity within a certain degree of accuracy.

With such experimental and theoretical analyses, several practical methods are proposed for effective thermal control. The most direct way is introducing grain boundaries that particularly scatter phonons with long mean free paths [10], and the theoretical approaches revealed that the

average grain size is critical [11]. While this approach generally works well at high temperature, it has little potential for further minute control and severe limitations considering the nanoscaled devices operating at moderate temperature. More suitable one for such applications is focusing on finer design of material structures and Fig. 1-1 shows successful examples. Nanoscaled inclusions into host materials are found to work as effective scattering factors for phonons [12]. Materials with superlattices or nanoparticles also lead to insulate the dominant phonon transport with long wavelength [13, 14]. It is recently found that certain nanostructures called as nanophononic structures introduce localized phonons, which sometimes block other phonons as an avoided crossing [15, 16]. Above approaches are useful indeed, however, they are just auxiliary elaboration, so to speak, superstructures, and the limitations in further improvement are visibly not so distant. At the same time, they are often followed by a high cost and low durability. The original purpose of thermal control is to avoid such drawbacks, and now it should be considered to develop not superstructures but innovative raw materials, with further understanding about what design should suppress or enhance the thermal properties.

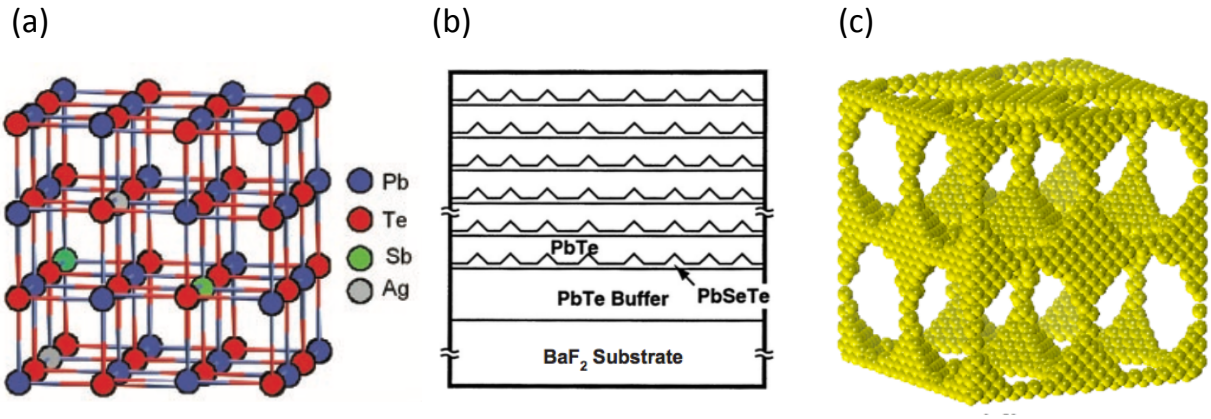

Fig. 1-1. The schematics of nanoscaled thermal control based on (a) the inclusions [12], (b) the superlattices [13], and (c) phonon localizations [15].

Measurements certainly bring us the related properties of materials like κ_l, $\bar{\tau}$, and $\overline{v_g}$, but these values are not directly shows some relationship between their structures. Thermal design of materials now requires how to analyze such relationship and to determine some structural elements that can be control factors of thermal properties [17]. The simplest way to do this is to compare a lot of candidate materials with each other, but a brute force comparison is unrealistic. There are enormous structural factors like chemical bonds, long-range interactions, topology, symmetry, orientation, and order. Moreover, in a lot of materials, these factors are put together and related to each other. To solve this maze of the material structures, we should have some consistent standpoint to compare structures and should choose appropriate comparisons. In general, the prime starting point is referring to preceding studies. Except for the superstructures, we can mainly find two effective approaches, namely, resonant bonding [18, 19] and phonon rattlers [20], shown in Fig. 1-2. The resonant effect indicates that a lack of valence electrons contributing to chemical bonds causes disordered distribution of electrons. Such disorder is observed as weakly delocalized electron density, resulting in strong phonon scatterings. The phonon rattlers mean guest atoms in host-guest structures, whose rattling motions are also known to scatter phonons selectively. Even though we already have the shoulders of giants as the above, such mechanisms are relatively limited to specific compounds and seem to be a little bit narrow as the starting point towards new material design. Therefore, this thesis dares to go back to the basics; we begin with a comparison between simple and pure structures and extend them into more complicated structures step by step. In each stage, we investigate effective analysis methods and structural factors dominant in thermal conductivity, from which we explore a hopeful direction to functionalize materials and establish new set of comparisons. Considering the requirements of various thermal properties as mentioned above, we discuss structure dependence in materials both with high thermal conductivity for

wasting heat and low thermal conductivity for thermoelectric conversion and heat insulation. Such elemental procedures are slow and steady, but should win some development in material design with distinctive findings.

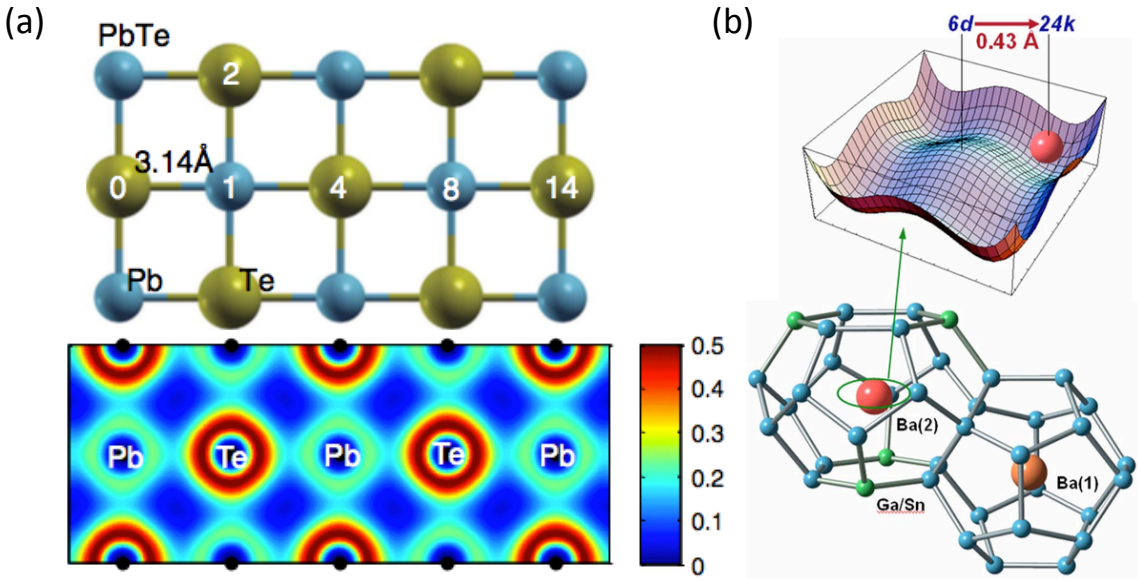

Fig. 1-2. Two approaches for new materials: (a) the resonant bonding in PbTe shows the delocalized electron density [18]; (b) the guest atoms show rattling motions scattering phonons [20].

The rest of this thesis is organized as follows. Chapter 2 introduces a basic concept of phonons related to the lattice thermal conductivity. It also includes detailed information of thermal conductivity calculations, especially about the NEGF and NEMD methods, used in the following chapters. Backgrounds of calculations, first-principles and classical calculations, are also briefly explained. In chapter 3, we investigate the structure dependence in thermal properties of single walled carbon nanotubes, typical examples of simple one-dimensional substances. Their high thermal transport properties are evaluated by the NEGF methods with the first-principles calculations, and compare between them focusing on effects of strained carbon-carbon bonds due to twisted tube structures. Chapter 4 describes a study about thermal properties affected by composite

structures via long-range interactions. We adopt double walled carbon nanotubes and propose a way to control their thermal transport properties at low temperature by using layered structures. The NEGF methods are employed with classical force fields, whose results are analyzed with a coupled vibration model, consisting of two vibrational systems interacted by weak interactions in a non-conducting direction. The analysis suggested the possible requirements for controllable thermal properties, and chapter 5 investigates the organic-inorganic hybrid structures meeting such requirements. In particular, considering the appreciation to thermoelectric materials, we focus on materials with high carrier mobilities and low thermal conductivity, namely, organic-inorganic hybrid perovskites. In order to take into account uncrystallized motion of embedded organic molecules, thermal conductivity is calculated with the classical NEMD with empirical force fields developed by fitting to results in *ab-initio* molecular dynamics. Suppression mechanism of the thermal conductivity is investigated by comparing between several hybrid model structures including organic molecules with different vibrational degrees of freedom. Chapter 6 developed the thermal design based on the hybrid perovskite structures by considering anion substitutions. The parameters of different anions are obtained as simple as possible in order to accept the enormous degrees of freedom for material design with hybrid structures. We propose a three-step procedure with detuning existing parameters, which is validated by comparing with results in experiment and first-principles calculations. With the detuned potential, the effects of anion substitution are investigated in terms of the vibrational properties. Finally in chapter 7, we summarize the guidelines of material design with required thermal properties, and propose future subjects with respect to flexible control of thermal transport phenomena.

Bibliography

[1] Bardeen, J. and Brattain, W.H. (1948). *Three-Electrode Circuit Element Utilizing Semiconductive Materials*. U.S. Patent. No. 2524035.

[2] Economic Research Office, ICT Strategy Policy Division, Global ICT Strategy Bureau, Ministry of Internal Affairs and Communications, Japan. (2015). *White Paper on Information and Communications in Japan*.

[3] Moore, G. E. (1965). Cramming More Components onto Integrated Circuits. *Electronics.* 38: 114–117.

[4] Semiconductor Industry Association. (2007). *The International Technology Roadmap for Semiconductors*.

[5] Ashcroft, N. W. and Mermin, N. D. (1976). *Solid State Physics*. Cengage Learning. ISBN 0030839939.

[6] Carslaw, H. S. and Jaeger, J. C. *Conduction of heat in solid, second edition*. Oxford University Press. ISBN 0198533683.

[7] Cahill, D. G.; Braun, P. V.; Chen, G.; Clarke, D. R.; Fan, S.; Goodson, K. E.; Keblinski, P.; King, W. P.; Mahan, G. D.; Majumdar, A.; Maris, H. J.; Phillpot, S. R.; Pop, E. and Shi, L. (2014). Nanoscale thermal transport. II. 2003–2012. *Appl. Phys. Rev.* 1: 011305.

[8] O'Neill, M. J.; Watson, E. S. (1966). *Differential microcalorimeter.* U.S. Patent. No. 3263484.

[9] Cahill, D. G.; Ford, W. K.; Goodson, K. E.; Mahan, G. D.; Majumdar, A.; Maris, H. J.; Merlin, R. and Phillpot, S. R. (2003). Nanoscale thermal transport. *J. Appl. Phys.* 93: 793-818.

[10] Biswas, K.; He, J.; Blum, I. D.; Wu, C.-I.; Hogan, T. P.; Seidman, D. N.; Dravid, V. P. and Kanatzidis, M. G. (2012). High-performance bulk thermoelectrics with all-scale hierarchical architectures. *Nature* 489: 414–418.

[11] Hori, T.; Shiomi, J. and Dames, C. (2015). Effective phonon mean free path in polycrystalline

nanostructures. *Appl. Phys. Lett.* 106: 171901.

[12] Hsu, K. F.; Loo, S.; Guo, F.; Chen, W.; Dyck, J. S.; Uher, C.; Hogan, T.; Polychroniadis, E. K. and Kanatzidis, M. G. (2004). Cubic $AgPb_mSbTe_{2+m}$: Bulk Thermoelectric Materials with High Figure of Merit. *Science* 303: 818-821.

[13] Harman, T. C.; Taylor, P. J.; Walsh, M. P. and Spears, D. L. (2000). Thermoelectric quantum-dot superlattices with high ZT. *J. Electron. Mater.* 29: L1-L2.

[14] Dresselhaus, M. S.; Chen, G.; Tang, M. Y.; Yang, R. G.; Lee, H.; Wang, D. Z.; Ren, Z. F.; Fleurial, J.-P. and Gogna, P. (2007). New Directions for Low-Dimensional Thermoelectric Materials. *Adv. Mater.* 19: 1043-1053.

[15] Yang, L.; Yang, N. and Li, B. (2014). Extreme Low Thermal Conductivity in Nanoscale 3D Si Phononic Crystal with Spherical Pores. *Nano Lett.* 14: 1734−1738.

[16] Davis, B. L. and Hussein, M. I. (2014). Nanophononic Metamaterial: Thermal Conductivity Reduction by Local Resonance. *Phys. Rev. Lett.* 112: 05505.

[17] Toberer, E. S.; Zevalkink, A. and Snyder, G. J. (2011) Phonon engineering through crystal chemistry. *J. Mater. Chem.* 21; 15843-15852.

[18] Lee, S.; Esfarjani, K.; Luo, T.; Zhou, J.; Tian, Z. and Chen, G. (2014). Resonant bonding leads to low lattice thermal conductivity. *Nat. Commun.* 5: 3525.

[19] Delaire, O.; Ma, J.; Marty, K.; May, A. F.; McGuire, M. A.; Du, M.-H.; Singh, D. J.; Podlesnyak, A.; Ehlers, G.;Lumsden M. D. and Sales B. C. (2011). Giant anharmonic phonon scattering in PbTe. *Nat. Mater.* 10: 614-619.

[20] Avila, M. A.; Suekuni, K.; Umeo, K.; Fukuoka, H.; Yamanaka, S. and Takabatake, T. (2007). $Ba_8Ga_{16}Sn_{30}$ with type-I clathrate structure: Drastic suppression of heat conduction. *Appl. Phys. Lett.* 94: 041901.

CHAPTER 2

THEORY OF THERMAL PROPERTIES

In this chapter, we introduce the computational methods for thermal transport properties with their basic theories. Analytical methods and specific approaches for practical systems in the following researches are explained in the corresponding chapter respectively. In section 2-1, lattice vibrations and phonons are introduced, which are the basic concept in the lattice thermal conduction phenomena.

In the following sections, the practical methods for conductivity are explained. As mentioned in chapter 1, four approaches are mainly used: NEGF, NEMD, Boltzmann equation with the relaxation time approximation [1], and Green-Kubo formula [2]. These methods are classified as Table 2-1, where highlighted ones, viz., NEGF and NEMD are used in the following study. The former is explained in section 2-2, and the later in section 2-3. Here we address the classification a little more in detail. Table 2-1 shows that the thermal transport calculations have two grouping axis, namely, viewpoints of dynamics and temperature environment. The former has the lattice dynamics and molecular dynamics, in other words, vibrations and atomic motions. In the lattice dynamics, thermal transport phenomena are understood as the phonon transports. It means that, the governing equation is the carrier transport equation, which can be simplified as Eq. (1-4). Such equations require the phonon properties of materials including scattering of phonons due to deviation from the harmonic approximation. While scattering events can be statistically analyzed as the group velocity and relaxation time of phonons, the practical calculations require solving phonon many-body problems with perturbative methods, taking a lot of computational costs. This approach is usually difficult to consider large or complex systems with highly scattered phonons, so is suitable to be

applied to materials with high thermal conductivity. On the other hand, the molecular dynamics directly treat the atomic motions under some temperature and heat flow environment. The thermal conductivity is calculated by substituting such motions into Eq. (1-1). This approach does not employ the phonon approximation and natively includes anharmonicity of the energy potential surfaces. While additional analyses often focus on characteristic vibrations with the help of phonon approximation, no perturbative approximation needs to be done basically. Low thermal conductive materials rather require this approach. As the latter axis, the assumption of temperature condition, the equilibrium and non-equilibrium situations will be considered. The equilibrium calculations can be performed with small computational systems and their results are usually stable within thermal fluctuations. The non-equilibrium assumption means that some temperature difference is located in a system. The actual temperature difference makes it easy to consider heterogeneous or uncrystallized systems that often includes defects, substitutions, and interfaces. Computational models should be lager so as not to arise unnaturally steep temperature gradients and temperature jumps, resulting in high calculation costs or unstable results.

Table. 2-1. Two grouping axis in thermal transport calculations.

	Equilibrium	Non-equilibrium
Lattice dynamics	Boltzmann equation [1]	Caroli's formula (NEGF)
Molecular dynamics	Green-Kubo fomula [2]	Fourier's law (NEMD)

The thermal transport calculations presuppose the ways to calculate vibrational properties or atomic motions. Generally speaking, we have two choices; *ab-initio* calculations and classical calculations with empirical force fields. The former evaluates phonons based on the electronic structure calculations, whose results are usually accurate and parameter free; nevertheless it is computationally expensive and unsuitable for large or soft systems. The latter is easy to be applied

to such systems, while its accuracy totally depends on the parameters in force fields. In practice, the *ab-initio* calculations are usually used with lattice dynamics focusing on the accurate calculations of rigid periodic structures. The classical ones cooperate with molecular dynamics for more general systems, such as uncrystallized or composite structures. While the following studies basically accord with this principle, the lattice dynamics calculations for double walled carbon nanotubes are based on the classical potential, considering their computational costs and the authority of developed force fields.

2-1 Phonons

The lattice thermal conduction means energy transfer via vibrational motions of atoms in a crystal lattice. These motions can be separated into isolated characteristic vibrations by the harmonic approximation, and simplified by an artificial periodic boundary condition. When the Schrödinger equation is adopted as the equation of motion, the energies of normal modes are quantized and such quanta are called as phonons. This concept is introduced by Igor Yevgenyevich Tamm in 1930s [3].

We begin with considering the classical motion of atoms in a crystal. Hereafter, $\boldsymbol{R}$ indicates a Bravais lattice point of the crystal, and the most stable point of ith atom in some lattice is described as $\bar{\boldsymbol{r}}_i(\boldsymbol{R})$. At finite temperature, the position of atoms at a certain time, t, are deviated from the most stable points into their surroundings. The actual position is represented by $\boldsymbol{r}_i(\boldsymbol{R}, t)$ and the deviation is $\boldsymbol{c}_i(\boldsymbol{R}, t)$. t dependence is omitted except when the equation of motions are discussed. Atoms in crystal seems to be deeply trapped in the most stable points and it can be assumed that the potential energy, U, can be Taylor expanded about $\boldsymbol{c}_i(\boldsymbol{R}, t)$ as

$$\begin{aligned} U(\boldsymbol{r}_1, \boldsymbol{r}_2, \cdots) &= U(\bar{\boldsymbol{r}}_1, \bar{\boldsymbol{r}}_2, \cdots) + \sum_{(i,\boldsymbol{R})} \boldsymbol{c}_i(\boldsymbol{R}) \cdot \boldsymbol{\nabla} U + \frac{1}{2}\left[\sum_{(i,\boldsymbol{R})} \boldsymbol{c}_i(\boldsymbol{R}) \cdot \boldsymbol{\nabla}\right]^2 U + O(\boldsymbol{u}^3) \\ &\simeq \frac{1}{2}\left[\sum_{(i,\boldsymbol{R})} \boldsymbol{c}_i(\boldsymbol{R}) \cdot \boldsymbol{\nabla}\right]^2 U = U_{harm}, \end{aligned} \tag{2-1}$$

where the origin of the energy is set as the zeroth order term. The first order term should be 0, considering that $\boldsymbol{c}_i(\boldsymbol{R}, t)$ is the deviation from the most stable points. The harmonic approximation indicates that the 3rd and higher order terms can be omitted within a certain accuracy as U_{harm}. The interpretation of this approximation can be understood with the simple example, namely, an ionic crystal or van der Waals' crystal. The potential energy can be described as the summation of the contributions of pairwise interactions $V_{i,j}(\boldsymbol{r}_i(\boldsymbol{R}) - \boldsymbol{r}_j(\boldsymbol{R}'))$ that depend on a distance between

each pair of atoms:

$$U = \frac{1}{2} \sum_{(i,\boldsymbol{R}),(j,\boldsymbol{R}\prime)} V_{i,j} \left(\bar{\boldsymbol{r}}_i(\boldsymbol{R}) - \bar{\boldsymbol{r}}_j(\boldsymbol{R}') + \boldsymbol{c}_i(\boldsymbol{R}) - \boldsymbol{c}_j(\boldsymbol{R}') \right). \tag{2-2}$$

Then we assme that $\boldsymbol{c}_i(\boldsymbol{R}) - \boldsymbol{c}_j(\boldsymbol{R}')$ is small enough to Taylor expand $V_{i,j}(\boldsymbol{r}_i(\boldsymbol{R}) - \boldsymbol{r}_j(\boldsymbol{R}'))$ and only the terms up to the second order are effective. The summation of zeroth order and first order can be omitted as before.

$$\begin{aligned} U_{2nd} &= \frac{1}{4} \sum_{(i,\boldsymbol{R}),(j,\boldsymbol{R}')} \left[\left(\boldsymbol{c}_i(\boldsymbol{R}) - \boldsymbol{c}_j(\boldsymbol{R}') \right) \cdot \boldsymbol{\nabla} \right]^2 V_{i,j} \left(\bar{\boldsymbol{r}}_i(\boldsymbol{R}) - \bar{\boldsymbol{r}}_j(\boldsymbol{R}') \right) \\ &= \frac{1}{4} \sum_{(\alpha,\boldsymbol{R}),(\beta,\boldsymbol{R}\prime)} \left(c_\alpha(\boldsymbol{R}) - c_\beta(\boldsymbol{R}') \right)^2 \left[\boldsymbol{\nabla}^2 V_{i,j} \left(\bar{\boldsymbol{r}}_i(\boldsymbol{R}) - \bar{\boldsymbol{r}}_j(\boldsymbol{R}') \right) \right]_{\alpha,\beta}, \end{aligned} \tag{2-3}$$

where the Cartesian coordinates (x, y, z) of atoms $(i, j, k, \cdots)$ are described as $(\alpha \equiv (i, x), \beta \equiv (i, y), \cdots)$. Eq. (2-3) can be described in terms of the deviation of each atom as the following:

$$\begin{aligned} U_{2nd} &= \frac{1}{2} \sum_{(\alpha,\boldsymbol{R}),(\beta,\boldsymbol{R}\prime)} c_\alpha(\boldsymbol{R})\, D'_{\alpha,\beta}(\boldsymbol{R} - \boldsymbol{R}')\, c_\beta(\boldsymbol{R}') = U_{harm}\,, \\ D'_{\alpha,\beta}(\boldsymbol{R} - \boldsymbol{R}') &= \delta_{\boldsymbol{R},\boldsymbol{R}\prime} \sum_{\boldsymbol{R}\prime\prime} \left[\boldsymbol{\nabla}^2 V_{i,j} \left(\bar{\boldsymbol{r}}_i(\boldsymbol{R}) - \bar{\boldsymbol{r}}_j(\boldsymbol{R}'') \right) \right]_{\alpha,\beta} - \left[\boldsymbol{\nabla}^2 V_{i,j} \left(\bar{\boldsymbol{r}}_i(\boldsymbol{R}) - \bar{\boldsymbol{r}}_j(\boldsymbol{R}') \right) \right]_{\alpha,\beta}. \end{aligned} \tag{2-4}$$

It can be found that the harmonic approximation corresponds to that interactions in crystal are replaced with the coupled harmonic springs.

The atoms in crystal will move according to the equation of motion with the crystal potential under the harmonic approximation. In classical theory, such motions are described as

$$\begin{aligned} \ddot{s}_\alpha(\boldsymbol{R}, t) &= -\sum_{(\beta,\boldsymbol{R}')} D_{\alpha,\beta}(\boldsymbol{R} - \boldsymbol{R}')\, s_\beta(\boldsymbol{R}', t)\,, \\ s_\alpha = \sqrt{m_\alpha} c_\alpha(\boldsymbol{R}, t), &\qquad D_{\alpha,\beta}(\boldsymbol{R} - \boldsymbol{R}') = \frac{1}{\sqrt{m_\alpha m_\beta}} D'_{\alpha,\beta}(\boldsymbol{R} - \boldsymbol{R}'), \end{aligned} \tag{2-5}$$

where m is the atomic mass, and the mass weighted Cartesian coordinates, $s_\alpha(\boldsymbol{R}, t)$, allows us to symmetrize the equations. In the matrix form,

$$\ddot{\boldsymbol{s}}(\boldsymbol{R}, t) = -\sum_{\boldsymbol{R}'} \boldsymbol{D}(\boldsymbol{R} - \boldsymbol{R}')\, \boldsymbol{s}(\boldsymbol{R}', t). \tag{2-6}$$

It is plausible to accept that motions of far distant atoms are close to independent and a terminal condition can be arbitrarily set for mathematical convenience. Here we consider that the motions of atoms in one lattice synchronize with those in the other a certain lattice apart, which is called as Born–von Karman boundary condition. It allows us to make a general solution of Eq. (2-6) as a plane wave, $\boldsymbol{s}(\boldsymbol{R},t)=\boldsymbol{\epsilon}e^{i(\boldsymbol{k}\cdot\boldsymbol{R}-\omega t)}$. ω is the angular frequency, and $\boldsymbol{k}$ the wave vector, which corresponds to a combination of reciprocal lattice vectors. $\boldsymbol{\varepsilon}$ is the polarization vector and indicates changes in the positions of atoms, viz., the vibration amplitude. Substituting this plane wave, Eq. (2-6) is deformed into the following eigenvalue problem:

$$\omega^2\boldsymbol{\epsilon}=\boldsymbol{D}(\boldsymbol{k})\boldsymbol{\epsilon},\qquad \boldsymbol{D}(\boldsymbol{k})=\sum_{\boldsymbol{R}}\boldsymbol{D}(\boldsymbol{R})e^{i\boldsymbol{k}\cdot\boldsymbol{R}}, \tag{2-7}$$

where $\boldsymbol{D}(\boldsymbol{k})$ is the Fourier transform of the mass-weighted Hessian, called as the dynamical matrix. Eq. (2-7) gives $N\cdot M$ eigenmodes for the N-dimensional lattice including M atoms, and solved ω corresponds to the angular frequency of the normal modes. One of the simplest example is the one-dimensional lattice includes two atoms with the same mass. As shown in Fig. 2-1, each of them is only linked with their nearest neighbors by the harmonic interaction with spring constants K_1 and K_2. Then the engenvalue problem is specified as

$$\begin{pmatrix}\omega^2-\frac{1}{m}(K_1+K_2) & \frac{1}{m}(K_1+K_2e^{-ikR})\\ \frac{1}{m}(K_1+K_2e^{ikR}) & \omega^2-\frac{1}{m}(K_1+K_2)\end{pmatrix}\begin{pmatrix}\epsilon_1\\ \epsilon_2\end{pmatrix}=0. \tag{2-8}$$

There are two eigenmodes with two eigenfrequencies, which are given as the functions of the wave vector.

$$\omega_{\pm}=\frac{1}{m}\left(K_1+K_2\pm\sqrt{K_1^2+K_2^2+2K_1K_2\cdot\cos kR}\right), \tag{2-9}$$

which is the dispersion relations of normal modes and can be described in the first Brillouin Zone as Fig. 2-1. The derivations of dispersion relations, $\partial\omega(k)/\partial k$, correspond to the group velocities, v_g,

of characteristic vibrations, which should be 0 on the Brillouin zone boundary and $k = 0$, because the vibrations should be standing wave there due to the Bragg reflection. The exception is the mode with the zero frequency at $k = 0$. This motion corresponds to a uniform translation of the atoms and does not construct a standing wave. Moreover, the frequency of the vibration approaches to 0 linearly, namely, without dispersion. In general, the dispersion relation of the vibrations in the N dimensional lattice including M atoms has the N number of such translational modes, called as acoustic modes. On the other hand, the rest $(N-1) \cdot M$ modes are called as optic modes, because they have higher vibrational energies and often interact with induced electromagnetic waves.

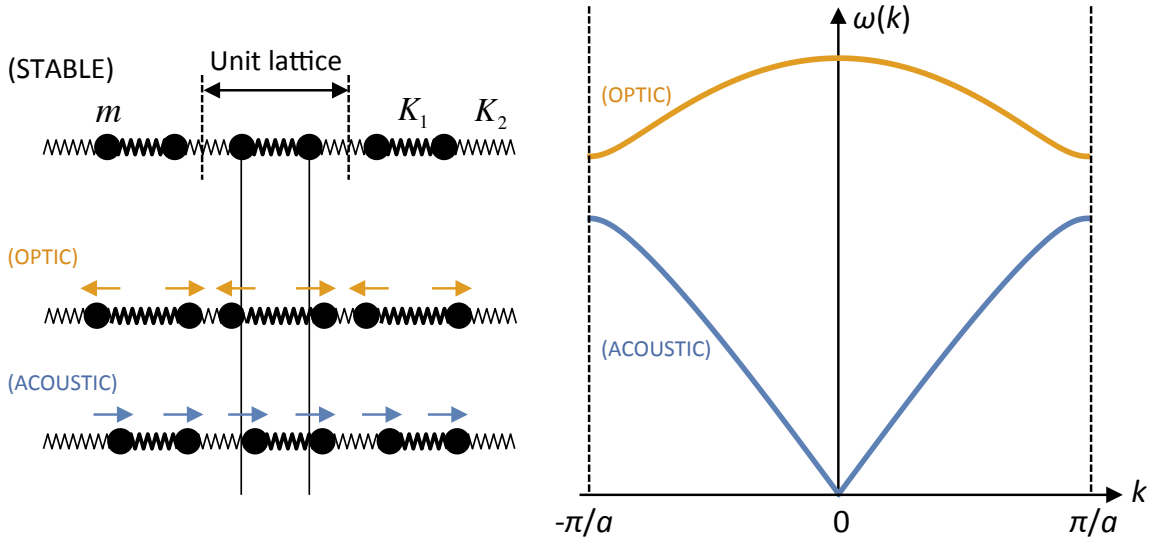

Fig. 2-1. The schematic and dispersion relation of the one dimensional lattice includes two atoms with the same mass. Polarization in each mode is shown as colored arrows.

In quantum mechanics, the Schrödinger equation rather describes the time evolution of the system. By the first or second quantization, the discussion moves from classical mechanics to quantum mechanics, which may be performed at any time of the above procedure. It means that the motion of atoms in the crystal can be directly quantized by substituting quantum harmonic oscillators for classical characteristic vibrations. The Hamiltonian operator of the sth harmonic

oscillator with an angular frequency ω_s is described as

$$\widehat{H}_{harm,s} = \sum_{(i,\boldsymbol{R})} \frac{1}{2m}\hat{p}^2 + \frac{1}{2}m\omega_s\hat{x}^2, \tag{2-10}$$

where $\widehat{H}_{harm,s}$ is the Hamiltonian, $\hat{p}$ the momentum operator, $\hat{x}$ the position operator. The Schrödinger equation with this Hamiltonian can be solved with the following eigenvalues:

$$\langle E\rangle_{harm} = \left(n_s + \frac{1}{2}\right)\hbar\omega_s, \qquad n_s = 0,1,2,\cdots \tag{2-11}$$

where $\langle E\rangle_{harm}$ is the expected value of the energy and $\hbar$ is the Dirac constant. Eq. (2-11) means that, in quantum mechanics, the energy of the simple harmonic oscillation is quantized by the quantum number n_s. In other words, the vibrational amplitude is limited to make a standing wave function in the harmonic potential. Then, we can interpret the quantized harmonic oscillator at n_sth excited state as a model, where the n_s number of some virtual particles with the energy $\hbar\omega_s$ are distributed to the harmonic state. Such virtual particles are called as phonons. It is obviously not restricted that several phonons occupy the same state, indicating that they are governed by the Bose-Einstein statistics. Each normal mode, namely, each line in the dispersion relation is called as the branch of phonons. In some branch, a vibration at some wave vector has an angular frequency $\omega_s(\boldsymbol{k})$, and such specified vibration is called as the mode of phonons. In this picture, the lattice thermal conduction is understood as that phonons with the energies $\hbar\omega_s$ are transported with the group velocities $\partial\omega_s(\boldsymbol{k})/\partial\boldsymbol{k}$. The energy increase is attributed to the increasing number of phonons, and the lattice specific heat C corresponds to the number of phonons introduced per unit temperature increase. Finally the simplified lattice thermal conductivity, Eq. (1-4), is shown again:

$$\kappa_l = \frac{N}{3}\overline{C_l v_g^2\,\tau},$$

Now we can see that the above equation is the average expression of that introduced phonons by temperature increase are transported with corresponding group velocities until they are scattered.

2-2 Non-equilibrium Green's functions

The non-equilibrium lattice dynamics often assume the system, where a thermal conductor is sandwiched between two heat baths (phonon bath) with different temperatures, shown in Fig. 2-2 (a). Here we define the scattering region. This region includes the thermal conductor and parts of heat baths that interact with the conductor effectively. The rest parts of the system are called as the left heat bath region (L) and right heat bath region (R) respectively. The temperatures of the left bath is assumed to be higher than one of the right bath, denoted as $T_L > T_R$. According to the previous section, the energy flows from left to right can be considered as phonon transports. We can estimate the contribution of some phonon mode in the left bath to the heat conduction as

$$J_{L,m}(k) = \hbar\omega_{L,m}(k) \cdot \frac{v_{L,m}(k)}{a} \cdot T\left(\omega_{L,m}(k)\right) \cdot n\left(\omega_{L,m}(k), T_L\right), \tag{2-12}$$

where $J_{L,m}(k)$ is the contribution of a mode in mth branch with a wave vector k, $v_{L,m}$ the group velocity, $\omega_{L,m}(k)$ the angular moment, $T(\omega)$ the transmission coefficient, and a the length of the scattering region. $n\left(\omega_{m,L}(k), T_L\right)$ is the Bose–Einstein distribution function, governing the number of phonons. The flow of all phonons in the left bath, J_L, is calculated by summing up $J_{m,L}(k)$ about modes, resulting in

$$J_L = \frac{1}{2\pi}\int d\omega\hbar\omega \cdot T(\omega) \cdot n(\omega, T_L). \tag{2-13}$$

The total energy flow J is the difference between the phonon flow from the left bath and one from the right bath, given by

$$J = \frac{1}{2\pi}\int d\omega\hbar\omega \cdot T(\omega) \cdot [n(\omega, T_L) - n(\omega, T_R)]. \tag{2-14}$$

Eq. (2-14) is called as the Landauer formula [4]. This formalism is enough to discuss one direction flows but can be generalized for multi-bath systems by defining transmission coefficients between each heat bath, known as the Landauer-Büttiker formula [5]. The thermal conductance is calculated

by dividing Eq. (2-14) with the temperature difference, that requires evaluating the transmission coefficient. The NEGF formalism is one typical solution to this problem. The NEGF can be understood only with the Keldysh formalism [6], but it requires a lot of specific Green's functions. So this time, we begin with evaluating the transmission coefficient in a conventional manner of the scattering problem with the slice model [7]. Next, we introduce the Green's function and relate them to the conventional picture [8]. Finally, the transmission coefficients are described with the Green's functions as the Caroli's formula.

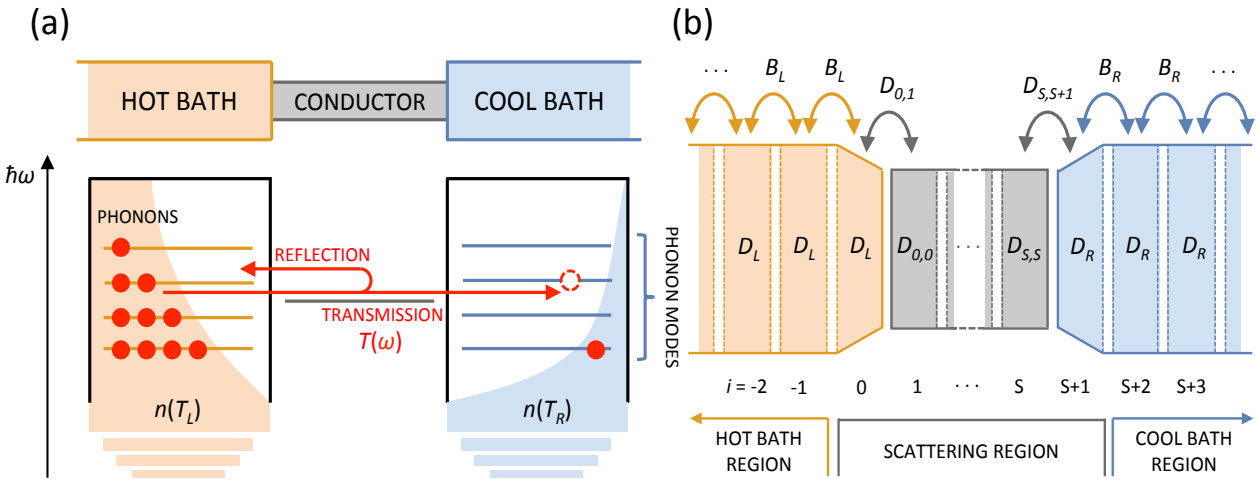

Fig. 2-2. The schematics of (a) the assumed system in the NEGF formalism and (b) the slice model in the scattering problem.

SLICE MODEL The NEGF interprets the sandwiched system as a set of slices divided into vertical like Fig. 2-2 (b). Each slice is given a number i: $i = -\infty, \cdots, -1$ for the left heat bath region; $i = 0, \cdots, S+1$ is the scattering region; $i = S+2, \cdots, \infty$ is the right bath region. Slices of $i = 1, \cdots, S$ is the thermal conductor and ones of $i = 0, S+1$ are the buffer heat bathes. The width of slices are set to interact only with their nearest neighbor slices, and the slices without the thermal conductor are characterized by the ideal periodic potential. We denotes the diagonal dynamical

matrix of the ith slice as $\boldsymbol{D}_{i,i}$, off-diagonal one between the ith and jth slices as $\boldsymbol{D}_{i,j}$. The deviation vector of each atom in the ith slice is described as $\boldsymbol{c}_i$. Under the harmonic approximation, the equations of atomic motions are given by

$$-\boldsymbol{D}_{i,i-1}\boldsymbol{c}_{i-1} + \left(\omega^2\boldsymbol{I} - \boldsymbol{D}_{(L,R)}\right)\boldsymbol{c}_i - \boldsymbol{D}_{i,i+1}\boldsymbol{c}_{i+1} = 0. \tag{2-15}$$

The components in heat bath slices are assumed to be uniform, whose diagonal dynamical matrices are abbreviated as $\boldsymbol{D}_{(L,R)}$ and off-diagonal ones as $\boldsymbol{B}_{(L,R)}$. The widths are also the same, denoted as $a_{(L,R)}$. Then, the equations of motion in the heat bath regions can be rewritten as,

$$-\boldsymbol{B}_{(L,R)}\boldsymbol{c}_{i-1} + \left(\omega^2\boldsymbol{I} - \boldsymbol{D}_{(L,R)}\right)\boldsymbol{c}_i - \boldsymbol{B}^{\dagger}_{(L,R)}\boldsymbol{c}_{i+1} = 0. \tag{2-16}$$

The heat bath region has the periodic structures with period $a_{(L,R)}$, and $\boldsymbol{c}_i$ can be chosen so as to satisfy the Bloch symmetry. It means that $\boldsymbol{c}_i = \lambda\boldsymbol{c}_{i-1} = \lambda^{-1}\boldsymbol{c}_{i+1}$, where $\lambda = e^{iqa}$ is the Bloch factor. When we adopt the Born–von Karman boundary condition considering $2N$ slices, Eq. (2-16) has solutions of the N number of right propagating waves and N left propagating waves. The former is marked with $+$, and the later $-$. With this symmetry, Eq. (2-16) is simplified as

$$\begin{aligned} &-\boldsymbol{B}_{(L,R)}\boldsymbol{u}_{(L,R),n}(\pm) + \left(\omega^2\boldsymbol{I} - \boldsymbol{D}_{(L,R)}\right)\lambda_{(L,R),n}(\pm)\boldsymbol{u}_{(L,R),n}(\pm) \\ &- \boldsymbol{B}^{\dagger}_{(L,R)}\lambda^2_{(L,R),n}(\pm)\boldsymbol{u}_{(L,R),n}(\pm) = 0, \end{aligned} \tag{2-17}$$

where $\lambda_{(L,R),n}(\pm)$ and $\boldsymbol{u}_{(L,R),n}(\pm)$ is the Bloch factor and eigenvectors of the corresponding wave respectively. Since the eigenvectors are nonorthogonal, it is convenient to define dual vectors of $\boldsymbol{u}_n(\pm)$ as

$$\begin{aligned} &\tilde{\boldsymbol{u}}^{\dagger}_n(\pm)\boldsymbol{u}_m(\pm) = \delta_{n,m}, \qquad \boldsymbol{u}^{\dagger}_n(\pm)\tilde{\boldsymbol{u}}_m(\pm) = \delta_{n,m} \\ &\boldsymbol{F}^i(\pm) = \sum_{n=1}^{N} \lambda^i_n(\pm)\boldsymbol{u}_n(\pm)\tilde{\boldsymbol{u}}^{\dagger}_n(\pm), \end{aligned} \tag{2-18}$$

where $\tilde{\boldsymbol{u}}_n(\pm)$ is the dual vector and $\boldsymbol{F}^i(\pm)$ is called as the Bloch matrix, which is a projection matrix onto eigenvectors in an other slice. The equations of motions about the heat baths are

described in terms of the Bloch matrices as follows:

$$-\boldsymbol{B}_{(L,R)}\boldsymbol{F}_{(L,R)}^{-1}(\pm)+\left(\omega^2\boldsymbol{I}-\boldsymbol{D}_{(L,R)}\right)-\boldsymbol{B}_{(L,R)}^{\dagger}\boldsymbol{F}_{(L,R)}(\pm)=0. \tag{2-19}$$

The general solutions are given by

$$\boldsymbol{c}_i=\boldsymbol{c}_i(+)+\boldsymbol{c}_i(-)=\boldsymbol{F}^{i-j}(+)\boldsymbol{c}_j(+)+\boldsymbol{F}^{i-j}(-)\boldsymbol{c}_j(-). \tag{2-20}$$

The slices $i=0,\cdots,S+1$ in the scattering region are not periodic, but it has boundary conditions at $i=0,S+1$, contiguous with the heat bath regions.

$$\begin{gathered}\boldsymbol{c}_{-1}=\boldsymbol{F}_L^{-1}(+)\boldsymbol{c}_0(+)+\boldsymbol{F}_L^{-1}(-)\boldsymbol{c}_0(-)=[\boldsymbol{F}_L^{-1}(+)-\boldsymbol{F}_L^{-1}(-)]\boldsymbol{c}_0(+)+\boldsymbol{F}_L^{-1}(-)\boldsymbol{c}_0,\\ \boldsymbol{c}_{S+2}=\boldsymbol{F}_R(+)\boldsymbol{c}_{S+1}(+)+\boldsymbol{F}_R(-)\boldsymbol{c}_{S+1}(-).\end{gathered} \tag{2-21}$$

The transmission from right to left can be discussed with an assumption, where $\boldsymbol{c}_0(+)$ is the only vibrational source into the thermal conductor. There are no injection from the right heat bath region, namely, $\boldsymbol{c}_{S+1}(-)=0$. Under these conditions, the equations of motion in the scattering region are written as

$$\begin{gathered}-\boldsymbol{D}'_{i,i-1}\boldsymbol{c}_{i-1}+\left(\omega^2\boldsymbol{I}-\boldsymbol{D}'_{i,i}\right)c_i-\boldsymbol{D}'_{i,i+1}\boldsymbol{c}_{i+1}=\boldsymbol{Q}_i\boldsymbol{c}_0(+),\\ \boldsymbol{D}'_{i,j}=\boldsymbol{D}_{i,j},\qquad with\ \{i,j\}\in\{0,1\}\cup\{(1,\cdots,S),(i,i\pm1)\}\cup\{S,S+1\},\\ \boldsymbol{D}'_{0,0}=\boldsymbol{D}_L+\boldsymbol{B}_L\boldsymbol{F}_L^{-1}(-),\\ \boldsymbol{D}'_{S+1,S+1}=\boldsymbol{D}_R+\boldsymbol{B}_R^{\dagger}\boldsymbol{F}_R(+),\\ \boldsymbol{Q}_i=\delta_{i,0}\boldsymbol{B}_L[\boldsymbol{F}_L^{-1}(+)-\boldsymbol{F}_L^{-1}(-)],\end{gathered} \tag{2-22}$$

where $\boldsymbol{c}_{S+1}(+)$ is the transmitted vector, including the information about summed up transmission coefficient via the slices in the scattering region. When the source is simplified as some mode at the left heat bath, $\boldsymbol{c}_0(+)=\boldsymbol{u}_{L,m}(+)$, $\boldsymbol{c}_{S+1}(+)$ is related to the transmission matrix elements $\tau_{n,m}$ as

$$\boldsymbol{c}_{S+1}(+)=\sum_{n=1}^{N}\boldsymbol{u}_{R,n}(+)\tau_{n,m}. \tag{2-23}$$

We should note that the transmission coefficients in the Landauer formula do not directly correspond to $\tau_{n,m}$, because the former is not about the wave amplitude but about the current

amplitude. It means that the elements in Eq. (2-23) should be scaled by the group velocities in the conducting direction and the widths of slices [9].

$$t_{n,m} = \sqrt{\frac{v_{R,n}(+)a_L}{v_{L,m}(+)a_R}}\tau_{n,m}, \qquad T = \sum_{n,m} |t_{n,m}|^2, \tag{2-24}$$

where $v_{(L,R),n}$ is the group velocity of the nth phonon mode in the left or right heat bath region. It is convenient to define the following two velocity matrices. One $\boldsymbol{V}_R(+)$ is the singular diagonal matrix that has $v_{R,n}/a_R$ on the elements about right propagating waves. The other $\widetilde{\boldsymbol{V}}_L(+)$ has $a_L/v_{L,n}$ on the left propagating elements because propagating direction is inverse in Eq. (2-24). With these matrices, the scaled transmission matrix can be described as

$$\boldsymbol{t} = \boldsymbol{V}_R^{1/2}(+)\boldsymbol{\tau}\widetilde{\boldsymbol{V}}_L^{1/2}(+). \tag{2-25}$$

The transmission coefficient in the Landauer formula is given by

$$T = \mathrm{Tr}[\boldsymbol{t}^\dagger \boldsymbol{t}] = \mathrm{Tr}\left[\boldsymbol{\tau}^\dagger \boldsymbol{V}_R(+)\boldsymbol{\tau}\widetilde{\boldsymbol{V}}_L(+)\right]. \tag{2-26}$$

GREEN'S FUNCTION We define the Green's functions for the equations of motion about the slice model. According to the Keldysh Green's function formalism, the retarded Green's functions $\boldsymbol{G}^r$ satisfy the following equations:

$$-\boldsymbol{D}_{i,i-1}\boldsymbol{G}^r_{i-1,j} + \left[(\omega^2 + i\eta)\boldsymbol{I} - \boldsymbol{D}_{i,i}\right]\boldsymbol{G}^r_{i,j} - \boldsymbol{D}_{i,i+1}\boldsymbol{G}^r_{i+1,j} = \boldsymbol{I}\delta_{i,j}\,, \tag{2-27}$$

where $\boldsymbol{G}^r(\omega)$ has singularities around their eigenvalues ω_s, like a pole of $1/(\omega^2 - \omega_s^2)$. With the infinitesimal imaginary part $i\eta$, such functional forms can be Fourier transformed from energy to time as step functions. The retarded Green's function corresponds to the evolution of vibrations from the ith slice to jth slice forward in time. Inversely, adding an negative imaginary part as $\omega^2 - i\eta$ results in the evolution backward in time with an inverted step function. This function is called as the advanced Green's function, denoted as $\boldsymbol{G}^a$. Moreover, the imaginary part of the

Green's function is corresponds to the vibrational density of states. It can be easily understood, considering $\mathrm{Im}[1/(\omega^2-\omega_s^2+i\eta)] \longrightarrow \delta(\omega^2-\omega_s^2)$ with $i\eta \longrightarrow 0$ [10].

We begin with the isolated nth slice with the Green's function $\boldsymbol{G}^{0,r}$, and estimate the effects of a new $n+1$th slice added as the neighbor on the right as shown in Fig. 2-3. The retarded Green's function of the system is expressed as

$$\begin{aligned}\boldsymbol{G}^r &= \begin{pmatrix} \boldsymbol{G}^r_{n,n} & \boldsymbol{G}^r_{n,n+1} \\ \boldsymbol{G}^r_{n+1,n} & \boldsymbol{G}^r_{n+1,n+1} \end{pmatrix} = \begin{pmatrix} (\omega^2+i\eta)\boldsymbol{I}-\boldsymbol{D}_{n,n} & -\boldsymbol{D}_{n,n+1} \\ -\boldsymbol{D}_{n+1,n} & (\omega^2+i\eta)\boldsymbol{I}-\boldsymbol{D}_{n+1,n+1} \end{pmatrix}^{-1} \\ &= \begin{pmatrix} \left[\boldsymbol{G}^{0,r}_{n,n}\right]^{-1} & -\boldsymbol{D}_{n,n+1} \\ -\boldsymbol{D}_{n+1,n} & \left[\boldsymbol{G}^{0,r}_{n+1,n+1}\right]^{-1} \end{pmatrix}^{-1}. \end{aligned} \tag{2-28}$$

The above equation gives the Green's function of the $n+1$th slice as

$$\boldsymbol{G}^r_{n+1,n+1} = \left[\left[\boldsymbol{G}^{0,r}_{n+1,n+1}\right]^{-1} - \boldsymbol{D}_{n+1,n}\boldsymbol{G}^{0,r}_{n,n}\boldsymbol{D}_{n+1,n}\right]^{-1}. \tag{2-29}$$

By repeating the above procedure, the effective dynamical matrix for an added new slice is gradually converged, and then the Green's function of the added slice is also converged. The converged one describes the propagating waves at the surface of the semi-infinite slices facing to the right, like the left heat bath region. It is called as the left surface Green's function $\boldsymbol{g}^r_L$, which is given by

$$\boldsymbol{g}^r_L = \left[(\omega^2+i\eta)\boldsymbol{I}-\boldsymbol{D}_L-\boldsymbol{B}_L\boldsymbol{g}^r_L\boldsymbol{B}^\dagger_L\right]^{-1} = [(\omega^2+i\eta)\boldsymbol{I}-\boldsymbol{D}_L-\boldsymbol{\Sigma}^r_L]^{-1}, \tag{2-30}$$

where $\boldsymbol{\Sigma}^r_L$ is the self-energy, defined as the perturbation to the dynamical matrix of the isolated slice. Similarly by adding new slices on the left, we can calculate the right surface Green's function $\boldsymbol{g}^r_R$ with the self-energy $\boldsymbol{\Sigma}^r_R$:

$$\boldsymbol{g}^r_R = \left[(\omega^2+i\eta)\boldsymbol{I}-\boldsymbol{D}_R-\boldsymbol{B}^\dagger_R\boldsymbol{g}^r_R\boldsymbol{B}_R\right]^{-1} = [(\omega^2+i\eta)\boldsymbol{I}-\boldsymbol{D}_R-\boldsymbol{\Sigma}^r_R]^{-1}. \tag{2-31}$$

Moreover, we can extend the above method to arbitrary perturbations, resulting in the recursive relationship of the Green's function called as the Dyson equation.

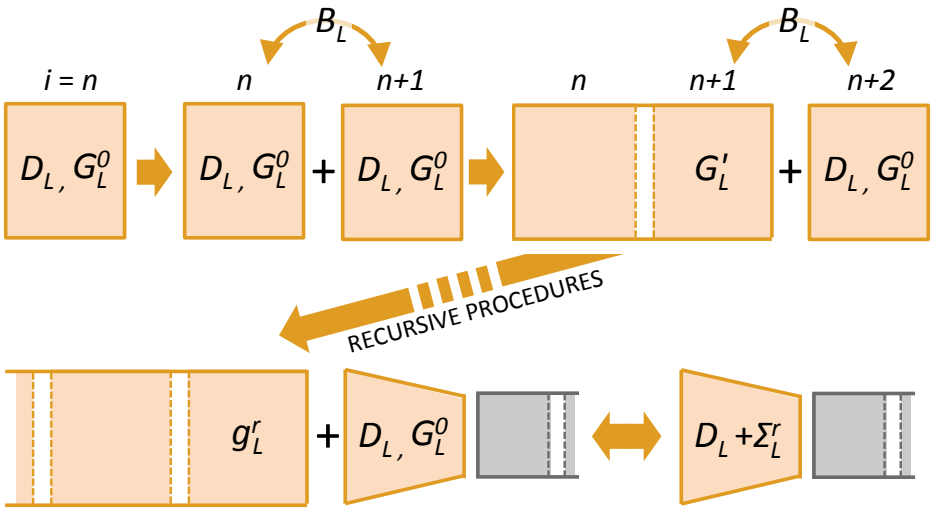

Fig. 2-3. The recursive procedure for the surface Green's function of the left heat bath region, which can truncate the semi infinite system as the self energy

$$\boldsymbol{G}^r_{i,j} = \boldsymbol{G}^{0,r}_{i,j} + \sum_{k,l} \boldsymbol{G}^r_{i,k}\boldsymbol{V}_{k,l}\boldsymbol{G}^{0,r}_{l,j}. \tag{2-32}$$

With these surface Green's functions, Eq. (2-27) can be rewritten ostensibly only about the scattering regions:

$$\begin{gathered} -\boldsymbol{D}''_{i,i-1}\boldsymbol{G}^r_{i-1,j} + \left[(\omega^2 + i\eta)\boldsymbol{I} - \boldsymbol{D}''_{i,i}\right]\boldsymbol{G}^r_{i,j} - \boldsymbol{D}''_{i,i-1}\boldsymbol{G}^r_{i+1,j} = \boldsymbol{I}\delta_{i,j}, \\ \boldsymbol{D}''_{i,j} = \boldsymbol{D}_{i,j}, \qquad with\ \{i,j\} \in \{0,1\} \cup \{(1,\cdots,S),(i,i\pm1)\} \cup \{S,S+1\}, \\ \boldsymbol{D}''_{0,0} = \boldsymbol{D}_L + \boldsymbol{B}_L\boldsymbol{g}^r_L\boldsymbol{B}^\dagger_L, \\ \boldsymbol{D}''_{S+1,S+1} = \boldsymbol{D}_R + \boldsymbol{B}^\dagger_R\boldsymbol{g}^r_R\boldsymbol{B}_R, \end{gathered} \tag{2-33}$$

where we set the surface of the infinite heat baths as the 0th and $S+1$th slices. Now we can discuss the relation ship between the Green's functions and the scattering picture. In terms of the Green's functions, the equations of motion in the ideal infinite heat bath can be described as

$$-\boldsymbol{B}_{(L,R)}\boldsymbol{G}^{b,r}_{i-1,j} + \left[(\omega^2 + i\eta)\boldsymbol{I} - \boldsymbol{D}_{(L,R)}\right]\boldsymbol{G}^{b,r}_{i,j} - \boldsymbol{B}^\dagger_{(L,R)}\boldsymbol{G}^{b,r}_{i+1,j} = \boldsymbol{I}\delta_{i,j}, \tag{2-34}$$

where superscript b indicates the heat bath. $\boldsymbol{G}^{b,r}_{i,j}$ indicates the propagation from the jth slice to ith and the vibrations in each slice satisfy the Bloch symmetry, resulting in that $\boldsymbol{G}^{b,r}_{i,j}$ also follows a

similar projecting relation:

$$\begin{aligned} \boldsymbol{G}_{i,j}^{b,r} &= \boldsymbol{F}^{i-j}(-)\boldsymbol{G}_{j,j}^{b,r}, \qquad with\ i < j, \\ \boldsymbol{G}_{i,j}^{b,r} &= \boldsymbol{F}^{i-j}(+)\boldsymbol{G}_{j,j}^{b,r}, \qquad with\ i > j. \end{aligned} \tag{2-35}$$

Now Eq. (2-34) can be simplified as

$$\begin{aligned} &\left[-\boldsymbol{B}_{(L,R)}\boldsymbol{F}_{(L,R)}^{-1}(-) + \left[(\omega^2 + i\eta)\boldsymbol{I} - \boldsymbol{D}_{(L,R)}\right] - \boldsymbol{B}_{(L,R)}^{\dagger}\boldsymbol{F}_{(L,R)}(+)\right]\boldsymbol{G}_{j,j}^{b,r} = \boldsymbol{I} \\ &\Leftrightarrow \left[\boldsymbol{G}_{j,j}^{b,r}\right]^{-1} = \boldsymbol{B}_{(L,R)}\left[\boldsymbol{F}_{(L,R)}^{-1}(+) - \boldsymbol{F}_{(L,R)}^{-1}(-)\right] = \boldsymbol{B}_{(L,R)}^{\dagger}\left[\boldsymbol{F}_{(L,R)}(-) - \boldsymbol{F}_{(L,R)}(+)\right] \\ &\Leftrightarrow \left[\boldsymbol{G}_{0,0}^{b,r}\right]^{-1} = \boldsymbol{Q}_0. \end{aligned} \tag{2-36}$$

Such amplitude transfer between slices also can be applied to semi infinite heat bath, and the equations of motion at $\{i,j\} \in \{0,0\}$ and $\{-1,0\}$ can be expressed as the following:

$$\begin{aligned} \left[-\boldsymbol{B}_L\boldsymbol{F}_L^{-1}(-) + \left[(\omega^2 + i\eta)\boldsymbol{I} - \boldsymbol{D}_L\right]\right]\boldsymbol{g}_L^r &= \boldsymbol{I}, \\ \left[-\boldsymbol{B}_L\boldsymbol{F}_L^{-1}(-) + \left[(\omega^2 + i\eta)\boldsymbol{I} - \boldsymbol{D}_L\right]\right]\boldsymbol{F}_L^{-1}(-)\boldsymbol{g}_L^r &= \boldsymbol{B}_L^{\dagger}\boldsymbol{g}_L^r. \end{aligned} \tag{2-37}$$

The above equations allow us to describe the surface Green's functions and self-energies in the scattering picture, in other words, with the Bloch matrices and dynamical matrices:

$$\boldsymbol{g}_L^r = \boldsymbol{F}_L^{-1}(-)\left[\boldsymbol{B}_L^{\dagger}\right]^{-1}, \qquad \boldsymbol{\Sigma}_L^r = \boldsymbol{B}_L\boldsymbol{F}_L^{-1}(-). \tag{2-38}$$

The same procedures can be applied to the equations of motion at $\{i,j\} \in \{S+1, S+1\}$ and $\{S+1, S+2\}$, resulting in

$$\boldsymbol{g}_R^r = \boldsymbol{F}_R(+)\boldsymbol{B}_R^{-1}, \qquad \boldsymbol{\Sigma}_R^r = \boldsymbol{B}_R^{\dagger}\boldsymbol{F}_R(+). \tag{2-39}$$

We can build a similar relation ship between the advanced Green's function and the propagating waves. In order to do this, the following advanced Bloch matrix $\boldsymbol{F}^a(\pm)$ is defined:

$$\boldsymbol{F}^a(\pm) = \sum_{n=1}^{N} \lambda_n(\mp)\boldsymbol{u}_n(\mp)\tilde{\boldsymbol{u}}_n(\mp) = \sum_{n=1}^{N} \lambda_n^a(\pm)\boldsymbol{u}_n^a(\pm)\tilde{\boldsymbol{u}}_n^a(\pm). \tag{2-40}$$

With $\boldsymbol{F}^a(\pm)$, it is found that the advanced Green's functions follow the projecting relation as

$$\boldsymbol{G}_{i,j}^{b,r} = \left[\boldsymbol{G}_{j,i}^{b,a}\right]^{\dagger} = \boldsymbol{G}_{j,j}^{b,r}[\boldsymbol{F}^{a\dagger}(+)]^{j-i}, \qquad with\ i < j,$$
$$\boldsymbol{G}_{i,j}^{b,r} = \left[\boldsymbol{G}_{j,i}^{b,a}\right]^{\dagger} = \boldsymbol{G}_{j,j}^{b,r}[\boldsymbol{F}^{a\dagger}(-)]^{j-i}, \qquad with\ i > j. \tag{2-41}$$

Considering the surface of the semi-infinite heat bathes, the advanced surface Green's functions are given by

$$\boldsymbol{g}_L^a = [\boldsymbol{F}_L^a(-)]^{-1}\left[\boldsymbol{B}_L^{\dagger}\right]^{-1}, \qquad \boldsymbol{g}_R^a = \boldsymbol{F}_L^a(+)\boldsymbol{B}_R^{-1}. \tag{2-42}$$

Comparing between Eq. (2-38), (2-39), and (2-42), the retarded Bloch matrices are related to the advanced one as

$$\boldsymbol{B}^{\dagger}\boldsymbol{F}(\pm) = \boldsymbol{F}^{a\dagger}(\pm)\boldsymbol{B}. \tag{2-43}$$

We can also rewrite the Dyson equation with the Bloch matrix as

$$\boldsymbol{G}_{i,0}^{r} = \boldsymbol{G}_{i,0}^{b,r} + \sum_{j,k} \boldsymbol{G}_{i,j}^{r}\boldsymbol{V}_{j,k}\boldsymbol{G}_{k,0}^{b,r} = \left[\boldsymbol{F}_L^{i}(+) + \sum_{j,k} \boldsymbol{G}_{i,j}^{r}\boldsymbol{V}_{j,k}\boldsymbol{F}_L^{k}(+)\right]\boldsymbol{G}_{i,0}^{b,r}. \tag{2-44}$$

CAROLI'S FORMULA We should rewrite the transmission matrix in terms of the Green's function. As the first step, the elements of the matrix can be discussed by simplifying the vibrational source as a mode at the left heat bath $\boldsymbol{u}_{L,m}(+)$ like the above discussion. The Lippmann-Schwinger equation shows that the transmitted wave can be described as the sum of the source and scattered vibrations:

$$\boldsymbol{c}_i = \boldsymbol{u}_{L,m,i}(+) + \sum_{j,k} \boldsymbol{G}_{i,j}^{r}\boldsymbol{V}_{j,k}\boldsymbol{u}_{L,m,k}(+) = \left[\boldsymbol{F}_L^{i}(+) + \sum_{j,k} \boldsymbol{G}_{i,j}^{r}\boldsymbol{V}_{j,k}\boldsymbol{F}_L^{k}(+)\right]\boldsymbol{u}_{L,m}(+), \tag{2-45}$$

where $\boldsymbol{u}_{L,m,i}(+)$ indicates the source is transferred from the 0th slice to ith without scattering, namely the reference wave. With Eqs. (2-43) and (2-44), the scatted wave $\boldsymbol{c}_i$ is given by,

$$\boldsymbol{c}_i = \boldsymbol{G}^r_{i,0}\left[\boldsymbol{G}^{b,r}_{0,0}\right]^{-1}\boldsymbol{u}_{L,m}(+). \tag{2-46}$$

The elements of the transmission matrix in Eq. (2-23) can be expressed as

$$\tau_{n,m} = \widetilde{\boldsymbol{u}}^{\dagger}_{R,n}(+)\boldsymbol{G}^r_{S+1,0}\left[\boldsymbol{G}^{b,r}_{0,0}\right]^{-1}\boldsymbol{u}_{L,m}(+). \tag{2-47}$$

In the second step, we define two matrices; one is $\boldsymbol{U}_{(L,R)}(\pm)$ whose columns are the normal modes of the heat bath regions; the other $\boldsymbol{\Lambda}_{(L,R)}(\pm)$ diagonal matrix which has the Bloch factors at its diagonal elements:

$$\begin{aligned}\boldsymbol{U}_{(L,R)}(\pm) &= \left(\boldsymbol{u}_{(L,R),1}(\pm)\boldsymbol{u}_{(L,R),2}(\pm)\cdots\boldsymbol{u}_{(L,R),N}(\pm)\right),\\ \Lambda_{(L,R)}(\pm)_{m,n} &= \lambda_{(L,R),n}(\pm)\delta_{m,n}.\end{aligned} \tag{2-48}$$

These matrices satisfy the following relation:

$$\boldsymbol{F}(\pm)\boldsymbol{U}(\pm) = \boldsymbol{U}(\pm)\boldsymbol{\Lambda}(\pm). \tag{2-49}$$

Similarly, the advanced matrices, $\boldsymbol{U}^a_{(L,R)}(\pm)$ and $\boldsymbol{\Lambda}^a_{(L,R)}(\pm)$, can be defined by using the advanced mode vectors and Bloch factors. With these matrices, the transmission matrix can be deformed as

$$\boldsymbol{\tau} = \boldsymbol{U}_R^{-1}(+)\boldsymbol{G}^r\boldsymbol{Q}_0\boldsymbol{U}_L(+). \tag{2-50}$$

The third step is to express the practical form of the velocity matrix, $\boldsymbol{V}_R(+)$. The group velocity is described as $\boldsymbol{v}_g = \partial\omega/\partial q$, which can be calculated by using Eq. (2-17) as

$$\begin{aligned}\boldsymbol{V}_R(+) &= \frac{i}{\omega}\left[\boldsymbol{U}_R^{\dagger}(+)\boldsymbol{B}_R^{\dagger}\boldsymbol{U}_R(+)\boldsymbol{\Lambda}_R(+) - \boldsymbol{\Lambda}_R^{\dagger}(+)\boldsymbol{U}_R^{\dagger}(+)\boldsymbol{B}_R\boldsymbol{U}_R(+)\right]\\ &= \frac{i}{\omega}\boldsymbol{U}_R^{\dagger}(+)\left[\boldsymbol{B}_R^{\dagger}\boldsymbol{F}_R(+) - \boldsymbol{F}_R^{\dagger}(+)\boldsymbol{B}_R\right]\boldsymbol{U}_R(+) = \frac{i}{\omega}\boldsymbol{U}_R^{\dagger}(+)\left[\boldsymbol{\Sigma}^r_R - \boldsymbol{\Sigma}^{r\dagger}_R\right]\boldsymbol{U}_R(+)\\ &= \frac{i}{\omega}\boldsymbol{U}_R^{\dagger}(+)\boldsymbol{\Gamma}_R\boldsymbol{U}_R(+).\end{aligned} \tag{2-51}$$

where $\boldsymbol{\Gamma}_{(L,R)} = i[\boldsymbol{\Sigma}^r_{(L,R)} - \boldsymbol{\Sigma}^{r\dagger}_{(L,R)}]$. $\boldsymbol{\Gamma}_{(L,R)}$ is the imaginary part of the modified Green's function, so corresponds to the density of states including the perturbation. The similar expression is held about $\boldsymbol{V}_L(+)$ as

$$\boldsymbol{V}_L(+) = \frac{i}{\omega}\boldsymbol{U}_L^{\dagger}(+)\boldsymbol{\Gamma}_L\boldsymbol{U}_L(+) = \frac{i}{\omega}\boldsymbol{U}_L^{a\dagger}(-)\boldsymbol{\Gamma}_L\boldsymbol{U}_L^{a}(-). \tag{2-52}$$

In the final step, we prove $\boldsymbol{Q}_0 = i\omega\boldsymbol{\Gamma}_L$ from Eq. (2-22) multiplied by $\sum_m \tilde{\boldsymbol{u}}_{L,m}^{a}(-)\tilde{\boldsymbol{u}}_{L,m}^{a\dagger}(-)$ on left and by $\boldsymbol{I} = \sum_n \boldsymbol{u}_{L,n}(+)\tilde{\boldsymbol{u}}_{L,n}^{\dagger}(+)$ on right:

$$\begin{aligned}
\boldsymbol{Q}_0 &= \boldsymbol{B}_L[\boldsymbol{F}_L^{-1}(+) - \boldsymbol{F}_L^{-1}(-)] = \boldsymbol{B}_L\boldsymbol{F}_L^{-1}(+) - [\boldsymbol{F}_L^{a\dagger}(-)]^{-1}\boldsymbol{B}_L^{\dagger} \\
&= \sum_m \tilde{\boldsymbol{u}}_{L,m}^{a}(-)\tilde{\boldsymbol{u}}_{L,m}^{a\dagger}(-)\left[\boldsymbol{B}_L\boldsymbol{F}_L^{-1}(+) - \left[\boldsymbol{F}_L^{a\dagger}(-)\right]^{-1}\boldsymbol{B}_L^{\dagger}\right]\sum_n \boldsymbol{u}_{L,n}(+)\tilde{\boldsymbol{u}}_{L,n}^{\dagger}(+) \\
&= \sum_{n,m} \tilde{\boldsymbol{u}}_{L,m}^{a}(-)\tilde{\boldsymbol{u}}_{L,n}^{\dagger}(+)\left[\frac{1}{\lambda_n(+)}\boldsymbol{u}_{L,m}^{a\dagger}(-)\boldsymbol{B}_L\boldsymbol{u}_{L,n}(+) - \frac{1}{\lambda_m^{a*}(+)}\boldsymbol{u}_{L,m}^{a\dagger}(-)\boldsymbol{B}_L^{\dagger}\boldsymbol{u}_{L,n}(+)\right] \\
&= \sum_n \tilde{\boldsymbol{u}}_{L,n}^{a}(-)\tilde{\boldsymbol{u}}_{L,n}^{\dagger}(+)\left[\frac{1}{\lambda_n(+)}\boldsymbol{u}_{L,n}^{\dagger}(+)\boldsymbol{B}_L\boldsymbol{u}_{L,n}(+) - \lambda_n(+)\boldsymbol{u}_{L,n}^{\dagger}(+)\boldsymbol{B}_L^{\dagger}\boldsymbol{u}_{L,n}(+)\right] \\
&= i\omega\sum_n \tilde{\boldsymbol{u}}_{L,m}^{a}(-)\tilde{\boldsymbol{u}}_{L,n}^{\dagger}(+)\boldsymbol{V}_{L,n,n}(+) = i\omega\boldsymbol{\Gamma}_L.
\end{aligned} \tag{2-53}$$

where we use Eqs. (2-18) and (2-19) at the forth equal, and do Eq. (2-52) at the sixth one. The fifth equal can be proved by comparing Eq. (2-17) and its complex conjugate. Substituting Eqs. (2-50), (2-51), and (2-53) into Eq. (2-26), the following expression is obtained:

$$T = \mathrm{Tr}[\boldsymbol{\Gamma}_R\boldsymbol{G}^r\boldsymbol{\Gamma}_L\boldsymbol{G}^a], \tag{2-54}$$

which is called as the Caroli's formula, the key equation in the NEGF formalism. The actual procedures in the calculation of the thermal conductance are as following: calculating 1) the dynamical matrices of the system, 2) the surface Green's functions of heat bath regions by the recursive procedure, 3) the Green's function with the perturbation of surfaces, 4) the transmission coefficients by the Caroli's formula, and then 5) the thermal conductance with the Landauer formula divided by the temperature difference.

As mentioned above, $\boldsymbol{\Gamma}_{(L,R)}$ is related to the density of states. So we can recalculate the carrier properties in the scattering region including the perturbation of heat bathes. If the carriers were electrons, we can guess the Hamiltonian from the density of states and repeat of the above

procedures, resulting in the converged non-equilibrium Hamiltonian and Green's functions [11]. For phonons, it has not found how to make the dynamical matrices from the vibrational density of states, and such repeating procedures are less able. However, the errors can be neglected when the temperature differences are small. The NEGF is usually applied to the linear response phenomena, where the small temperature difference is definitely appropriate.

2-3 Non-equilibrium Molecular dynamics

The NEMD methods adopt a similar system to the one of NEGF, namely, the thermal conductor with some temperature difference. NEMD is assumed to use the classical molecular dynamics with low computational cost. The empirical potentials enable us to calculate dynamics of large systems at once, so the NEMD methods do not need the slice model and recursive procedures employed in the NEGF method. Instead there are several ways to set up the system reproducing the thermal conduction phenomena, shown in Fig. 2-4.

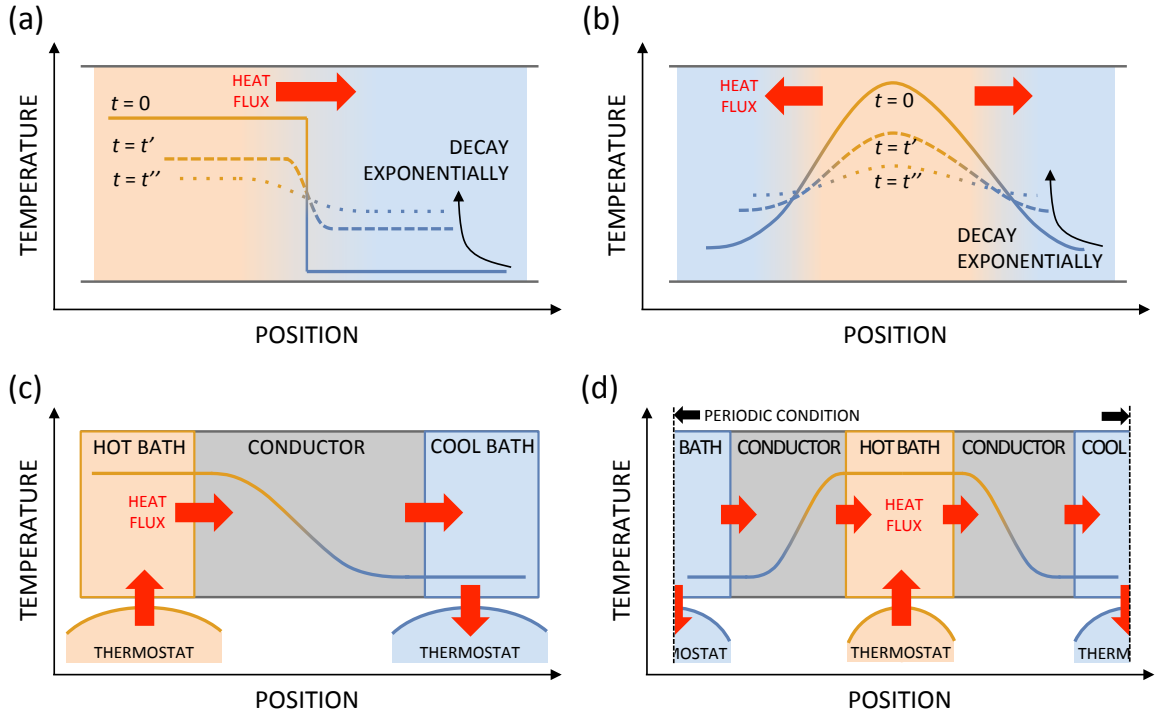

Fig. 2-4. The schematics of (a) the non-steady non-equilibrium system [12], (b) the pumping non-equilibrium system [13], (c) the isolated steady non-equilibrium system, and (d) the periodic steady non-equilibrium system [14].

In terms of stationarity, the practical systems used in NEMD are classified into two groups: the non-steady non-equilibrium system and steady non-equilibrium system. Fig. 2-4 (a) indicates the newest one of the former group, which is proposed in 2014 [12]. The calculation

begins with the system, which is separated into two regions with different temperatures. The time evolution of the system is observed regarding the relaxation of the temperature difference, by substituting which in the diffusion equation the thermal conductivity is evaluated. We can perform the same evaluation by adding an initial energy at some position like Fig 2-4 (b), which is the conventional method [13]. It means that the non-steady methods can be seen as an analogy of the pump-probe method in experiment. It calculates the conductivity assuming the exponential relaxation processes, and does not need to wait full relaxation to thermal equilibrium. Thus, the non-steady methods usually require less computational time than the steady one. In the steady method, we assume the almost same system as the NEGF model, where the thermal conductor is sandwiched by two heat baths with different temperatures shown in Fig. 2-4 (c) and (d) [14]. During the evolution, the temperature gradient and heat flux in the thermal conductor relax into a steady state. The Fourier's law is used to calculate the thermal conductivity with the steady temperature difference and thermal flow. While the steady methods take rather long computational time for relaxation, they have definite conduction regions and are easy to be applied to general heterogeneous systems.

There are also two types of boundary conditions in NEMD, viz., truncated systems and periodic systems. The difference between them is more serious for the steady method. Fig. 2-4 (c) is an example of the steady system without periodic boundary condition, both sides of which is considered as the hot and cool baths. Such truncated systems totally reduce computational costs because long-range interactions are confined within small regions. As the same time, we should carefully consider the termination of both ends so as not to affect the thermal properties and not to violate charge neutralization of the systems. These systems are often not appropriate to ionic systems, where the long-range interactions are significant. Periodic steady systems do not suffer

from such artificial termination conditions. However, separated heat bathes require additional conductor regions, shown as Fig. 2-4 (d). The double-sized system costs corresponding computational time even for non-ionic systems, and much more for ionic ones.

In the following research, we employ the NEMD method with the periodic steady systems, whose practical procedures are explained below. The basic method using two thermostats is introduced, in addition to analytical methods to compare with the experimental conductivity. After that, we explain the modified method that is actually used, called as the reverse non-equilibrium molecular dynamics (RNEMD).

NON-EQUILIBRIUM MOLECULAR DYNAMICS The basic NEMD with steady systems consists of the following four steps:

1) Equilibrate the whole system including the heat bath regions by some thermostat with the target temperature T_{target}, where the thermal conductivity will be observed.
2) Remove the T_{target} thermostat and add two partial thermostats: one with T_{low} for the cool bath region, and the other with T_{high} for the hot bath.
3) Evolve the system with measuring the thermal flow and temperature gradient between two baths.
4) After the relaxation of the system, the thermal conductivity is calculated from the Fourier's law, namely, $\kappa = J/(T_{\mathrm{high}} - T_{\mathrm{low}})$.

The temperatures of two heat baths are usually defined around the target temperature as $T_{\mathrm{target}} = (T_{\mathrm{high}} + T_{\mathrm{low}})/2$. The thermal flux is given by

$$\boldsymbol{J} = \frac{1}{V}\left(\sum_i E_i \boldsymbol{v_i} - \sum_i \left(\overline{\boldsymbol{r}_i \otimes \boldsymbol{f}_i}\right)\boldsymbol{v}_i\right), \tag{2-55}$$

where E_i is the energy attributed to ith atom in the system, $\boldsymbol{v}_i$ is the velocity, $\boldsymbol{r}$ is the position, and $\boldsymbol{f}_i$ the atomic force. $\overline{\boldsymbol{r}_\iota \otimes \boldsymbol{f}_\iota}$ is the sum of $\boldsymbol{r}_n \otimes \boldsymbol{f}_n$ for all interactions related to ith atom. The first terms corresponds to the energy transfer via the motion of atoms. Such convection has little effect for solid structures. The second term means the transfer via the forces from the displacement of atoms, namely, vibrations, which is the dominant factor of the thermal conduction in crystal. Put another way, this contribution corresponds to the transfer of the pressure, because it is found that $\boldsymbol{r} \cdot \boldsymbol{f}/V$ is an atomic expression of the pressure as the following. We assume the simplest example, which is the isotropic cubic system with a length L. The system is equilibrated into the canonical ensemble, where the physical properties are described with the distribution function. The pressure is calculated as

$$P = k_b T \left(\frac{\partial \ln Q}{\partial V} \right)_T, \tag{2-56}$$

where k_b is the Boltzmann constant, V the volume, and T the temperature. $Q(V, N; T)$ is the distribution functions and given by

$$Q(V, N; T) = \frac{1}{h^{3N} N!} \iint d\boldsymbol{r} d\boldsymbol{p} \exp[-H(\boldsymbol{r}, \boldsymbol{p})/k_b T], \tag{2-57}$$

where h is the Plank constant, H the classical Hamiltonian, and $\{\boldsymbol{r}, \boldsymbol{p}\}$ the set of position and momentum of atoms. Using the Gaussian integral, the integration of the Hamiltonian about momenta can be calculated as

$$Q(V, N; T) = \frac{2\pi m k_b T^{3N/2}}{h^{3N} N!} \int d\boldsymbol{r} \exp[-V_{int}(\boldsymbol{r})/k_b T] = \frac{1}{\Omega^{3N} N!} Z(V, N; T), \tag{2-58}$$

where $V_{int}(\boldsymbol{r})$ is the potential of the system and $Z(V, N; T)$ is the volume dependent part of the distribution function. Ω is the constant, which comes from the Gaussian integral of each degree of freedom. With Eqs. (2-56) and (2-58), the pressure is described as the following:

$$P = \frac{k_b T}{Z(V,N;T)}\frac{\partial Z(V,N;T)}{\partial V} = \frac{Nk_bT}{V} - \int_0^1 d\boldsymbol{q}\frac{\partial V_{int}\left(V^{1/3}\boldsymbol{q}\right)}{\partial V}\exp\left[-V_{int}\left(V^{1/3}\boldsymbol{q}\right)/k_b\,T\right]$$
$$= \frac{Nk_bT}{V} - \left\langle\frac{\partial V_{int}}{\partial V}\right\rangle = \frac{Nk_bT}{V} - \frac{1}{3V}\left\langle\sum_i \boldsymbol{r_i}\frac{\partial V_{int}}{\partial \boldsymbol{r_i}}\right\rangle = \frac{Nk_bT}{V} - \frac{1}{3V}\left\langle\sum_i \boldsymbol{r_i}\cdot\boldsymbol{f}_i\right\rangle, \quad (2\text{-}59)$$

where $\boldsymbol{q}$ is the position vectors of atoms normalized by L. As similar to Eq. (2-55), the first term in Eq. (2-59) is the contribution of moving atoms, which hit the walls of systems. The second term corresponds to the force of the interactions, which results in the vibrations in solid systems and the second terms in Eq. (2-55). In the anisotropic system, the response to forces is not diagonal and we should consider the strain tensor. Then the pressure is also extended into the pressure tensor like $\boldsymbol{r}\otimes\boldsymbol{f}$.

As we have seen, both of the procedures and background of the NEMD method is much simpler and more straightforward than those of NEGF. However the results often strongly depend on the details of the computational systems and we should set up them carefully in order to compare the other results. The first important point is the temperature difference. NEMD assumes the linear thermal conduction and the temperature difference should be small enough not to deviate from the linear regime. Large differences result in temperature jumps between the heat bath and thermal conductor, which should be suppressed. The second point is the length of the thermal conductor. In this method, the thermal conductivity is calculated by the Fourier's low, namely, the diffusion equation. The diffusive energy transfer occurs in the system longer than the mean free paths of phonons that have the main contribution to the thermal conduction. The smaller systems are used, the more ballistic phonons contribute to the thermal conduction. The Ballistic conduction does not associate with the temperature gradient and cannot be taken into account by the Fourier's low, resulting in overestimation of the conductivity. The error is tends to be large for materials with high thermal conductivity, because they often have phonons with long mean free paths. Third, we should

also take care of the length of the heat bath regions. The wavelengths of induced phonons from the heat baths are limited by the length of the bathes their selves. The system with short heat baths cannot describe the thermal conduction via phonons with long wavelength. In other words, the phonon distributions of vibration baths depend on the their length, sometimes resulting in the artificial interface resistance between the thermal conductor and heat baths. This error can be observed as the temperature jumps at the interface, so we should use the long baths enough to attenuate the jumps. In many cases, the half length of the thermal conductor is used for the heat baths at least [15]. Lastly, we have to consider that the thermal conductivity depends on the length of the conductor and NEMD results should be modified to compare with other theoretical or experimental data. Since the computational systems are usually much shorter than the experimental samples, we calculate the several conductivities of systems with different length, from which a comparable conductivity is extrapolated to the one of the infinite system, κ_∞ [16]. For the extrapolation, we begin with the detailed expression of Eq. (1.4).

$$\kappa_l = \sum_{\boldsymbol{k}} \sum_{n} C_l(n, \boldsymbol{k})\, v_g(n, \boldsymbol{k})\, \tau(n, \boldsymbol{k}; L), \tag{2-60}$$

where $C_l(n, \boldsymbol{k})$ is the lattice specific heat of each phonon mode of nth branch and a wave vector $\boldsymbol{k}$, $v_g(n, \boldsymbol{k})$ the group velocity, and $\tau(n, \boldsymbol{k}; L)$ the relaxation time. In order to discuss the length dependency, we separate the relaxation time into two contributions: the scattering in the thermal conductor and one at the interface between heat baths. These scattering phenomena are assumed to be isolated, and the relaxation time is given by

$$\frac{1}{\tau(n, \boldsymbol{k}; L)} = \frac{1}{\tau_p(n, \boldsymbol{k})} + \frac{1}{\tau_b(n, \boldsymbol{k}; L)}, \tag{2-61}$$

where $\tau_p(n, \boldsymbol{k})$ is the contribution of the phonon-phonon scattering and $\tau_b(n, \boldsymbol{k}; L)$ is the one of the interfacial scattering. The later effects are averaged about all phonon modes, corresponding to

the time required for phonons to move to the interface from the averaged position, viz., the center of the conductor. Then $\tau_b(n, \boldsymbol{k}; L)$ is expressed as the following:

$$\tau_p(n, \boldsymbol{k}) = \frac{L/2}{\left|v_g(n, \boldsymbol{k})\right|}. \tag{2-62}$$

With Eqs. (2-61) and (2-62), the lattice thermal conductivity is calculated as

$$\kappa(L) = \sum_n \sum_{\boldsymbol{k}} C_l(n, \boldsymbol{k}) \left[v_g(n, \boldsymbol{k})\right]^2 \tau_p(n, \boldsymbol{k}) \left[1 + \frac{2\left|v_g(n, \boldsymbol{k})\right| \tau_p(n, \boldsymbol{k})}{L}\right]^{-1}. \tag{2-63}$$

The above equation shows that $1/\kappa$ is a function of $1/L$, $f(1/L)$, which converges to $1/\kappa_\infty$ for $L \to \infty$. Here we introduce an assumption, where $1/\kappa$ can be Taylor expanded with respect to $1/L$ at around $f(0)$, which is plausible for diffusive phenomena. The thermal conductance of the infinite system is evaluated as

$$\frac{1}{\kappa_\infty} = f(0) = f\left(\frac{1}{L}\right) + \frac{f'^{(1/L)}}{1!}\left(-\frac{1}{L}\right) + \frac{f''^{(1/L)}}{2!}\left(-\frac{1}{L}\right)^2 + \cdots, \qquad with\ L \to \infty. \tag{2-64}$$

In practical, only the first order term is often used for extrapolation, because results in NEMD include not small fluctuations and the accurate prediction of the second and higher order terms is difficult. An error of the linear approximation comes from the difference of phonon mean free paths. So the error is negligible for materials with low thermal conductivity, where almost of all phonons have short mean free paths.

REVERSE NON-EQUILIBRIUM MOLECULAR DYNAMICSR In the above NEMD method, the input is the temperature difference, as whose responses the thermal flux and temperature gradient are equilibrated. This method is simple but has several disadvantages. One is that the thermostats of the heat bath regions spoil the conservation of the microscopic motions. Another is the artificial boundary between the thermal conductor and heat baths. The other is the very slow relaxation of the flux and gradient. RNEMD is proposed to solve these problems, where “reverse”

indicates the inversion relation of the input and response. In this method, we input the artificial thermal flux, and the temperature gradient is observed as the response [17]. As shown in Fig. 2-5, the practical procedures are the followings:

1) Equilibrate the whole system by some thermostat with the target temperature T_{target}, where the thermal conductivity will be observed.
2) Define the hot bath and cool bath regions.
3) Evolve the system.
4) At uniform time intervals, exchange the velocity of the fastest atom in the cool bath for the one of the slowest atom in the hot bath.
5) After the relaxation of the system, the conductivity is calculated with $\kappa = J/(T_{\text{high}} - T_{\text{low}})$.
6) Modify the results by extrapolating.

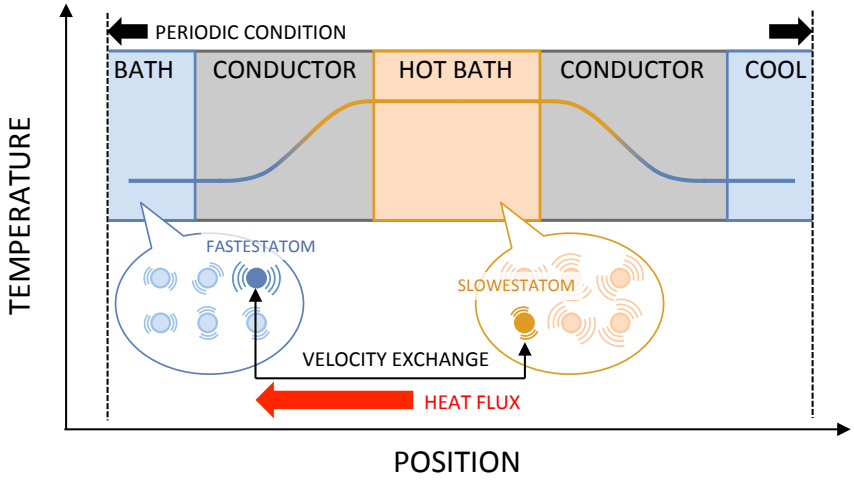

Fig. 2-5. The schematic of the RNEMD, where the artificial heat flux is induced by the velocity swapping.

The main difference between the general NEMD is the exchanging procedures from 2) to 4). The velocity exchanging extracts the energy from the cool bath to hot bath. It results in the artificial thermal flux without the thermostats, which does not spoil the energy conservation. While

the simple velocity exchange is enough for the monoatomic system, the multiatomic one requires swapping the velocities scaled with square roots of atomic masses for the energy conservation. The exchange of scaled velocities violates the momentum conservation, but the energy one should be preferred. The thermostat free calculations also remove the artificial boundaries and keep the continuity of the systems. It results in the quick conversion of temperature gradient than NEMD. Moreover, artificial thermal flux is well-defined and enables us to skip to calculate non-equilibrium atomic pressures, whose ensemble is quite unclear.

While the RNEMD method solves or attenuates the problems in NEMD, this method also has practical issues in the application to materials with low thermal conductivities. In these materials, the temperature gradient responses sensitively and linear thermal transport is easily collapsed. To avoid it, the swapping time intervals should be long as much as the response is linear. It usually takes enormous amount of computational time, so we should attempt to find out how to compromise this problem.

Bibliography

[1] Hamaguchi, C. (2001). *Basic Semiconductor Physics.* Springer. ISBN 3540416390.

[2] Frenkel, D.; Smit, B. (2002). *Understanding Molecular Simulation: From Algorithms to Applications.* Academic Press. ISBN 0122673514.

[3] Kojevnikov, A. B. (1993). Paul Dirac and Igor Tamm correspondence; 1, 1928-1933. *CERN Articles & Preprints.*

[4] Landauer, R. (1992) Conductance from transmission: common sense points. *Physica Scripta.* T42: 110-114.

[5] Büttiker, M. (1988). Symmetry of electrical conduction. *IBM J. Res. Dev.* 32:317-334.

[6] Keldysh, L. V. (1965). Diagram Technique for Nonequilibrium Processes. *J. Exp. Theor. Phys.* 20: 1018-1026.

[7] Khomyakov, P. A. and Brocks, G. (2004). Real-space finite-difference method for conductance calculations. *Phys. Rev. B* 70: 195402.

[8] Khomyakov, P. A.; Brocks, G.; Zwierzycki, M. and Kelly, P. J. (2005). Conductance calculations for quantum wires and interfaces: Modes matching and Green's functions. *Phys. Rev. B* 72: 035450.

[9] Datta, S. *Electronic Transport in Mesoscopic Systems.* Cambridge University Press. ISBN 0521599431.

[10] Fetter, A. L. and Walecka, J. D. *Quantum Theory of Many-Particle Systems.* Dover Publications. ISBN 0486428273.

[11] Brandbyge, M.; Mozos, J.-L.; Ordejón, P.; Taylor, J. and Stokbro, K. (2002). *Density-functional method for nonequilibrium electron transport. Phys. Rev. B* 65: 165401.

[12] Melis, C.; Dettori, R.; Vandermeulen S. and Colomboa, L. (2014). Calculating thermal

conductivity in a transient conduction regime: theory and implementation. *Eur. Phys. J. B* 87: 96.

[13] Tsai, D. H. and MacDonald, R. A. (1976). Molecular-dynamical study of second sound in a solid excited by a strong heat pulse. *Phys. Rev. B* 14: 4714-4723.

[14] Baranyai, A. (1996). Heat flow studies for large temperature gradients by molecular dynamics simulation. *Phys. Rev. E* 54: 6911-6917.

[15] Shiomi, J. (2014). NONEQUILIRIUM MOLECULAR DYNAMICS METHODS FOR LATTICE HEAT CONDUCTION CALCULATIONS. *Annu. Rev. Heat Transfer* 17: 177-203.

[16] Sellan, D. P.; Landry, E. S.; Turney, J. E.; McGaughey, A. J. H. and Amon C. H. (2010). Size effects in molecular dynamics thermal conductivity predictions. *Phys. Rev. B* 81: 214305.

[17] Muller-Plathe, (1997). A simple nonequilibrium molecular dynamics method for calculating the thermal conductivity. *J. Chem. Phys.* 106: 6082-6085.

CHAPTER 3

CHIRALITY DEPENDENCE OF THERMAL TRANSPORT PROPERTIES IN SINGLE-WALLED CARBON NANOTUBES

Low-dimensional nanostructures have attracted attention as cutting-edge materials showing many characteristic properties [1, 2]. In particular, one-dimensional (1D) tubular nanostructures are promising candidates as materials for nano-electronic devices because such tubular structures have distinctive physical properties that differ from those of bulk structures, such as their quantum properties, large surface area, and high directivity. Carbon nanotubes (CNTs) are one of such nanostructures with the most potential because of their high electronic conductivity, stability, and flexibility. Because of their physical properties, CNTs are expected to be suitable materials for nanowires [3], nanotransistors [4], and photosensors [5].

In addition to these characteristics, CNTs are also addressed as suitable materials for heat management in nanoelectronic devices, owing to their significant thermal transport properties [6]. Specifically, one experiment prepared a thin film of aligned single-walled carbon nanotubes (SWCNTs), showing a high thermal conductivity around $200\ \mathrm{W/(mK)}$ at $300\ \mathrm{K}$ [7]. The other showed that a suspended multi-walled carbon nanotube with a length around of $2.5\ \mu\mathrm{m}$ has a thermal conductivity that increases monotonically until a high temperature, $\sim 300\ \mathrm{K}$ [8]. Moreover, recent measurements of individual nanotubes showed their prominent conductivity around $3000\ \mathrm{W/(mK)}$ [9, 10]. These properties are attributed to that effects of anharmonicity and the Umklapp scattering are relatively small even at room temperature because of the long mean free paths of their phonons. For efficient exhausting heat in devices, we should utilize such ballistic characteristics of CNTs, which can be achieved by microscopic understanding of their thermal

transport properties. The large difference between the mat and individual samples also promise that CNTs shows some controllable structural factors.

Phonons pass through thermal conductors without scattering in ballistic systems, where the sizes of conductors are smaller than the mean free paths of phonons contributing to thermal transport. On the analogy of electric currents, it is expected that the ballistic thermal conductance is quantized at low temperature because the conductance is proportional to the number of discrete phonon states. The thermal conductance normalized by a contribution of each phonon should show a step function, terraces of which are called as quantized plateaus [11, 12]. By using bulk SWCNT samples, Hone *et al*. observed the quantized plateaus in the thermal conductance divided by the temperature, whose plateaus were maintained up to $T = 40$ K [13]. Individual SWCNTs do not include any inter-layer interactions and their phonons are estimated to have the particularly long mean free paths, resulting in the longer quantized plateaus than those of other CNTs.

A theoretical analysis supports these results based on the Landauer formula and an adiabatic contact approximation. This contact assumes that transmission coefficients are equal to 1 in the energy range where phonon bands exist, and the absolute value of plateaus is explained only by the number of excited normal modes. Thus, the normalized thermal conductance remains flat during the lowest optical modes $\hbar\omega_{op}^{0}$ are excited. To estimate the length of plateaus, $\hbar\omega_{op}^{0}$ is calculated by using the zone-folding method [14]. In this method, the dynamical matrices of SWCNTs are made from those of graphenes with a rolled-up boundary condition, showing that $\hbar\omega_{op}^{0}$ increases as the tube radius decreases. With these results, the approximated Laudauer formula shows that the maximum width of quantized plateaus in SWCNTs is 20 K, which is the half of the experimental value, 40 K. This discrepancy indicates that the SWCNTs' thermal conductance and $\hbar\omega_{op}^{0}$ are affected by other structural factors than the radius, which cannot be considered under the adiabatic

contact and zone-folding approximation. For graphene, its thermal transport property is strongly affected by the conducting direction: the zigzag or armchair direction [15]. Thus, it is expected that we can tailor the ballistic transport properties of SWCNTs by the roll-up directions of tubes, namely, their chiralities.

In this study, we calculate the thermal conductance of SWCNTs with three different chiralities. To reveal the chirality dependence, we should perform higher precision calculations than the approximated Landauer formula including the adiabatic contact and zone-folding approximation. Then, the NEGF method shown in Sec. 2-2 is employed, where the transmission coefficients are described by using the Green's functions. The Green's functions are calculated from the dynamical matrices, which are evaluated by the frozen phonon method with the first-principles calculations [16]. The first-principles calculations are performed based on the density functional theory, which enable us to discuss the charily dependence of thermal transport properties with the precise vibrational properties of SWCNTs. We evaluate thermal conductance in a wide temperature range: $10 < T < 1000$ K. For the detailed investigation of the quantized plateau, the calculations focused on the low temperature region $(10 < T < 100\ \mathrm{K})$ are also performed.

This chapter is organized as follows. In Sec. 3-1, we shall introduce the computational details including the SWCNTs models with the semi-infinite heat baths. Sec. 3-2 shows the microscopic physical properties, namely, the phonon properties, transmission coefficients, and perturbations of the heat baths, which are fundamentally related to the thermal conductance. In Sec. 3-3, the thermal conductances of SWCNTs are evaluated, especially focusing on their quantized plateaus at the low temperature region. A summary of this chapter is given in Sec. 3-4.

3-1 Computational details

MODEL SETUP The three SWCNT structures are adopted with the different chiralities, shown in Fig. 3-1 (a). Chirality of SWCNTs is sometimes classified by their edge structures as the armchair, zigzag or chiral type; but the most convenient way is using a chirality vector, which is a rolled up direction from grapheme ribbons to SWCNTs [17]. The chirality vector is described with the combination of two numbers, which correspond to coefficients of the Bravais lattice vectors for graphenes, as we can see in Fig. 3-1 (b). With this notation, our models are describes as the SWCNTs $(3,3)$, $(5,0)$ and $(4,2)$, classified as the armchair, zigzag and chiral type, respectively.

Table. 3-1. Structural information of SWCNTs $(3,3)$, $(5,0)$, $(4,2)$, and $(7,0)$: d, l_z, and N are the diameter, tube length, and number of atoms in unit cells, which is used for dynamical matrix calculations. $\hbar\omega_{\mathrm{op}}^{0}$ are the lowest optical energies obtained by using primitive cells. $\hbar\gamma_{\mathrm{op}}[\omega_{\mathrm{op}}^{0}]$ are projected normal modes' couplings at $\hbar\omega_{\mathrm{op}}^{0}$. The SWCNT $(7,0)$ have very low $\hbar\omega_{\mathrm{op}}^{0}$, whose numerical errors prevent $\hbar\gamma_{\mathrm{op}}[\omega_{\mathrm{op}}^{0}]$ being extracted.

	d	l_z	N	$\hbar\omega_{\mathrm{op}}^{0}$	$\hbar\gamma_{\mathrm{op}}[\omega_{\mathrm{op}}^{0}]$
	(Bohr)	(Bohr)	-	(meV)	(meV)
SWCNT $(3,3)$	7.97	70.21	180	19.96	2.36
SWCNT $(5,0)$	7.75	72.38	180	16.74	4.70
SWCNT $(4,2)$	8.04	64.33	168	15.75	6.24
SWCNT $(7,0)$	10.73	73.06	252	11.90	-

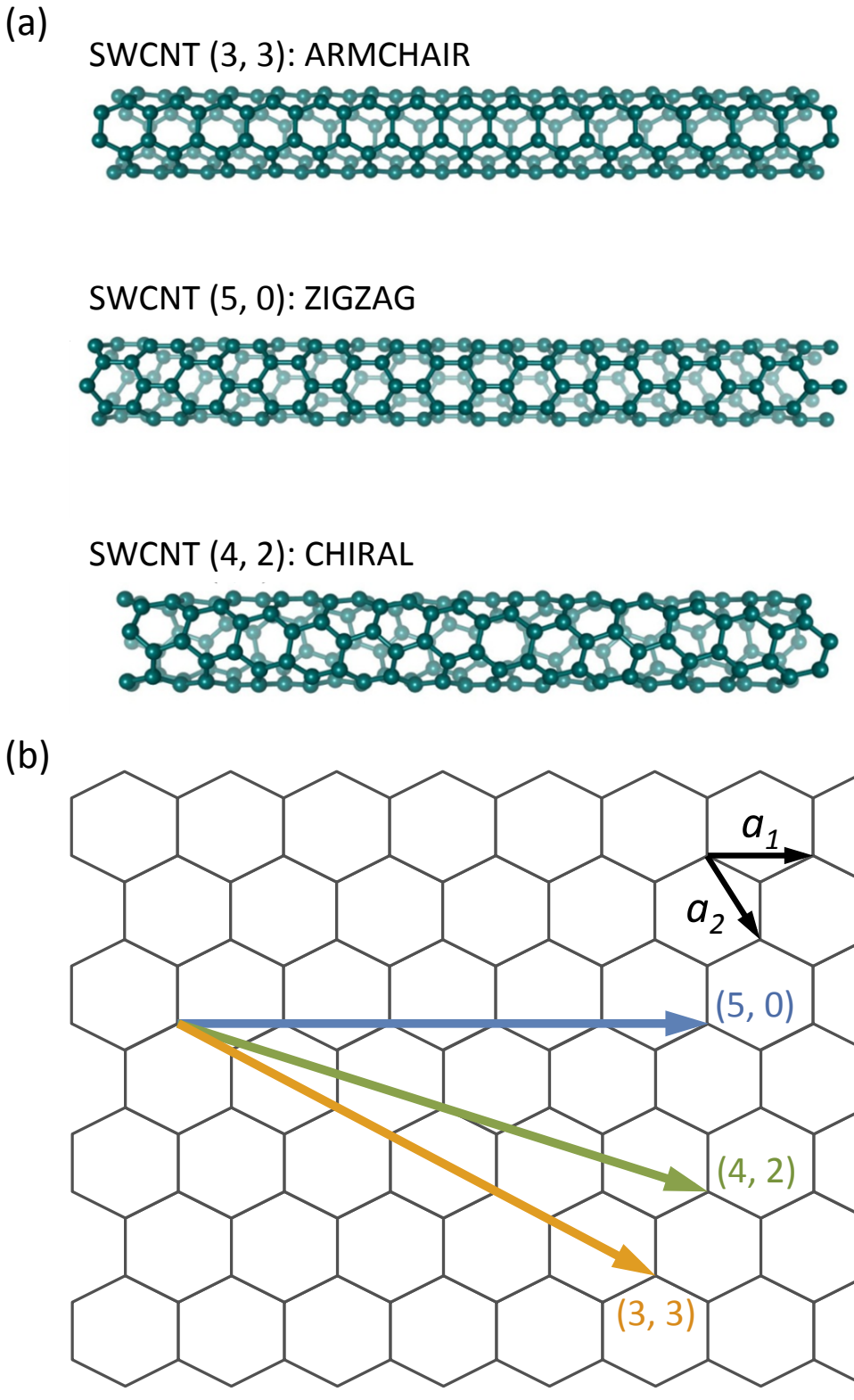

Fig. 3-1. (a) Atomic structures of SWCNTs with three different chiralities. (b) Definition of chiral vectors and corresponding vectors to the models.

Each model has the shortest radius and so the highest $\hbar\omega_{op}^{0}$ in the corresponding chirality type. Their radii, unit lengths, and numbers of atoms are almost identical (Table. 3-1), thus, we assume that the difference in the thermal properties can be attributed to their chiralities. This assumption is confirmed by an additional calculation about the SWCNT $(7,0)$ with a larger radius in the following chapter. The unit cell has 15 Å vacuum along the radial non-conducting direction $(x\text{-}y)$, and the periodic boundary condition is imposed to the tube direction (z) in the dynamical matrix calculations. In the NEGF calculations, these models are divided into three parts (the left heat bath region, scattering center region, and right heat bath region) with an equivalent number of atoms: each region contains 60 atoms in the SWCNTs $(3,3)$ and $(5,0)$; 56 atoms in $(4,2)$.

The structural optimization and dynamical matrix calculations are performed using SIESTA [18]. We employ the local density approximation (LDA) for the exchange and correlation functional in density functional theory calculations [19]. Core electrons are described by the Troullier-Martins pseudopotential [20] with the Kleinman-Bylander projector [21] and the Kohn-Sham orbitals are expanded by the double-zeta plus polarization basis set. In the calculations of dynamical matrices, the atoms belonging to the center region are displaced 0.04 Bohr from their most stable positions. To obtain convergence of the vibrational density of states (vDOS), the Brillouin zone is sampled by $1 \times 1 \times 20$ Monkhorst-Pack grids [22]. In the NEGF calculations, an infinitesimal parameter η in Eq. (2-27) is set to 1×10^{-5} meV.

PROJECTED NORMAL MODES To evaluate the transmission coefficients and the thermal conductance in terms of the perturbation for each phonon mode, we propose the projected normal mode (PNM) analysis. The interactions with the semi-infinite heat baths modify the dynamical matrices of the scattering region, and this method projects it onto the normal mode basis of the

isolated center region. This analysis allows us to evaluate the effect of the coupling and the energy shift from the phonon-phonon interactions with the semi-infinite heat baths as

$$\begin{aligned} \gamma_q[\omega] &= -\sqrt{\left|\Im\left[\omega_q^{0\,2} - \langle\phi_q|G^{r-1}[\omega]|\phi_q\rangle\right]\right|}\ , \\ \Delta_q[\omega] &= \pm\sqrt{\left|\Re\left[\omega_q^{0\,2} - \langle\phi_q|G^{r-1}[\omega]|\phi_q\rangle\right]\right|}\ , \end{aligned} \tag{3-1}$$

where ω_q^0 is the bare frequency of the qth normal mode at the scattering region. $\gamma_q[\omega]$ is the square root of the imaginary part of Σ^r $(\equiv \Gamma)$ projected onto the qth normal mode. $\Delta_q[\omega]$ is the square root of the real part and equivalent to the energy shift projected onto the qth mode. The signs of $\Delta_q[\omega]$ with negative $\Re\left[\omega_q^{0\,2} - \langle\phi_q\left|G^{r-1}[\omega]\right|\phi_q\rangle\right]$ are set to be negative. Hereafter, we call them the projected normal modes' coupling (PNMs' coupling) and the projected normal modes' energy shift (PNMs' energy shift), respectively. Note that $\gamma_q[\omega]$ and $\Delta_q[\omega]$ explicitly depend on the induced energies, ω. A similar projection analysis is performed in electronic transport, where the couplings and energy shifts are projected onto molecular orbitals [23-25]. The values are often evaluated at their characteristic energies such as the Fermi level of the electrode with the wide-band-limit approximation. In contrast, the energy dependence of the coupling parameters is not clear for phonon transport. Therefore, in the PNM analysis, the energy-dependent profiles of $\gamma_q[\omega]$ and $\Delta_q[\omega]$ are also discussed.

3-2 Microscopic properties

STRUCTURE OPTIMIZATION AND OPTICAL MODES The structural parameters of the optimized SWCNTs and the energies of the first optical modes $\hbar\omega_{op}^{0}$, are shown in Table 3-1. $\hbar\omega_{op}^{0}$ has an important role at very low temperature because it breaks the quantized plateau of the normalized thermal conductance. The previous study using the zone-folding method showed that $\hbar\omega_{op}^{0}$ depends only on its diameter, namely, the higher $\hbar\omega_{op}^{0}$ results in the smaller diameter. For the SWCNT with a diameter of 8.0 Bohr, the extrapolation of the previous study expects $\hbar\omega_{op}^{0}$ to be 20 meV, and such extrapolated values are described as $\hbar\omega_{op}^{ext}$. $\hbar\omega_{op}^{ext}$ is comparable to our result of the SWCNT $(3,3)$, but it is considerably larger than those of $(5,0)$ and $(4,2)$. This fact clearly shows that $\hbar\omega_{op}^{0}$ is also affected by the chirality, not just by the diameters. On the other hand, $\hbar\omega_{op}^{0}$ difference between the SWCNTs $(7,0)$ and $(5,0)$ follows the radius dependence discussed in the previous study.

TRANSMISSION COEFFICIENTS The transmission coefficients of the SWCNTs $(3,3)$, $(5,0)$ and $(4,2)$ are shown in Fig.3-2 (a). Their transmission coefficients have stepwise shapes, and such quantized features correspond to the pure ballistic properties of the SWCNT systems in the NEGF calculations [26-28]. Because a SWCNT has one rotational symmetry and three translational symmetries, it has four acoustic branches, which have zero frequencies at the center of the Brillouin zone. Fig. 3-2 (a) shows that the transmission coefficients of all SWCNTs are 4 close to $0\ \mathrm{cm}^{-1}$, corresponding to those acoustic modes. In all models, there are characteristic dips in the transmission coefficients in the region 100-150 meV. 210 meV is the upper end of the phonon band, above which the transmission coefficients are vanished.

Apart from the common features as mentioned, there are also several differences. The transmission coefficients of the SWCNTs $(5,0)$ and $(4,2)$ increase from 4 to 6 immediately at ~ 5 meV, while that of the SWCNT $(3,3)$ remains 4 up to higher energy ~ 20 meV. These different transmission coefficients in the low-energy regions are partially attributed to the vibrational energy of the first optical modes, $\hbar\omega_{op}^{0}$. Such difference affects the behavior of the thermal conductance especially at low temperature, where the transmission coefficients in the low energy region dominantly contribute to the thermal conductances according to the Bose-Einstein distribution (see Eq. (2-14)). Around 50-70 meV, the transmission coefficient of the SWCNT (3, 3) has the high peaks. Conversely, the transmission coefficient of the SWCNT $(5,0)$ at 50-70 meV is less than 4, while those of the other two models are over 6. Around the temperature where the modes around 50-70 meV are excited effectively, the thermal conductance of the SWCNT $(3,3)$ will increase and the inverse is true for the SWCNT $(5,0)$.

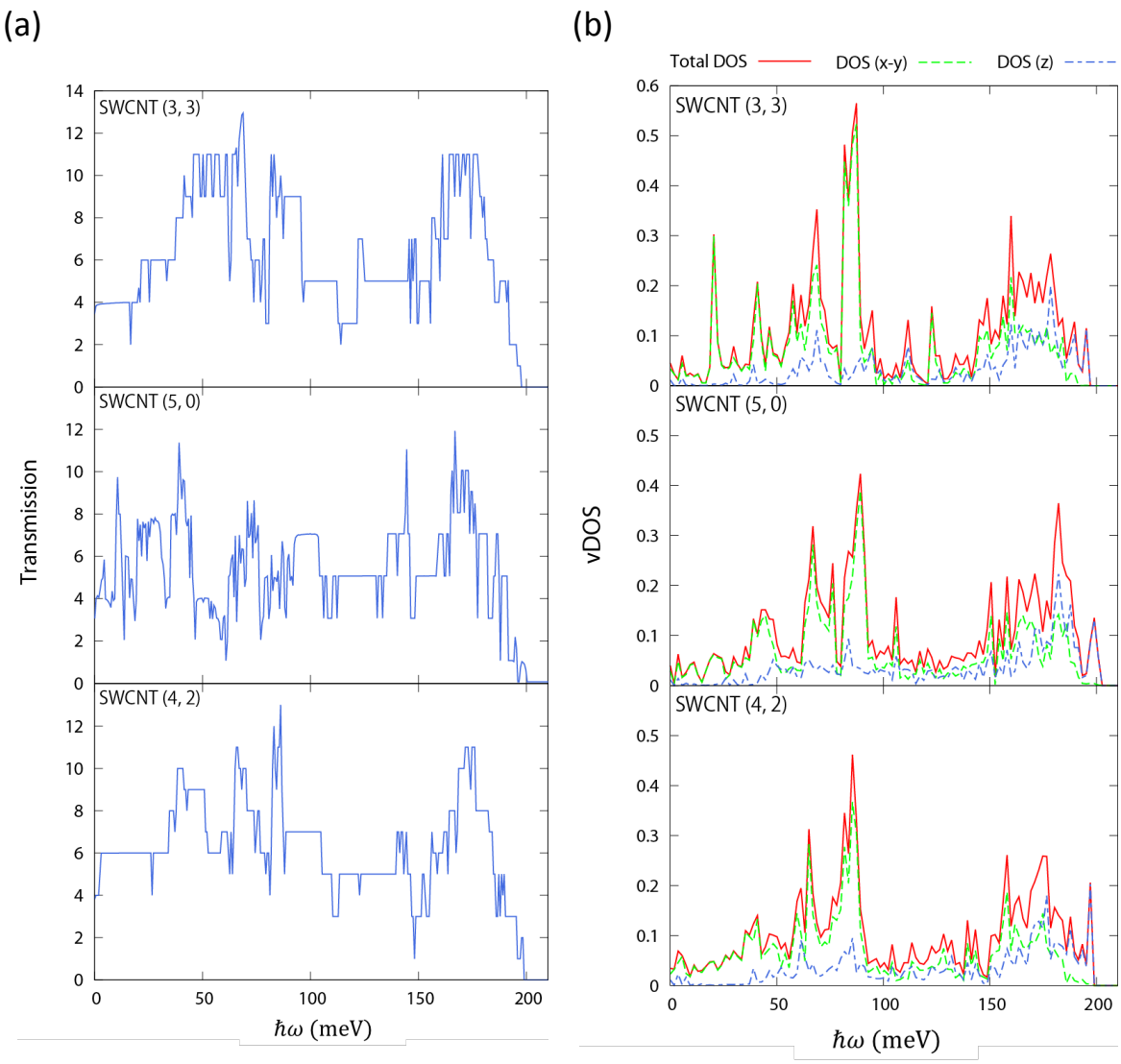

Fig. 3-2. (a) Transmission coefficients of SWCNTs $(3,3)$, $(5,0)$, and $(4,2)$. (b) Vibrational density of states of the infinite SWCNTs. The contribution is separated into the radial $(x\text{-}y)$ and tube (z) directions.

VDOS AND PNM ANALYSIS We investigate the microscopic origins of the differences in transmission coefficients with respect to the vDOS and phonon-phonon interactions with the semi-infinite heat baths. The vDOS of the SWCNTs are shown in Fig. 3-2 (b). Moreover, we decompose the total vDOS into those of the radial $(x\text{-}y)$ and tube (z) directions to examine the relationship between the direction of the phonon modes and the coupling properties. In any chirality,

the x-y components make the major contributions in the low-energy region, while the z component stands out in the high-energy region (150-200 meV). It means that the major vibrational modes change from the transverse modes to longitudinal ones with energy increase. The low peak intensities around 0 meV stem from the large dispersion of the acoustic modes. The prominent peaks in 50-100 and 140-210 meV correspond to the transverse and longitudinal optical modes respectively, and between these two regions (around 100-140 meV) the peak intensity is low.

The PNMs' couplings with the semi-infinite heat baths are calculated by using Eq. (3-1), shown in Fig. 3-3 (a). Symbols in Fig. 3-3 correspond to the ones in Eq. (3-1), namely, ω^0 is the bare frequency of the phonon modes, ω the induced energy, $\hbar\gamma_q[\omega]$ the coupling. While $\hbar\gamma_q[\omega]$ depends on the induced energy, here we take the PNMs' coupling at the energy ω^0 as a qualitative measure. For the first optical modes, $\hbar\gamma_{op}[\omega_{op}^0]$ is also given in Table. 3-1. The coupling of the SWCNT $(4,2)$ is large compared with the other models over all energies and modes, resulting in the high transmission coefficient in the whole energy region as shown in Fig. 3-2. The largest energy couplings are found around 100-140 meV in all three models. However, as we have mentioned, the phonon densities are not large in this energy range, resulting in the transmission coefficients with moderate values compared with the couplings.

With the above vDOS and PNMs' couplings, we can discuss the origin of the low transmission coefficients of the SWCNT $(5,0)$ at 50-70 meV, which contributes the low thermal conductance of the $(5,0)$ SWCNT above 150 K, shown in the next section. Although Fig. 3-2 shows that the total phonon densities of all models are similar, the transmission coefficient of the SWCNT $(5,0)$ is smaller than those of other SWCNTs at 50-70 meV. This result implies that the transmissions through the normal modes excited in the 50-70 meV region are not perfect for the

SWCNT $(5,0)$. The origin of the inefficient transmission could be a contact asymmetry, where the couplings to the left and right leads are not equal [25]. The contact asymmetry is produced by the localized spatial distribution of normal modes. The localized character of vibrational modes are found as the relatively large contribution from the longitudinal (z) component to the total vDOS of the SWCNT $(5,0)$ shown in Fig. 3-2 and the PNMs' coupling of the $(5,0)$ SWCNT (about 9 meV) that is lower than the other two (about 15 meV) at $\omega^0, \omega =$ 50-70 meV. The number of modes contributing to the inefficient transport in the 50-70 meV range gives a rational explanation for the lower transmission coefficients and accordingly the lower thermal conductance above room temperature.

The PNMs' energy shift in Eq. (3-1) is also shown in Fig. 3-3 (b). In general, the energy shift is not large at $\hbar\omega_q^0$ (along the diagonal line in Fig. 3-3), and hence the effects of the energy shifts on the transmission coefficients are not significant. Furthermore, the energy dependence of the shift is independent of the chirality. The energy shifts of all modes behave like cosine curves through the whole induced energy. The shift has a node at around 130 meV, which coincides with the borderline between the regions of transverse and longitudinal modes. The energy shift is related to the phonon dispersion relation. A positive energy shift indicates that the phonon band has its minimum at the center of the Brillouin zone and, in contrast, a negative shift indicates that the phonon band has its maximum at the center of the Brillouin zone.

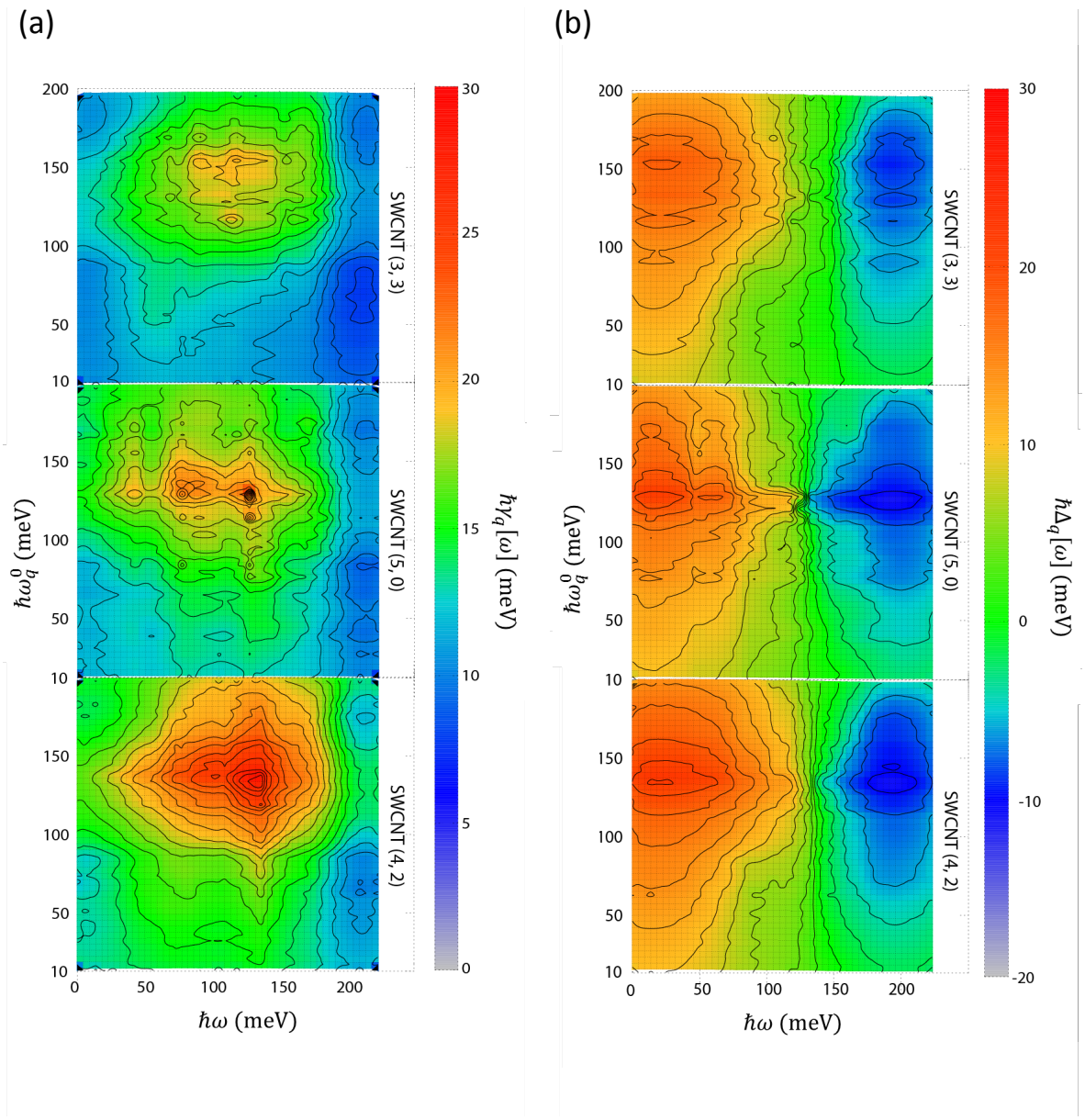

Fig. 3-3. (a) PNM's couplings and (b) PNM's energy shifts of SWCNTs $(3,3)$, $(5,0)$, and $(4,2)$. Their intensities are visualized with the contour lines and colors.

3-3 Thermal conductance

WIDE TEMPERATURE RANGE In Fig. 3-4, the thermal conductances of the SWCNT models are shown over a wide temperature range calculated with Eqs. (2-14) and (2-54). Our results have similar values to the previous works using the first-principles NEGF calculations [28], MD simulations [29], and model calculations ($\sim$2.4 nW/K at 300 K) [30]. In particular, the result of the SWCNT $(7, 0)$ is in good agreement with that of the previous NEGF calculation.

It is shown that the temperature dependence of models varies according to their chiralities at both the low and high temperatures. In the low-temperature region below 150 K, all of the SWCNTs show an almost linear dependence on the temperature, similar to the previous work, although the (3, 3) SWCNT shows a slight change of its slope. This difference corresponds to the trend of the transmission coefficients in the low energy region (0-20 meV) shown in Fig. 3-4. In the next subsection, we will focus on the thermal conductances in the low temperature region with respect to the quantized plateaus.

Above 150 K, the conductance of the SWCNT $(5, 0)$ is much lower than those of the other two models. The previous study showed a linear relationship between the diameter and the thermal conductance, with which the difference in the diameter of our models $(4, 2)$ and $(5, 0)$, viz., 0.29 Bohr corresponds to 0.1 nW/K difference in the thermal conductance. Compared with this, the difference of 0.4 nW/K between the SWCNTs $(4, 2)$ and $(5, 0)$ at 300 K in our result is a little bit larger. It can be concluded that the low thermal conductance of the SWCNT $(5, 0)$ above 150 K is partially due to its chirality, which produces the difference in the transmission coefficients around 50-70 meV investigated in the previous section. On the other hand, the difference of 0.67 nW/K at 300 K between $(5, 0)$ and $(7, 0)$ is fully explained by the difference in the diameters (about 2.8 Bohr) because of their same chiralities.

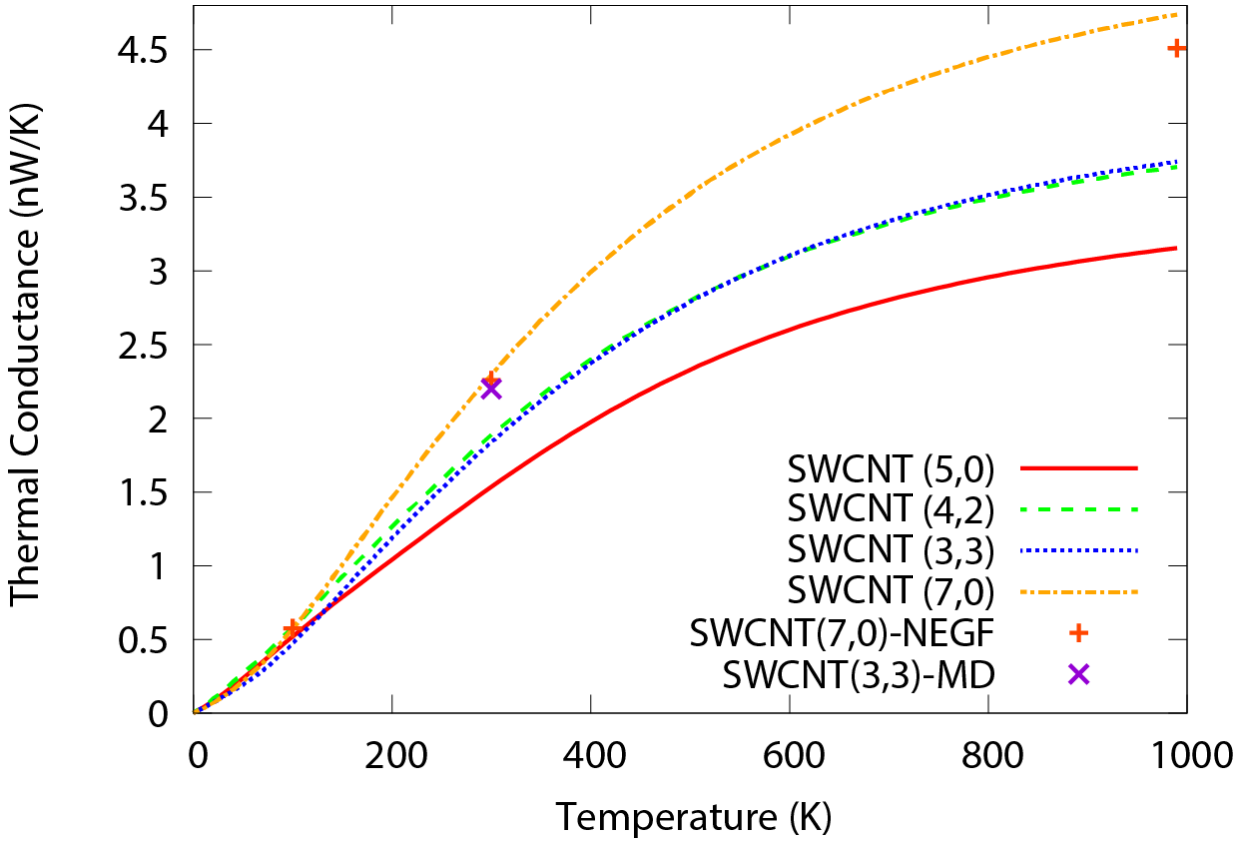

Fig. 3-4. Thermal conductances of SWCNT models including the thick $(7,0)$ one. The previous results of the SWCNT $(7,0)$ [28] and $(3,3)$ [29] are also shown for comparison as cross marks.

LOW TEMPERATURE REGION Finally, the thermal conductance below 100 K is investigated in detail. Because the conductance at low temperature is well quantized, it is convenient to introduce the universal quantum unit $\kappa_0(T)$ defined as,

$$\kappa_0(T) = \frac{\pi {k_B}^2 T}{6\hbar} . \tag{3-2}$$

The universal quantum unit is the single phonon transmission probability under the adiabatic contact assumption. Especially at the low temperature, the quantum unit is equivalent to an asymptotic value of one mode's contribution to the thermal conductance. The thermal conductance normalized by the quantum unit, $\kappa(T)/\left(4\kappa_0(T)\right)$, is shown in Fig. 3-5: a coefficient 4 indicates

the three transverse modes and one twisting mode. The quantized plateau is found as the constant $\kappa(T)/\left(4\kappa_0(T)\right)$, where the temperature dependence of the thermal conductance is linear. The experimental result is also shown [13], whose thermal conductance is divided by the temperature and scaled to 1. For the purpose of the comparison, we also calculated the conductance using the approximated Landauer formula. In this formula, we assume the adiabatic transmission and consider only the branch of the four acoustic modes and those of the two lowest optical modes. For this model calculation, we use the energies of optical modes, $\hbar\omega_{op}^{ext}$, defined in Sec. 3-2. The thermal conductance based on the approximated Landauer formula is given by

$$\kappa(T) = \int_0^\infty \frac{d\omega}{2\pi} 4\hbar\omega \frac{\partial n}{\partial T} + \int_{\omega_{\mathrm{op}}^{\mathrm{ext}}}^\infty \frac{d\omega}{2\pi} 2\hbar\omega \frac{\partial n}{\partial T}. \tag{3-3}$$

As shown in Fig. 3-5, while the result calculated by the approximate Landauer formula does not reproduce the long plateau, the thermal conductance of the SWCNT (3, 3) has a plateau span of 50 K, which is longer than both of those obtained by the approximate Landauer formula and by the experiment. On the other hand, the normalized thermal conductances of the other two SWCNTs do not have clear plateaus and are higher than 1, even in the very low temperature region. The reason is clearly explained by the transmission coefficients, as shown in Sec. 3-2. The transmission coefficient of the SWCNT $(3,3)$ remains 4 in the wide energy range, while those of other two rise to 6 immediately.

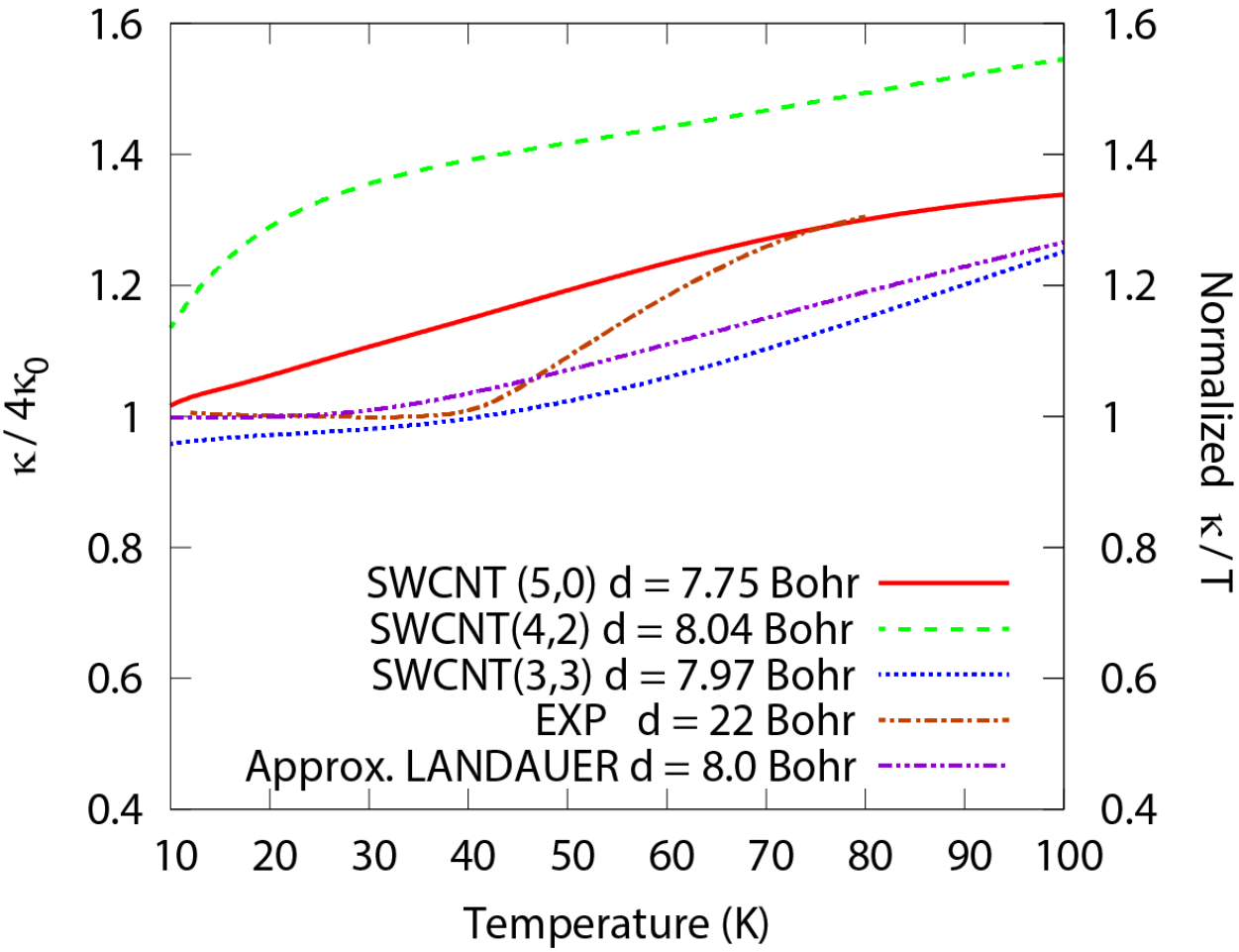

Fig. 3-5. Normalized thermal conductances of SWCNTs. Normalization factor is the universal quantum, $4\kappa_0(T) = 2\pi {k_b}^2 T/3\hbar$. See the text for the details of the approximate Landauer formula. The experimental value is scaled so that the quantized plateau equals 1 [13].

There are two origins of such a difference in the transmission coefficients. As discussed before, one origin is the frequency of the first optical modes $\hbar\omega_{\mathrm{op}}^0$ mentioned in Sec. 3-1. The considerably higher $\hbar\omega_{op}^0$ of the SWCNT $(3,3)$ leads to delaying the contribution of the first optical modes to the transmission coefficient. The other is a chirality-dependent energy coupling, found in Table. 3-1. $\hbar\gamma_{op}[\omega_{op}^0]$ of the SWCNTs $(4,2)$ and $(5,0)$ are larger, thus, the influences of the vDOS of the optical modes appear at lower energies than those of the SWCNT $(3,3)$. Our

first-principles NEGF method explicitly described the chirality dependence of $\hbar\omega_{op}^{0}$ and the phonon-phonon interaction with the semi-infinite heat baths, which results in the long plateau of the thermal conductance, $\sim$50 K, of the armchair SWCNT (n, n).

It is difficult to compare the results of our calculation directly with the experimental results because the diameters of the SWCNTs in our models are not equal to those in experiment. However, we are able to comment on the height of the plateau because a plateau is well reproduced in the (3, 3) SWCNT. If we assume that the effects of the diameter on $\hbar\omega_{op}^{0}$ is less than those from the calculation with the zone-folding method, the armchair SWCNT with the large diameter could still have the long plateau of $4\kappa_0$. On the other hand, our results of the zigzag $(n, 0)$ and chiral (n, m) SWCNTs, where the transmission coefficients quickly become 6, give another possibility. If SWCNTs used in the experiment consist of the zigzag or chiral SWCNTs, gradual slopes around $6\kappa_0$ could be observed as if they were the first quantized plateaus. The plateau will stand during other optical modes with higher energies start to contribute. These possibilities can be investigated by more precise experiments or first-principles calculations for larger SWCNTs.

Finally, we mention the effect of the electronic thermal conductance. The contribution of the conduction electrons is important in typical metal materials at low temperature, and the total thermal conductance is described as Eq. (1-3). For the metallic SWCNTs, $\kappa_c = 4\kappa_0$ because the four electronic states are at the Fermi level. However, because the characteristic energy for electronic excitations is of the order of 0.1 eV, the quantized nature of the thermal conductance caused by electrons survives up to the room temperature. Therefore, κ_c does not affect the length of the quantized plateau of the κ_l and only raise its absolute value by $4\kappa_0$. Deeper understanding about the electronic effects on the quantized plateaus also requires the comparison with the more

detailed experimental results, because the electronic density of states of SWCNTs changes according not only to their chiralities but also to their alignments in the samples. [31, 32]

3-4 Summary

We performed the first-principles calculations of the thermal transport properties of SWCNTs for investigating the chirality dependence. The NEGF method is applied to the three SWCNT models with the different chiralities. The thermal conductance of the models shows the clear dependence on the chirality. The SWCNT $(5,0)$ has lower values above 150 K, which is partially due to the dip in the transmission coefficient in the range 50-70 meV. On the other hand, the thermal conductance of the SWCNT $(3,3)$ is relatively low below 150 K because the energy of its first optical mode is higher than the other SWCNTs.

We also calculate the phonon densities and interactions with semi-infinite heat bathes, in order to understand the thermal conductance and the transmission coefficients from the microscopic point of view. In the range 50-70 meV, the DOS of the SWCNT $(5,0)$ shows that the phonon modes are relatively polarized into the longitudinal direction, and its PNM's coupling is lower than the other two models. With these analyses, it is concluded that the transmission coefficient of the SWCNT $(5,0)$ is suppressed by such localized properties of phonon modes.

The lower thermal conductance of the SWCNT $(3,3)$ at low temperature is also discussed in the context of the quantized plateau. The plateau length of the SWCNT $(3,3)$ results in 50 K, which is longer than that from the approximate Landauer formula. This is because the approximate Landauer formula includes only the radial dependence and does not take into account the effects of the chirality on $\hbar\omega_{\mathrm{op}}^{0}$. Because of the explicit treatment of the parameter-free phonon states and the interactions with the heat bathes, we reproduced the plateau comparable to the experimental result $(40$ K$)$. While this result is consistent with the experimental one, a further analysis using various SWCNTs will be necessary with respect to the absolute values of plateaus because the obtained values can be $4\kappa_0$ and $6\kappa_0$ for the armchair and the other SWCNTs.

Bibliography

[1] Balandin, A. A. (2011). Thermal properties of graphene and nanostructured carbon materials. *Nat. Mat.* 10: 569-581.

[2] Novoselov, K. S.; Geim, A. K.; Morozov, S. V.; Jiang, D.; Katsnelson, M. I.; Grigorieva, I. V.; Dubonos, S. V. and Firsov, A. A. (2005). *Nature* 438: 197-200.

[3] Dekker, C. (1999). Carbon Nanotubes as Molecular Quantum Wires. *Phys. Today* 52: 22-28.

[4] Tans, S. J.; Verschueren, A. R. M. and Dekker, C. (1998). Room-temperature transistor based on a single carbon nanotube. *Nature* 393: 49-52.

[5] Levitsky, I. A. and Euler, W. B. (2003). *Appl. Phys. Lett.* 83: 1857-1859.

[6] Berber, S.; Kwon Y.-K. and Tománek, D. (2000). Unusually High Thermal Conductivity of Carbon Nanotubes. *Phys. Rev. Lett.* 84: 4613-4616.

[7] Hone, J.; Llaguno, M. C.; Nemes, N. M.; Johnson, A. T.; Fischer, J. E.; Walters, D. A.; Casavant, M. J.; Schmidt, J. and Smalley, R. E. (2000). Electrical and thermal transport properties of magnetically aligned single wall carbon nanotube films. *Appl. Phys. Lett.* 77: 666-668.

[8] Kim, P.; Shi, L.; Majumdar, A. and McEuen, P. L. Thermal Transport Measurements of Individual Multiwalled Nanotubes. (2001). *Phys. Rev. Lett.* 87: 215502.

[9] Fujii, M.; Zhang, X.; Xie, H.; Ago, H.; Takahashi, K.; Ikuta, T.; Abe, H. and Shimizu, T. (2005). Measuring the Thermal Conductivity of a Single Carbon Nanotube. *Phys. Rev. Lett.* 95: 065502.

[10] Pop, E.; Mann, D.; Wang, Q.; Goodson, K. and Dai, H. (2006). Thermal Conductance of an Individual Single-Wall Carbon Nanotube above Room Temperature. *Nano Lett.* 6: 96-100.

[11] Blencowe, M. P. (1999). Quantum energy flow in mesoscopic dielectric structures. *Phys. Rev.*

B 59: 4992-4998.

[12] Yamamoto, T.; Watanabe, S. and Watanabe, K. (2004). Universal Features of Quantized Thermal Conductance of Carbon Nanotubes. *Phys. Rev. Lett.* 92: 075502.

[13] Hone, J.; Llaguno, M. C.; Biercuk, M. J.; Johnson, A. T.; Batlogg, B.; Benes, Z. and Fischer, J. E. (2002). Thermal properties of carbon nanotubes and nanotube-based materials. *Appl. Phys. A* 74, 339-343.

[14] Saito, R.; Takeya, T.; Kimura, T.; Dresselhaus, G. and Dresselhaus, M. S. (1998). Raman intensity of single-wall carbon nanotubes. *Phys. Rev. B* 57, 4145-4153.

[15] Tan, Z. W.; Wang, J.-S. and Gan, C. K. (2010). First-Principles Study of Heat Transport Properties of Graphene Nanoribbons. *Nano Lett.* 11: 214-219.

[16] Parlinski, K.; Li, Z. Q. and Kawazoe, Y. (1997). First-Principles Determination of the Soft Mode in Cubic ZrO_2. *Phys. Rev. Lett.* 78: 4063-4066.

[17] Jishi, R. A.; Venkataraman, L.; Dresselhaus, M. S. and Dresselhaus G. (1995). Symmetry properties of chiral carbon nanotubes *Phys. Rev. B* 51: 11176-11179.

[18] Soler, J. M.; Artacho, E.: Gale, J. D.; Garcia, A.; Junquera, J.; Ordejon, P. and Sanchez-Portal, D. J. (2002). The SIESTA method for *ab initio* order-N materials simulation. *Phys. Condens. Mater.* 14: 2745-2779.

[19] Perdew, J. P. and Zunger, A. (1981). Self-interaction correction to density-functional approximations for many-electron systems. *Phys. Rev. B* 23: 5048-5079.

[20] Troullier, N and Martins, J. L. (1991). Efficient pseudopotentials for plane-wave calculations. *Phys. Rev. B* 43: 1993-2006.

[21] Kleinman, L. and Bylander, D. M. (1982). Efficacious Form for Model Pseudopotentials. *Phys. Rev. Lett.* 48: 1425-1428.

[22] Monkhorst H. J. and Pack, J. D. (1976). Special points for Brillouin-zone integrations. *Phys. Rev. B* 13: 5188-5192.

[23] Stokbro, K.; Taylor, J.; Brandbyge, M.; Mozos, J.-L. and Ordejón, P. (2003). Theoretical study of the nonlinear conductance of Di-thiol benzene coupled to Au (111) surfaces via thiol and thiolate bonds. *Comput. Mater. Sci.* 27: 151-160.

[24] Ohto, T.; Yamashita, K. and Nakamura, H. (2011). First-principles study of electronic structure and charge transport at PTCDA molecular layers on Ag (111) and Al (111) electrodes. *Phys. Rev. B* 84: 045417.

[25] Nakamura, H.; Asai, Y.; Hihath, J.; Bruot, C. and Tao, N. (2011). Switch of Conducting Orbital by Bias-Induced Electronic Contact Asymmetry in a Bipyrimidinyl-biphenyl Diblock Molecule: Mechanism to Achieve a pn Directional Molecular Diode *J. Phys. Chem. C* 115: 19931-19938.

[26] Yamamoto, T. and Watanabe, K. (2006). Nonequilibrium Green's Function Approach to Phonon Transport in Defective Carbon Nanotubes. *Phys. Rev. Lett.* 96: 255503.

[27] Savić, I.; Mingo, N. and Stewart, D. A. (2008). Phonon Transport in Isotope-Disordered Carbon and Boron-Nitride Nanotubes: Is Localization Observable? *Phys. Rev. Lett.* 101: 165502.

[28] Mingo, N.; Stewart, D. A.; Broido, D. A. and Srivastava, D. (2008). Phonon transmission through defects in carbon nanotubes from first principles. *Phys. Rev. B* 77: 033418.

[29] Shiomi, J. and Maruyama, S. (2008). Molecular Dynamics of Diffusive-Ballistic Heat Conduction in Single-Walled Carbon Nanotubes. *Jpn. J. Appl. Phys.* 47: 2005-2009.

[30] Yamamoto, T.; Konabe, S.; Shiomi, J. and Maruyama, S. (2009). Crossover from Ballistic to Diffusive Thermal Transport in Carbon Nanotubes. *Appl. Phys. Express* 2: 095003.

[31] Kane, C. L. and Mele, E. J. (1997). Size, Shape, and Low Energy Electronic Structure of Carbon Nanotubes. *Phys. Rev. Lett.* 78: 1932-1935.

[32] Kwon, Y.-K. and Tománek, D. (1998). Electronic and structural properties of multiwall carbon nanotubes. *Phys. Rev. B* 58: R16001-R16004.

CHAPTER 4

MULTI-WALL EFFECTS ON THERMAL TRANSPORT PROPERTEIS OF NANOTUBE STRUCTURES

The characteristic properties of SWCNTs are known to vary greatly depending on the structural factors. As the previous chapter shows the chiralities dependence of the thermal transport properties, these versatile properties of SWCNTs are expected to be controlled by adjusting the molecular structure. At the same time, such beneficial properties are also too sensitive and easily spoiled by defects [1], heating [2], and chemical modifications [3], unfortunately.

One of the promising solutions to overcome the difficulty is stacking, i.e. building multi-walled nanotubes. Recently, numerous experimental methods to achieve stacked structures of low-dimensional nanostructures are developed [4-7], and thus it is expected to control existing properties and build up novel characteristics with such techniques. In the field of CNTs, it is experimentally observed that multi-walled CNTs (MWCNTs) gain more thermal and chemical stability [3] from the inter-layer interaction. At the same time, there are also some reports, where the electronic and thermal properties of CNTs are modified by the stacked structures [8, 9]. In order to elucidate the effects of the inter-layer interaction on these properties, double-walled CNTs (DWCNTs) with the smallest number of layers are an appropriate subject of study. Understanding the impact of the inter-layer interaction in DWCNTs is a stepping-stone towards controlling the physical properties of stacked nanotube systems.

Here, we focus on the multi-wall effects justly on the thermal transport properties of DWCNTs. The magnitude and temperature dependence of the thermal conductance are important for the stability and the thermal efficiency of nano-circuits consisting of nanowires and

nanotransistors [10, 11], and for the quantification of the phonon noise in photosensors [12]. The thermal properties of carbon nanotubes have been investigated mainly with respect to specific heat. It is well known that the specific heat of the SWCNTs is proportional to temperature up to ~ 300 K, which rationalizes the pseudo-1D character of SWCNTs. Meanwhile, in the case of DWCNTs, the specific heat is still monotonic but found to deviate from the 1D character, showing quadratic temperature dependence. The Debye model predicts that the excess degree of freedom in the radial direction causes the $T^{2\sim3}$ temperature dependence of the specific heat [13], and the coupled vibration model suggests that the magnitude of the specific heats is suppressed compared with the SWCNTs [14]. The specific heat of DWCNTs has been discussed in terms of the acoustic modes, but other contributions from the optical modes are also important for small systems at the whole of the temperature range except for the extremely low temperature region [15]. In this work, we perform calculations of the thermal conductance and transmission coefficients of DWCNTs to reveal the mechanism of the multi-walled effects on the thermal transport properties. The all phonon modes are calculated with the empirical force fields, and their contributions to the thermal transports are evaluated with the NEGF formalism.

This chapter is organized as follows. In Sec. 4-1, the computational details and our DWCNT models are introduced. Subsequently, in Sec. 4-2, we show the results of the thermal conductances and transmission coefficients, whose properties are also analyzed based on their phonon modes. In Sec. 4-3, we quantify the multi-walled effects and discuss the mechanism by using the coupled vibration model. Concluding remarks of this chapter are given in Sec. 4-4.

4-1 Computational details

We adopt two DWCNT structures, $(7,7)@(12,12)$ and $(3,3)@(7,7)$, shown in Fig. 4-1. In the notation of MWCNTs, the chirality vectors are combined with @ in an ascending order of their radii. Specifically, $(7,7)@(12,12)$ indicates that DWCNT consist of the inner $(7,7)$ tube and the outer $(12,12)$ tube. To confirm the generality of the multi-wall effects in terms of the tube radius, we prepare the two armchair DWCNTs with different radii. The inter-layer distances of the DWCNTs are set up as 3.3 Å and 2.8 Å for $(7,7)@(12,12)$ and $(3,3)@(7,7)$, respectively, which are relatively close to the inter-layer distance of graphite, 3.4 Å (Table 4-1). SWCNTs $(3,3)$, $(7,7)$, and $(12,12)$ are also considered for reference calculations. We make the periodic unit cell with the conducting (z) direction parallel to the axis of the DWCNT. The lattice parameters along the conducting direction are set to 15 times the minimum periodic length of the armchair CNT structure, that is around 2.46 Å. Sufficient vacuum of about 25 Å is prepared in the non-conducting $(x\text{-}y)$ direction.

First, we perform energy minimizations of the CNT models by using GROMACS (Groningen machine for chemical simulations) [16-20] with the OPLS (optimized potentials for liquid simulations) force field [21]. This potential is given by a summation of the non-bonded interactions and the energies attributed to the structural factors, viz., bonds, angles, and dihedrals.

$$\begin{aligned} E_{\text{total}} &= E_{\text{bond}} + E_{\text{angle}} + E_{\text{dihedral}} + E_{\text{vdW}} + E_{\text{Coulomb}} \\ &= \sum_{\text{bond}} \alpha_i \left(r_i - r_{i,eq}\right)^2 + \sum_{\text{angle}} \beta_j \left(\theta_j - \theta_{j,eq}\right)^2 \\ &+ \frac{1}{2} \sum_{\text{dihedral}} \sum_{l=1}^{4} \gamma_{k,l} \left(1 + (-1)^{l-1} \cos\left(l \cdot \phi_k\right)\right) \\ &+ \sum_{l,m} \varepsilon_{lm} \left[\left(\frac{\sigma_{lm}}{r_{lm}}\right)^{12} - \left(\frac{\sigma_{lm}}{r_{lm}}\right)^{6}\right] + \sum_{l,m} \frac{1}{4\pi\epsilon_0} \frac{\mathcal{Z}_l \mathcal{Z}_m}{r_{lm}}, \end{aligned} \tag{4-1}$$

where r is the bond length, θ the angle, and ϕ the dihedral angle. The eq term indicates the corresponding value for the equilibrium structure. The van deer Waals interaction (vdW) terms are approximated with the Lennard-Jones potential with ε and σ parameters, and the Coulomb interactions are described with the point fixed charges $\mathcal{Z}$. The practical parameters for CNTs are shown in Appendix. We minimize the structures of the DWCNTs from several initial structures with different relative angles between two hexagonal rings of each layer of the DWCNT. The angle is varied by 10 degrees and the two most stable angles are considered in this work (Table 4-1). Then, to confirm that these structures do not rotate randomly below room temperature, MD simulations are performed for $50\,\mathrm{ns}$ at $300\,\mathrm{K}$ by using the Nosé-Hoover thermostat [22, 23]. It is confirmed that all of these structures are stable at the adopted relative angles; therefore, we use these two stable structures in the calculations of thermal conductance.

Table. 4-1. Structural information of the SWCNTs and DWCNTs. *N, d,* and l_z are respectively the number of atoms, diameter, and the (z) length of the unit cell of the models. The two most stable relative angles between two hexagonal rings of each layer of the DWCNTs are also shown.

	N	*d*	l_z	1st stable	2nd stable
		(Ang)	(Ang)	(deg)	(deg)
SWCNT $(3,3)$	180	4.02	36.9	-	-
SWCNT $(7,7)$	420	9.50	36.9	-	-
SWCNT $(12,12)$	720	16.2	36.9	-	-
DWCNT $(3,3)@(7,7)$	600	9.50	36.9	340	140
DWCNT $(7,7)@(12,12)$	1140	16.2	36.9	70	200

In the NEGF calculations, we assume that the length of each of the three respective regions (left, center, and right) is 5 times the minimum periodic length. The infinitesimal parameter η in Eq. (2-27) is set to 1×10^{-5} meV.

(a) DWCNT (7, 7)@(12, 12)

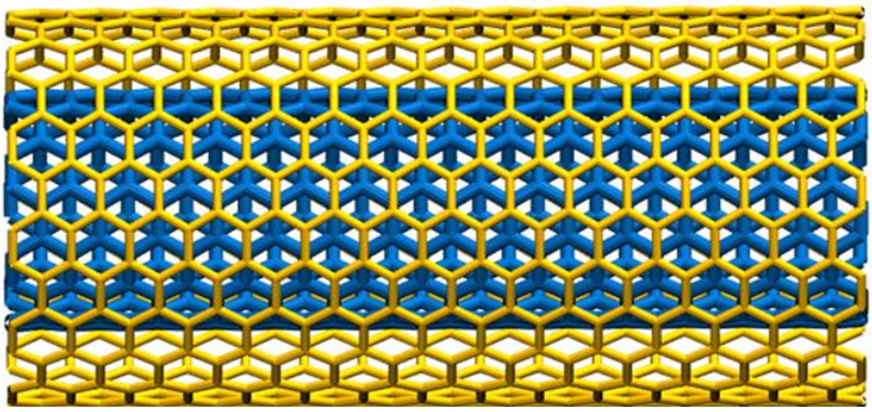

(b) DWCNT (3, 3)@(7, 7)

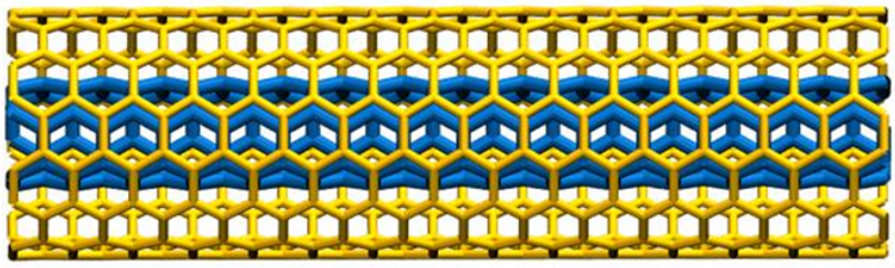

Fig. 4-1. Stable atomic structures of DWCNTs (a) (7, 7)@(12, 12) and (b) (3, 3)@(7, 7). The layer with yellow (thin) bonds is the outer tube and that with the blue (thick) bond is the inner tube.

4-2 Thermal transport properties

THERMAL CONDUCTANCE First, we calculate the temperature dependence of the thermal conductance of the CNT models. The results for the DWCNT $(7,7)@(12,12)$ are shown in Fig. 4-2. The thermal conductance values of the two DWCNTs with different relative angles are almost identical, which indicates that the effect of the relative angle is not dominant.

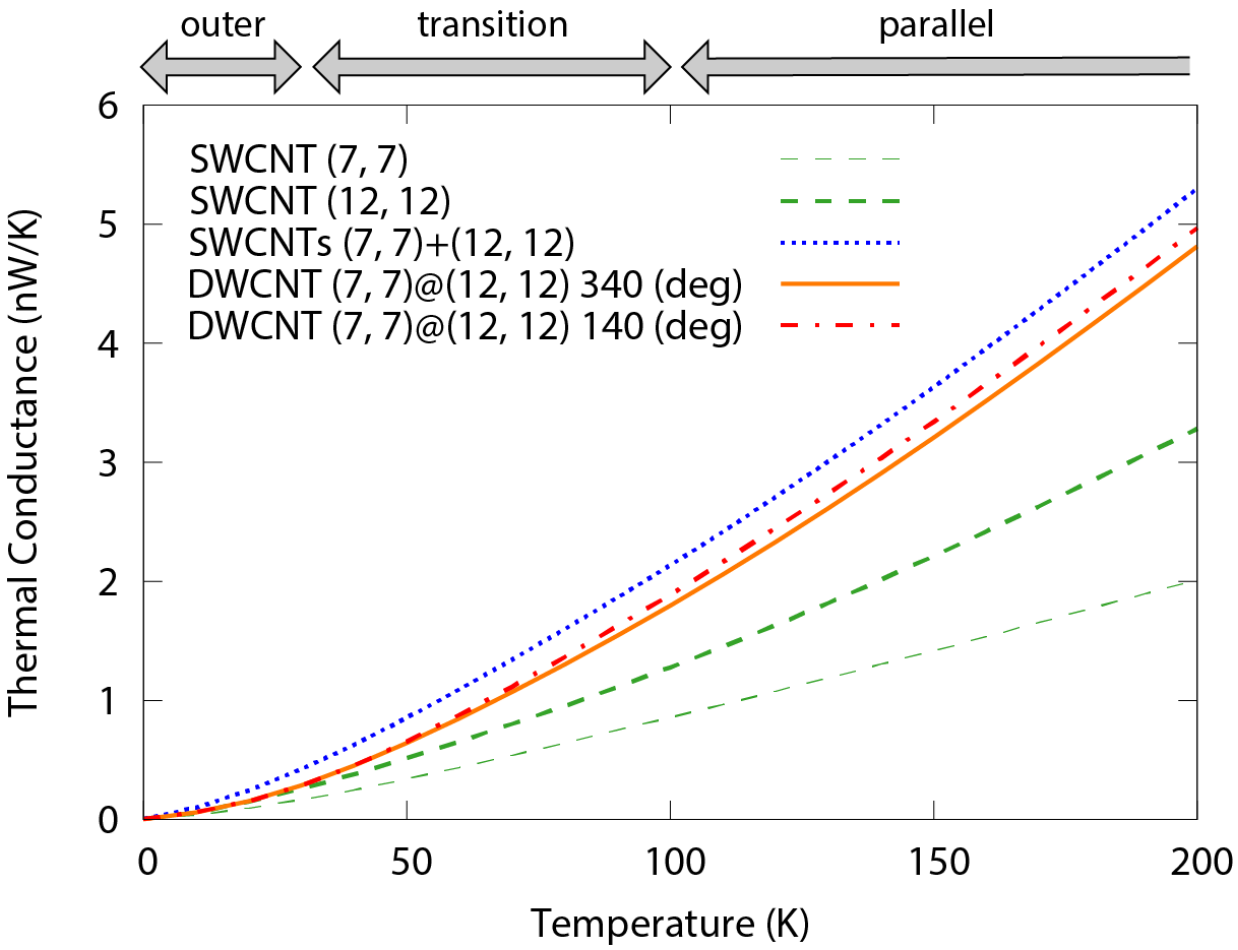

Fig. 4-2. Thermal conductance of DWCNT (7, 7)@(12, 12) with two relative angles and SWCNTs (7, 7), (12, 12), and (7, 7)+(12, 12). SWCNTs (7, 7)+(12, 12) represents the parallel circuit of SWCNTs (7, 7) and (12, 12). The three regions indicated by the arrows on top represent: from the left, the outer layer region (0-30 K), the transition region (30-100 K), and the parallel region (100-200 K).

The thermal conductance values of the SWCNTs $(7,7)$, $(12,12)$, and $(7,7)+(12,12)$ are also shown in Fig. 4-2. The results of the SWCNTs (7, 7)+(12, 12) is calculated as the sum of those of the SWCNTs $(7,7)$ and $(12,12)$, which corresponds to the virtual system, where the SWCNTs $(7,7)$ and $(12,12)$ compose an ideal parallel circuit without any interactions with each other. Thus we can see the impact of inter-layer interaction between two CNTs comparing them with the DWCNTs.

At low temperature (0-100 K), the curvature of the thermal conductance of the DWCNT $(7,7)@(12,12)$ is clearly larger than those of the SWCNTs, in other words, it has a quadratic temperature dependence. This result agrees well with the temperature dependence of specific heats in the previous studies [13, 24]. The DWCNT $(7,7)@(12,12)$ is found to have the lower thermal conductance than the SWCNTs $(7,7)+(12,12)$. This suppression is attributed to the inter-layer van der Waals interactions, analogous with SWCNT bundles, whose thermal conductivities are attenuated by inter-tube van der Waals interactions [25]. At very low temperature, (0-30 K), the thermal conductance of the DWCNT $(7,7)@(12,12)$ behaves as that of the outer tube, namely, the SWCNT $(12,12)$. Yet in the higher temperature region $(100\text{-}200\ \mathrm{K})$, the temperature dependence of the DWCNT $(7,7)@(12,12)$ and SWCNTs $(7,7)+(12,12)$ are identical, viz., parallel within 5% gradient error.

In Fig. 4-3, we show the thermal conductance of the DWCNT $(3,3)@(7,7)$, together with the results of the SWCNTs $(3,3)$, $(7,7)$, and $(3,3)+(7,7)$. The thermal conductance of the SWCNTs $(3,3)+(7,7)$ is obtained in the same way as that of the SWCNTs $(7,7)+(12,12)$. We can see that the trends in Fig. 4-3 are fully consistent with the case of the DWCNT $(7,7)@(12,12)$, namely, the identical behavior of the two DWCNTs with different relative angles, the quadratic temperature dependence in the DWCNTs, and the suppression of the thermal

conductance of DWCNTs compared with that of the parallel circuit SWCNTs. At very low temperature (0-100 K), the thermal conductance of the DWCNT $(3,3)@(7,7)$ behaves like that of the outer SWCNT $(7,7)$. In addition, the differences between the thermal conductance of the DWCNT $(3,3)@(7,7)$ and SWCNTs $(3,3)+(7,7)$ are almost constant at 150-200 K.

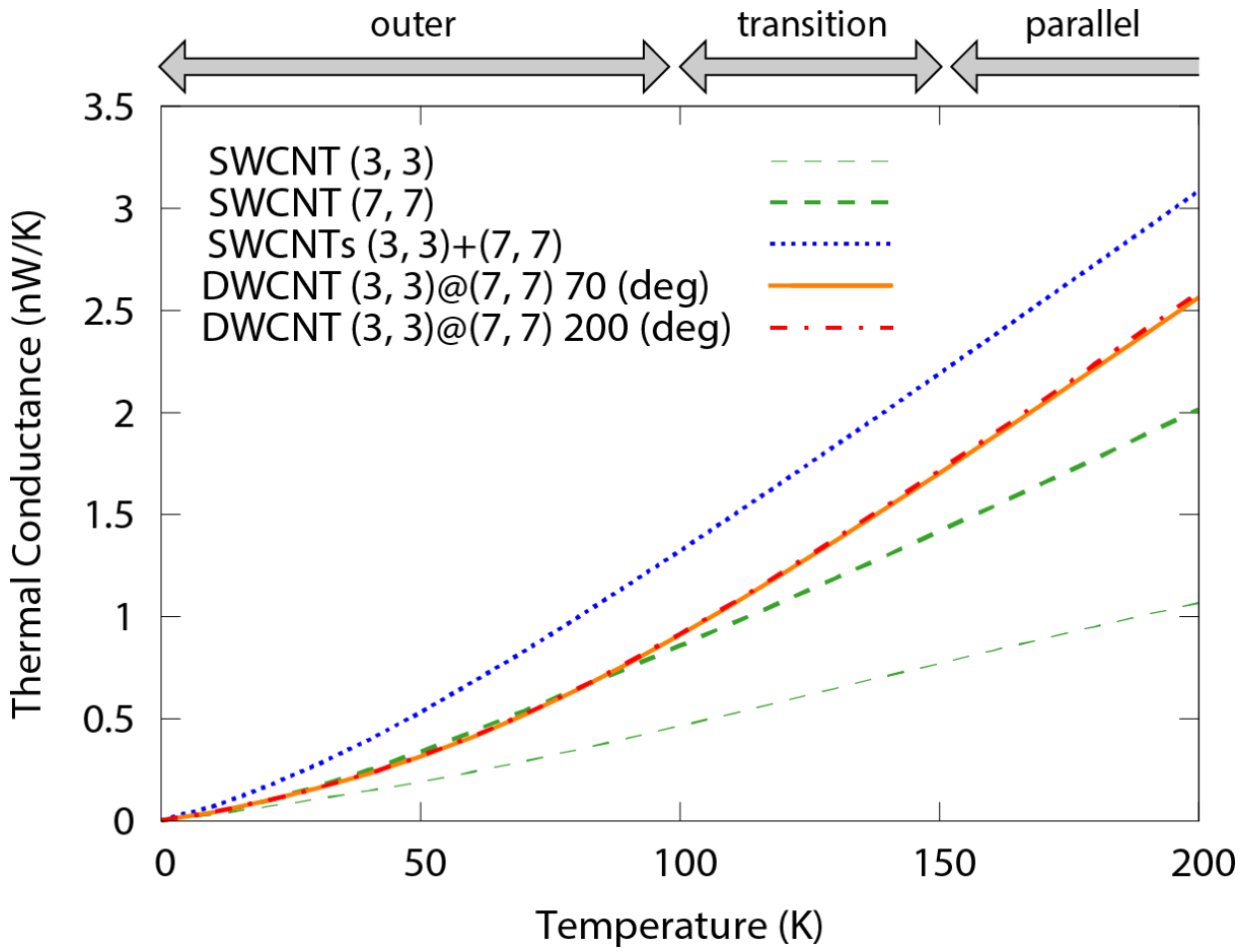

Fig. 4-3. Thermal conductance of DWCNT (3, 3)@(7, 7) with two relative angles and the SWCNTs (3, 3), (7, 7), and (3, 3)+(7, 7). The three regions indicated by the arrows on top represent: from the left, the outer layer region (0-100 K), the transition region (100-150 K), and the parallel region (150-200 K).

Given the above results, it is concluded that the thermal conductance of DWCNT generally consists of three regions with different temperature tendencies: low-temperature region governed by the outer layer (named the outer layer region), a higher-temperature region behaving like a parallel circuit of SWCNTs (the parallel region), and a transition region between the two former regions. In the following discussion, we just focus on the DWCNT (7, 7)@(12, 12) with the most stable relative angle because of the less importance of their radii and relative angles.

TRANSMISSION COEFFICIENTS In Fig. 4-4, we show the transmission coefficient of the DWCNT $(7,7)@(12,12)$ given by Eq. (2-54) with those of the SWCNTs $(7,7)$, $(12,12)$, and $(7,7)+(12,12)$. The transmission coefficients of the SWCNTs $(7,7)+(12,12)$ are also defined as the summation of those of $(7,7)$ and $(12,12)$.

Comparing between the DWCNT $(7,7)@(12,12)$ and SWCNTs $(7,7)+(12,12)$, the transmission coefficient of the former is different from that of the later especially in the low energy region (0-50 meV), while these values are almost identical at the higher energy region. Assuming that incident phonons are transported via the modes with similar energies, the results indicate that the conduction passes through low-energy modes are largely affected by the inter-layer interaction in DWCNTs. Moreover, the transmission coefficient of the DWCNT $(7,7)@(12,12)$ is suppressed into that of SWCNT $(12,12)$ at the low energy region. Considering that the occupancy of phonons obeys the Bose-Einstein statistics, the suppression of the transmission coefficient at the low energy region explains that the thermal conductance of the DWCNT gradually changes from the outer layer region to the parallel region with temperature increase.

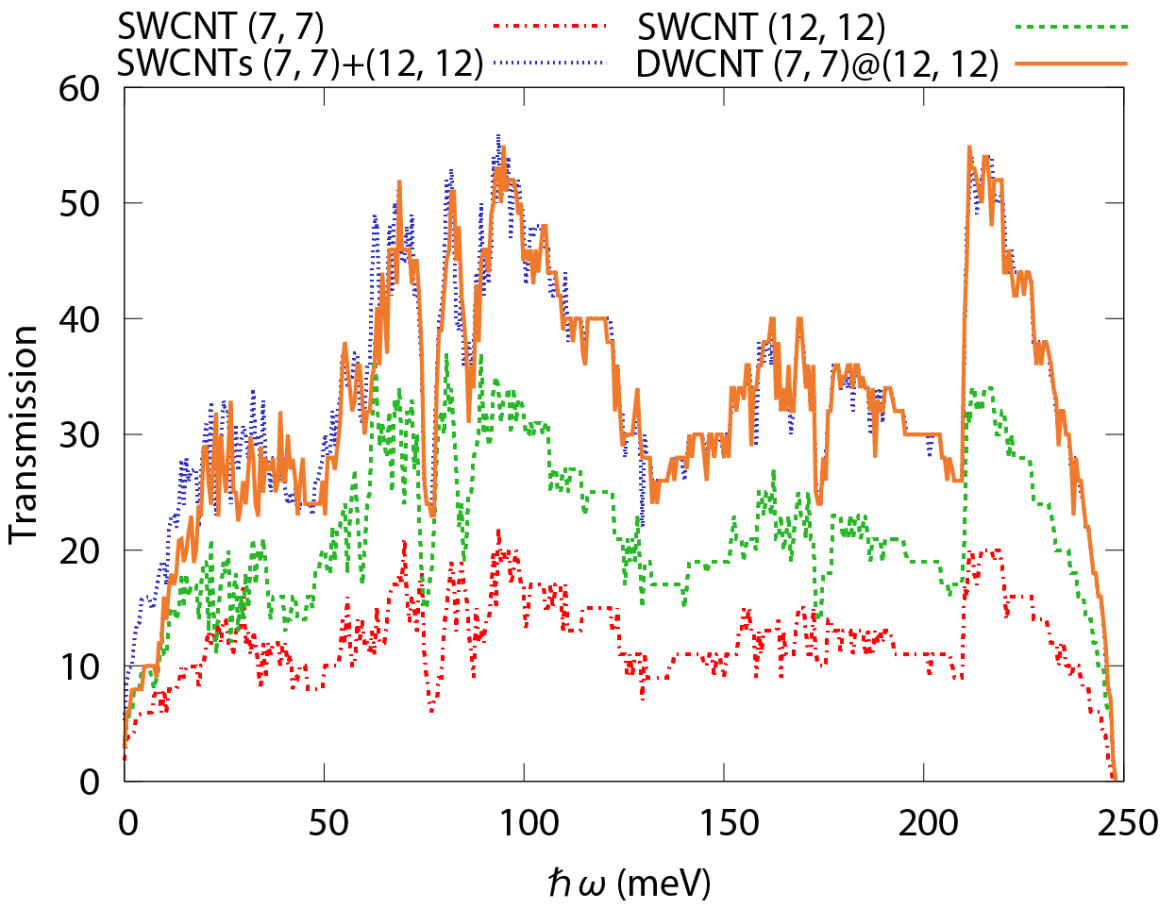

Fig. 4-4. Transmission coefficients of DWCNT $(7,7)@(12,12)$ and SWCNTs $(7,7)$, $(12,12)$, and $(7,7)+(12,12)$. The results of SWCNTs (7, 7)+(12, 12) are calculated as the sum of SWCNTs (7, 7) and (12, 12).

Next, we also compare the energy distribution of the normal modes about the DWCNT $(7,7)@(12,12)$ and SWCNTs $(7,7)+(12,12)$ (Fig. 4-5). The number of modes of the DWCNT $(7,7)@(12,12)$ is less than that of the SWCNTs $(7,7)+(12,12)$ at 0-25 meV, while the opposite is true at 25-50 meV. It indicates that the phonon modes of the DWCNTs shift toward higher energy compared with those of the parallel SWCNTs. Considering that the thermal transmission coefficients are deeply related with the distribution of the phonon modes, the characteristic suppression in the transmission coefficients of the DWCNTs is ascribed to the energy shifts of the phonon modes at the low energy region.

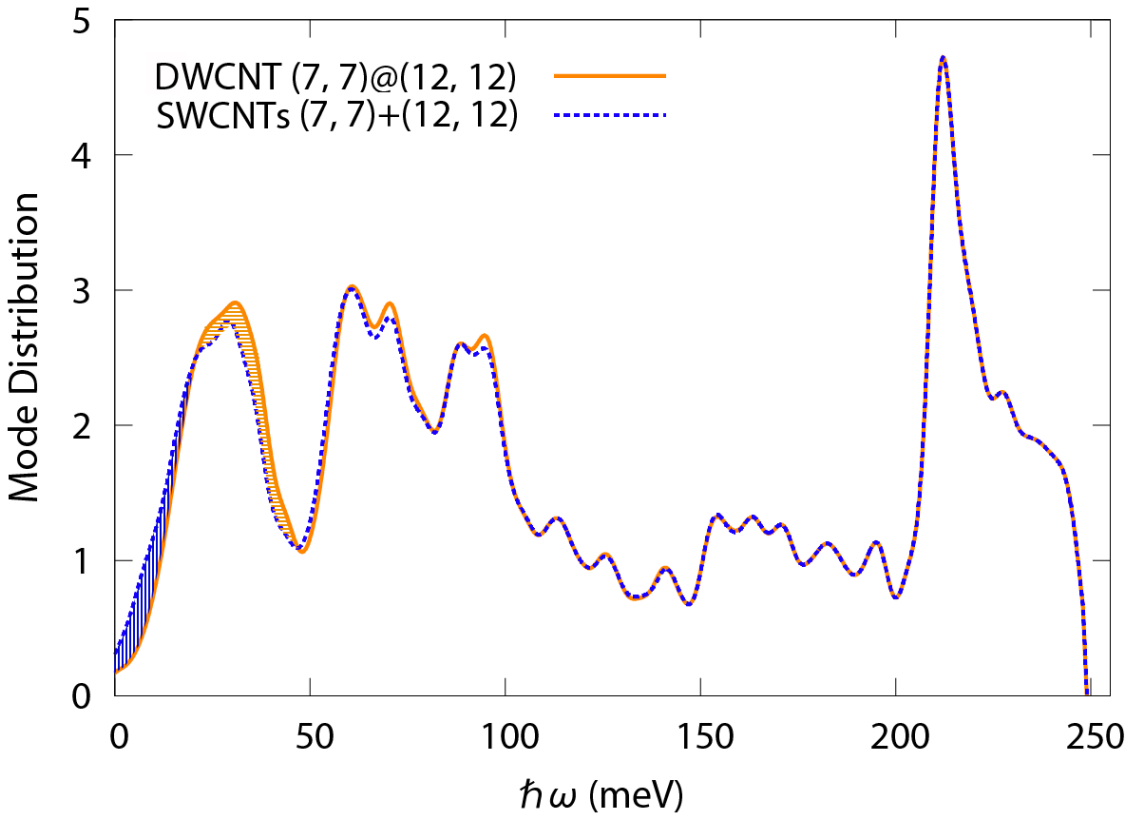

Fig. 4-5. Energy distribution of phonon modes about DWCNT $(7,7)@(12,12)$ and SWCNTs $(7,7)+(12,12)$. The standard deviation $2.5\ \mathrm{meV}$ in Gaussian functions is set for broadening.

NORMAL MODE ANALYSIS We analyze the phonon modes of the DWCNT $(7,7)@(12,12)$ to elucidate the origin of the mode shift in DWCNTs. Assuming that the normal modes of the DWCNT can be considered as a combination of the two single SWCNTs, the polarization vectors of $(7,7)@(12,12)$ are described in terms of the interactions between those of the SWCNTs $(7,7)$ and $(12,12)$. First, we remark on the acoustic modes. The translational and rotational modes of the DWCNT are composed of those of the inner and outer layers in a symmetric *in-phase* relationship, which is consistent with the argument in the previous study [14]. Furthermore, in the higher energy region 0-50 meV, there are a large number of phonon mode, where the vibrations of

the inner and outer layers are in a symmetric *in-phase* or *out-phase* relationship, shown in Fig. 4-6 (a) and (b) respectively. We separate these normal modes of the DWCNT $(7,7)@(12,12)$ into the outer and inter contributions and assign them to the modes of the SWCNTs $(7,7)$ and $(12,12)$, whose energies are compared with the original modes of the DWCNTs (Table 4-2). The energy of the *in-phase* modes is close to that of the normal modes corresponding to the outer SWCNT $(12,12)$, while the *out-phase* modes have higher energy than both of the SWCNTs $(7,7)$ and $(12,12)$.

The mode shifts in DWCNTs shown above are attributed to the fact that the transverse modes are dominant at low energy. DWCNTs have energy barriers in the transverse direction because of their walled structures. The *out-phase* modes blocked by the barriers and shift to higher energy, whereas the *in-phase* modes remain at low energy. Conversely at the higher energy region above $50\ \mathrm{meV}$, the transverse modes are not dominant; thus, the inter-layer interaction is negligible. Therefore, no mode shift is observed there. This point is taken up again in the following discussion.

Table. 4-2. Energy of the modes: from the left, the modes assigned to the outer and inner layers, the normal modes of DWCNT $(7,7)@(12,12)$, and the results of the model calculation with the coupled vibration model.

	outer layer	inner layer	DWCNT	Model ($\lambda_{\pm}$)
	(meV)	(meV)	(meV)	(meV)
in-phase acoustic mode	0	0	0	
out-phase acoustic mode	0	0	10.3	
in-phase mode (Fig. III-6 a)	9.03	8.35	8.83	8.77
out-phase mode (Fig. III-6 b)	9.03	8.35	13.4	14.3

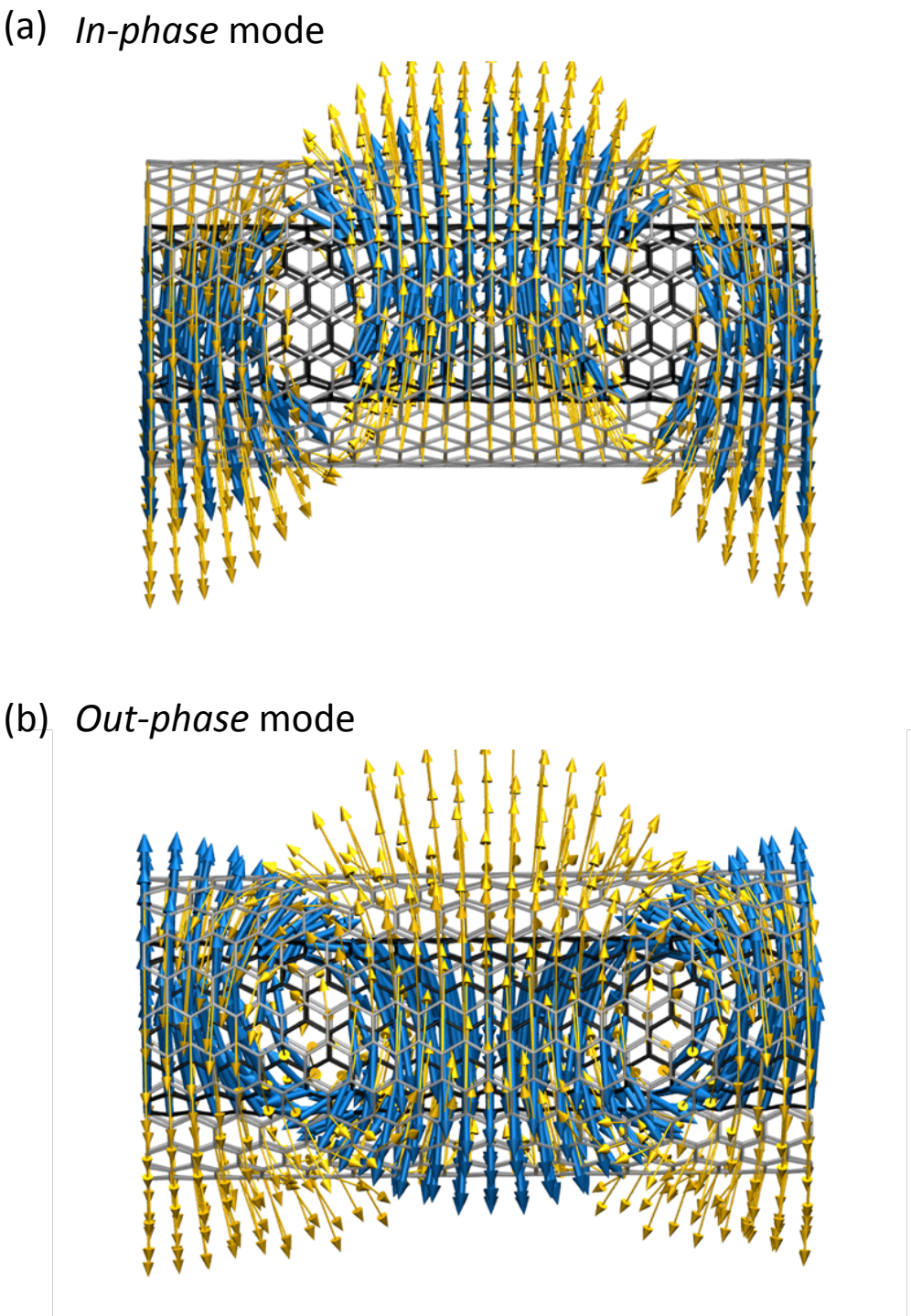

Fig. 4-6. Schematics of typical (a) *in-phase* mode and (b) *out-phase* mode. These modes result from the fact that transverse modes of inside and outside layers are coupled via inter-layer interactions.

4-3 Coupled vibration description

In Sec. 3-2, we show that the transmission coefficient of the DWCNT reduces to that of the outer SWCNT at the low energy region because the energies of phonon modes are shifted by the inter-layer interactions. To understand further the mechanism of such energy shifts, we apply the coupled vibration model to our results [14, 26]. In this model, the normal modes of the DWCNT are described as the outer layer modes, $m_{out}\ddot{c}_{out} = -k_{out}c_{out}$ and inner layer modes, $m_{in}\ddot{c}_{in} = -k_{in}c_{in}$ are coupled by the coupling constant ζ originating from the inter-layer van der Waals interaction. The whole equation of motions are given by

$$\begin{aligned} m_{out}\ddot{c}_{out} &= -k_{out}c_{out} - \zeta(c_{out} - c_{in}), \\ m_{in}\ddot{c}_{in} &= -k_{in}c_{in} + \zeta(c_{out} - c_{in}), \end{aligned} \tag{4-2}$$

where $m_{out(in)}$ is the atomic mass, $c_{out(in)}$ the displacement, and $k_{out(in)}$ the force constant of the corresponding normal mode of the isolated outer (inner) layer.

First, we apply this model to the *in-phase* and *out-phase* modes shown in Fig. 4-6 to validate the coupled vibration model. The dynamical matrix of the whole system $\boldsymbol{D}$ is expressed as follows:

$$\boldsymbol{D} = \begin{pmatrix} \dfrac{k_{out} + \zeta}{m_{out}} & \dfrac{\zeta}{\sqrt{m_{out}m_{in}}} \\ \dfrac{\zeta}{\sqrt{m_{out}m_{in}}} & \dfrac{k_{in} + \zeta}{m_{in}} \end{pmatrix}. \tag{4-3}$$

Assuming that $m_{out(in)}$ are proportional to the tube's diameter (see Table 4-1), they are defined as $m_{out} = 16.2\,m$, $m_{in} = 9.50\,m$ using an arbitrary constant m. Then, we obtain $k_{out(in)}$ from the vibrational energies $\omega_{out(in)}$ of the modes assigned to the SWCNTs (see Table 4-2) with the relation: $\omega_{out(in)} = \sqrt{k_{out(in)}/m_{out(in)}}$. The off-diagonal term of $\boldsymbol{D}$, namely, $\zeta/\sqrt{m_{out}m_{in}}$ is

extracted from the off-diagonal term of the DWCNT dynamical matrix projected onto the eigenvectors of each layer as

$$\begin{pmatrix} OUTER\ EIGEN\ VECTOR & 0 \\ 0 & INNER\ EIGEN\ VECTOR \end{pmatrix}^{-1} \begin{pmatrix} DWCNT\ DYNAMICAL\ MATRIX \end{pmatrix} \begin{pmatrix} OUTER\ EIGEN\ VECTOR & 0 \\ 0 & INNER\ EIGEN\ VECTOR \end{pmatrix} = \begin{pmatrix} {\omega_{out}}'^2 & \frac{\zeta}{\sqrt{m_{out}m_{in}}} \\ \frac{\zeta}{\sqrt{m_{out}m_{in}}} & {\omega_{in}}'^2 \end{pmatrix}. \quad (4\text{-}4)$$

For the modes shown in Fig. 4-6, the assigned modes of each layer degenerate with the orthogonal modes. To obtain the coupling constant between modes in a uniform direction, we pick up and diagonalize a corresponding 2×2 matrix between the two degenerated modes of each layer. As a result, we obtain a coupling constant as $\gamma/\sqrt{m_{out}m_{in}} = 63.4\ \mathrm{meV^2}$. The vibrational energy resulting from the coupling is evaluated by the diagonalization of the matrix in Eq. (4-3) and is given by

$$\lambda_{\pm} = \sqrt{\frac{1}{2}\left(\Omega \pm \sqrt{\Omega^2 - 4\left({\omega_{out}}^2{\omega_{in}}^2 + {\omega_{out}}^2\frac{\zeta}{m_{in}} + {\omega_{in}}^2\frac{\zeta}{m_{out}}\right)}\right)}, \quad (4\text{-}5)$$

$$\Omega = {\omega_{out}}^2 + {\omega_{in}}^2 + \frac{\zeta}{\mu}, \qquad \mu = \frac{m_{out}m_{in}}{m_{out} + m_{in}}$$

where μ is the reduced mass. We show the resulting values in Table 4-2. The values of λ_- and λ_+ (8.77 and 14.3 meV) reproduce our simulation results well (8.83 and 13.4 meV), whereas λ_+ is slightly overestimated by 1 meV. Therefore, the coupled vibration model reproduces the energy shifts in the DWCNT modes and is appropriate for explaining our results.

Next, we investigate the dependence of the coupled vibrational energies $\lambda_{\pm}$ on the coupling constant ζ. In the following, it is assumed that $\omega_{out} > \omega_{in}$, but even in the opposite case the discussion below holds the generality. When $\zeta \longrightarrow 0$, the system corresponds to the ideal parallel circuit, thus λ_- and λ_+ are equal to ω_{in} and ω_{out}, respectively. On the other hand, it is

found that $\lambda_{\pm}$ monotonically increase with respect to ζ and λ_{-} converges to a finite value when $\zeta \longrightarrow \infty$. The range of λ_{-} is

$$\omega_{in} \leq \lambda_{-} \leq \sqrt{\frac{m_{out}}{m_{out}+m_{in}}{\omega_{out}}^{2} + \frac{m_{in}}{m_{out}+m_{in}}{\omega_{in}}^{2}} \equiv \lambda_{-}^{max}, \tag{4-6}$$

where λ_{-}^{max} is an upper limit of λ_{-} and depends on the vibration energies of two layers via the scaling factor, $m_{(out,in)}/(m_{out}+m_{in})$, thus becoming closer to the vibrational energy of the heavier layer. The convergence of λ_{-} with increasing ζ is rapid and is nearly converged ($\lambda_{-} \geq 0.88\,\lambda_{-}^{max}$) for the significant couplings, $\zeta/\sqrt{m_{out}m_{in}} \geq 20$ meV^2. This trend explains that the low-energy normal mode distribution of DWCNTs is consistent with that of the outer layer, as shown in Figs. 4-4 and 4-5, hence resulting in the outer-layer region of the thermal conductance in Figs. 4-2 and 4-3. In contrast, as mentioned above, the energy shift of the DWCNT is negligible at the higher energy region (> 50 meV). Most of the vibrational modes with such energy regions include longitudinal components along the z-axis, vis., orthogonal to the inter-layer direction (in the x-y plane), and the couplings between the inner and outer layers are small. In that case, $\lambda_{\pm}$ are not shifted far from $\omega_{out(\,in)}$.

From the discussions, we can provide one principle: the thermal conductance of the multi-walled tubular structure is governed by the heavier layer especially at low temperature, and such tendency becomes prominent as the difference in the mass of layers increases. This rule is confirmed by the calculation of the thermal conductance for the triple-walled system, MWCNT $(3,3)@(7,7)@(12,12)$, whose results are shown in Fig. 4-7. We can confirm that even when the number of layers is more than two, the thermal conductance at low temperature is similar to that of the heaviest layer. That is, the conductance of the MWCNT $(3,3)@(7,7)@(12,12)$ are comparable to that of the SWCNT $(12,12)$ at very low temperature (0-40 K). At higher

temperature (40-90 K), the thermal conductance of the MWCNT begins to accommodate that of the second heaviest layer, SWCNT $(7,7)$ and eventually follows that of the DWCNT $(7,7)@(12,12)$. It is expected that this principle enables us to design the desired thermal properties by the multi-wall effects.

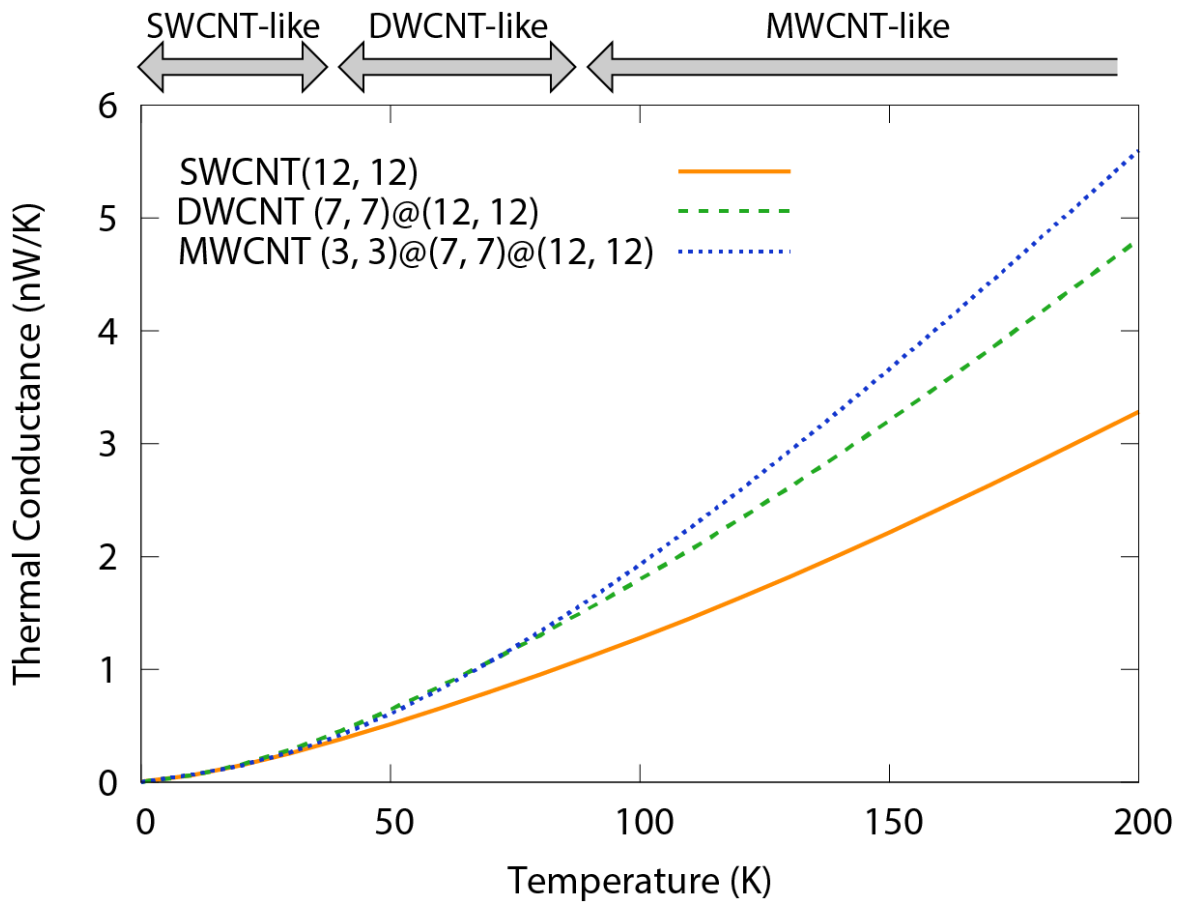

Fig. 4-7. Thermal conductance of MWCNT $(3,3)@(7,7)@(12,12)$, with that of DWCNT $(7,7)@(12,12)$ and SWCNT $(12,12)$. The three regions indicated by the arrows on top represent: from the left, the SWCNT $(12,12)$-like region (0-40 K), the DWCNT $(7,7)@(12,12)$-like region (40-90 K), and the higher region.

4-4 Summary

MULTI-WALL EFFECTS We studied the multi-wall effects on the thermal conductance of nanotube structures by means of the NEGF methods, focusing on DWCNTs. It is found that the thermal conductance of the DWCNT is suppressed into one of the outer layer and has quadratic temperature dependence at the low temperature region, comparing with the thermal conductance of the single SWCNTs and the ideal parallel circuit of them. In contrast, at higher temperature, the DWCNT is considered as the ideal parallel circuit and the quadratic behavior vanishes. This trend is universal with respect to the radius and the relative angle between two layers. The suppression at the low temperature region is attributed to the energy shifts of the normal modes at the low energy region. Normal mode analysis shows that the symmetric modes of the inner and outer layers are coupled and split into the *in-phase* and *out-phase* modes. The energy of the *in-phase* mode is close to the energy of the corresponding mode of the outer layer, while the *out-phase* mode lies at a higher energy.

The coupled vibration model attributed the origin of such mode shift to the coupling between inner- and outer-layer modes. The energy shift in the DWCNT is reproduced precisely by the extracted coupling constants from our simulations. This model also reveals that the energy of the *in-phase* coupled mode is close to the outer one because of the mass difference between two layers. That is, the heavier layer governs the thermal conductance of a stacked nanotube system at the low temperature region. This trend is also confirmed in the case of the triple-walled carbon nanotube system.

CONTROL STRATEGIES Comparing between the chirality dependence and multi-wall effects, the latter is thought to be convenient and practicable for thermal design. While the chirality of

CNTs affects on the thermal transport properties, the rearrangement of chemical bonds rather changes the other properties, in particular, electronic properties. Such drastic modification hinders the selective control of thermal properties. On the other hand, multi-walled structure modifies their properties via the non-bonded interactions. Such weak interactions often have little impact on the electrons with high energies and rather modify the vibrational properties with low energies, which makes the independent thermal design possible. The coupled vibrational description also provides the definite guideline to do it.

Specifically, we expect that thermal conductance of walled tubular structures could be tailored by controlling the mass of each layer. It is feasible to design new nano-materials with superior thermal efficiency by combining a heavier nanotube with excellent thermal transport properties and a lighter layer with desirable properties. For lighter layers, Si and TiO_2 nanotubes are promising materials for secondary batteries [27] and solar cells [28]. On the other hand, ceramics such as boron nitride, aluminum nitride, and silicon carbide are relatively heavy and thermally conductive, and thus ceramic nanotubes should be appropriate materials for heavier layers. Diamond tubes and moissanite tubes might also be candidates for such applications. The above results suggest that we can theoretically predict the thermal properties of composite tubes made of these candidates.

Appendix

The OPLS parameters for CNTs are the following, shown in the .itp file format in GROMACS.

```
[ atomtypes ]
   C       6       12.0110     0.000      A   3.55000e-01   2.92880e-01
   H       1       1.00800     0.000      A   2.42000e-01   1.25520e-01

[ bondtypes ]
   C       C                              1   0.14000       392459.2
   C       H                              1   0.10800       307105.6

[ angletypes ]
   C       C       C                      1   120.000       527.184
   C       C       H                      1   120.000       292.880
   H       C       H                      1   117.000       292.880

[ dihedraltypes ]
   C       C       C       C              3       30.33400    0.00000   -30.33400   0.00000
                                           0.00000   0.00000
   H       C       C       H              3       30.33400    0.00000   -30.33400   0.00000
                                           0.00000   0.00000
   H       C       C       C              3       30.33400    0.00000   -30.33400   0.00000
                                           0.00000   0.00000
```

Bibliography

[1] Park, J.; Bifano, M. F. P. and Prakash, V. (2013). Sensitivity of thermal conductivity of carbon nanotubes to defect concentrations and heat-treatment. *J. Appl. Phys.* 113: 034312.

[2] Sun, C. Q.; Bai, H. L.; Tay, B. K.; Li, S. and Jiang, E. Y. (2003). Dimension, Strength, and Chemical and Thermal Stability of a Single C−C Bond in Carbon Nanotubes. *J. Phys. Chem. B* 107: 7544-7546.

[3] Shen, C.; Brozena, A. H. and Wang, Y. H. (2011). Double-walled carbon nanotubes: Challenges and opportunities. *Nanoscale* 3: 503-518.

[4] Dean, C. R.; Young, A. F.; Meric, I.; Lee, C.; Wang, L.; Sorgenfrei, S.; Watanabe, K.; Taniguchi, T.; Kim, P.; Shepard, K. L. and Hone J. (2010). Boron nitride substrates for high-quality graphene electronics. *Nat. Nanotechnol.* 5: 722-726.

[5] Hiraoka, T.; Kawakubo, T.; Kimura, J.; Taniguchi, R.; Okamoto, A.; Okazaki, T.; Sugai, T.; Ozeki, Y.; Yoshikawa, M. and Shinohara, H. (2003). Selective synthesis of double-wall carbon nanotubes by CCVD of acetylene using zeolite supports. *Chem. Phys. Lett.* 382: 679-685.

[6] Kitaura, R.; Imazu, N.; Kobayashi, K. and Shinohara, H. (2008). Fabrication of Metal Nanowires in Carbon Nanotubes via Versatile Nano-Template Reaction. *Nano Lett.* 8: 693-699.

[7] Kim, Y. A.; Hayashi, T.; Fukai, Y.; Endo, M.; Yanagisawa, T. and Dresselhaus, M. S. (2002). Effect of ball milling on morphology of cup-stacked carbon nanotubes. *Chem. Phys. Lett.* 355: 279-284.

[8] Okada, S. and Oshiyama, A. (2003). Curvature-Induced Metallization of Double-Walled Semiconducting Zigzag Carbon Nanotubes. *Phys. Rev. Lett.* 91: 216801.

[9] Popov, V. N. (2004). Theoretical evidence for $T^{1/2}$ specific heat behavior in carbon nanotube

systems. *Carbon* 42: 991-995.

[10] Che, J.; Çagin, T. and Goddard, W. A. III (2000). Thermal conductivity of carbon nanotubes. *Nanotechnology* 11: 65-69.

[11] Chen, D.; Chilstedt, S.; Dong, C. and Pop, E. (2010). What everyone needs to know about carbon-based nanocircuits. *Proc. 47th Design Automation Conf.* 1-18.

[12] Blencowe, M. P. (1999). Quantum energy flow in mesoscopic dielectric structures. *Phys. Rev. B* 59: 4992-4998.

[13] Benedict, L. X.; Louie, S. G. and Cohen, M. L. (1996). Heat capacity of carbon nanotubes. *Solid State Comm.* 100: 177-180.

[14] Damnjanović, M.; Dobardžić, E.; Milošević, I.; Vuković, T. and Nikolić, B. (2003). Lattice dynamics and symmetry of double wall carbon nanotubes. *New J. Phys.* 5: 148.

[15] Hepplestone, S. P. and Srivastava, G. P. (2007). *J. Phys. Conf. Ser.* 92: 012076.

[16] Berendsen, H. J. C.; van der Spoel, D. and van Druen, R. (1995). GROMACS: A message-passing parallel molecular dynamics implementation. *Comp. Phys. Comm.* 91: 43-56

[17] Lindahl, E.; Hess, B. and van der Spoel, D. (2001). GROMACS 3.0: a package for molecular simulation and trajectory analysis. *J. Mol. Model* 7: 306-317.

[18] van der Spoel, D.; Lindahl, E.; Hess, B.; Groenhof, G.; Mark, A. E. and Berendsen, H. J. C. (2005). GROMACS: Fast, flexible, and free. *J. Comp. Chem.* 26: 1701-1718.

[19] Hess, B.; Kutzner, C.; van der Spoel, D. and Lindahl, E. (2008). J. Chem. Theory Comp. 4 435.

[20] Pronk, S.; Páll1, S.; Schulz, R.; Larsson, P.; Bjelkmar, P.; Apostolov, R.; Shirts, M. R.; Smith, J. C.; Kasson, P. M.; van der Spoel, D.; Hess, B. and Lindahl, E. (2013). GROMACS 4.5: a high-throughput and highly parallel open source molecular simulation toolkit. *Bioinformatics*

29: 845-854.

[21] Jorgensen, W. L.; Maxwell, D. S. and Tirado-Rives, J. (1996). Development and Testing of the OPLS All-Atom Force Field on Conformational Energetics and Properties of Organic Liquids. *J. Am. Chem. Soc.* 118: 11225-11236.

[22] Nosé, S. (1984). A molecular dynamics method for simulations in the canonical ensemble. *Mol. Phys.* 52: 255-268.

[23] Hoover, W. G. (1985). Canonical dynamics: Equilibrium phase-space distributions. *Phys. Rev. A* 31: 1695-1697.

[24] Yi, W.; Lu, L.; Dian-lin, Z.; Pan, Z. W. and Xie, S. S. (1999). Linear specific heat of carbon nanotubes. *Phys. Rev. B* 59: R9015- R9018.

[25] Hsu, I.-K.; Pettes, M. T.; Aykol, M.; Chang, C.-C.; Hung, W.-H.; Theiss, J.; Shi, L. and Cronin, S. B. (2011). Direct observation of heat dissipation in individual suspended carbon nanotubes using a two-laser technique. *J. App. Phys.* 110: 044328.

[26] Dobardžić, E.; Maultzsch, J.; Milošević, I.; Thomsen, C. and Damnjanović, M. (2003). The radial breathing mode frequency in double-walled carbon nanotubes: an analytical approximation. *Phys. Stat. Sol. (b)* 237: R7-R10.

[27] Lotfabad, E. M.; Kalisvaart, P.; Kohandehghan A, Cui K, Kupsta M, Farbod B and Mitlin D. (2014). Si nanotubes ALD coated with TiO_2, TiN or Al_2O_3 as high performance lithium ion battery anodes. *J. Mater. Chem. A* 2: 2504-2516.

[28] Nunzi, F. and Angelis, F. D. (2010). DFT Investigations of Formic Acid Adsorption on Single-Wall TiO2 Nanotubes: Effect of the Surface Curvature. *J. Phys. Chem. C* 115: 2179-2186.

CHAPTER 5

EFFECTS OF HYBRID INTERACTIONS ON THERMAL TRANSPORT PROPERTIES OF ORGANIC-INORGANIC PROVSKITES

The idea of composite structures via weak interactions, proposed in the previous chapter, does not always require tubular structures and seems to stand for general combinations. The suppression effects of the weak interactions are expected to function more effectively for materials with low thermal conductivities. The mass difference in components is also important for the selective control. The organic-inorganic composites might meet the above conditions. In this chapter, we adopt hybrid organic-inorganic halides of the formula ABX_3 (A = organic molecular cation; B = Ge, Sn, Pb; X = halide), which is one of the simplest organic-inorganic hybrid structures.

In addition to their well-known superior performance in photovoltaics [1-4], the hybrid organic-inorganic halides have recently attracted attention for possible thermoelectric applications [5]. The thermoelectric figure of merit (ZT) is expressed as $ZT = S^2\sigma T/\kappa$, where S is the Seebeck coefficient, T is the temperature, σ is the electronic conductivity, and κ is the thermal conductivity [6]. High carrier mobility, high Seebeck coefficient, and low thermal conductivity are desirable for efficient thermoelectric materials. Continuing efforts to understand the light conversion efficiency of ABX_3 revealed that their high carrier mobilities are based on small effective masses and long diffusion lengths [7-10]. Moreover, recent research shows that $CH_3NH_3PbI_3$ (hereafter MAPI) has a high Seebeck coefficient, deriving from multidegenerated conduction and valence bands [5].

Fortunately, MAPI is also characterized by a beneficial low thermal conductivity [11]. For both of the single-crystal and polycrystalline MAPI, thermal conductivities are observed as

$\sim 0.4\ \mathrm{Wm^{-1}K^{-1}}$ at room temperature, far below that of inorganic perovskites [12]. On the one hand, these results show that MAPI meets all the optimal requirements of materials for thermoelectric conversion; on the other hand, the cause of the drastic suppression of phonon transport remains obscure. The hybrid organic-inorganic halide perovskites have larger lattice parameters than fully inorganic ones and embedded cations move incoherently [13]. These conditions are similar to the existing phonon-glass electron-crystal materials, namely host-guest structures like type-I clathrate and skutterudite compounds [14-16]. In those systems, the rattling motions of the embedded atoms are coupled with the transverse acoustic mode and provide the phonon scattering [14]. For MAPI, it is also suggested that the ionic interactions couple inorganic lattice (Pb-I) vibrations with methylammonium (MA) motions. The IR and Raman spectra show that the Pb-I vibration density of states (vDOS) mainly overlaps with the rotation of MA [17-19], so rotational motion is thought to play a critical role in the suppression [11]. Even if this is the correct explanation, the specific mechanism remains unclear. In particular, the coupling mechanism between rotational motions and Pb-I vibrations, how it modifies the vibrational states, and the extent to which it suppresses the thermal conductivity are all issues that should be fully clarified. Such further understanding is mandatory not only to control the thermal transport properties of MAPI but also to provide guidelines for the design of hybrid thermoelectric materials.

In this study, we analyze the thermal transport properties of MAPI. The suppression effects induced by the MA rotation are evaluated and explained through the vibrational coupling analysis. To perform thermal conductivity calculations including anharmonic effects, we have developed an empirical potential for MAPI based on *ab initio* molecular dynamics calculations. By using this force field, the thermal conductivity of MAPI is calculated by using the RNEMD method, introduced in Sec. 2-3. The results are compared with model systems that include different

embedded cations, and it shows that the suppression of heat conduction is mainly attributed to the MA rotations. By checking the phonon band structures, we find that coupling between translational and rotational motions of MA is the key to the suppression mechanism in MAPI.

This chapter is organized as follows. In Sec. 5-1, the potential development procedures are explained. The thermal conductivities of MAPI and the related models are shown in Sec. 5-2. The detuning of parameters for the models with different embedded cations are also introduced. In Sec. 5-3, we discuss the suppression mechanism in low thermal transport properties of MAPI based on the phonon dispersion relations and vibrational couplings. Sec. 5-4 shows the summary of this chapter.

5-1. Potential development

FITTING PROCEDURES The molecular dynamics method is the best way to evaluate the thermal transport properties of materials with strong anharmonicity. Anharmonic potentials for thermal transport calculations can be developed via several approaches, in which the interatomic force constants (IFCs) are fitted to force trajectories of *ab initio* MD by linear regression [20, 21]. Such procedures are quite accurate for crystals where all atoms have rigid stable points for IFCs. However, in host-guest structures, embedded components feel complex and shallow potentials, which are a combination of non-bonded interactions with host atoms. Because the method using IFCs is not adequate for such structures, we have improved it by using interatomic potential functions. These functions include OPLS force fields used for the MWCNTs, and potential energies are attributed to the structural components (bonds, angles, and dihedrals) and the non-bonded interactions. The practical functional form is the following:

$$\begin{aligned} E_{\text{total}} &= E_{\text{bond}} + E_{\text{angle}} + E_{\text{dihedral}} + E_{\text{vdW}} + E_{\text{Coulomb}} \\ &= \sum_{\text{bond}} \alpha_i \left(r_i - r_{i,eq}\right)^2 + \sum_{\text{angle}} \beta_j \left(\theta_j - \theta_{j,eq}\right)^2 + \sum_{\text{dihedral}} \sum_{l=1}^{5} \gamma_{k,c} (\cos\phi_k)^c \\ &\quad + \sum_{l,m} \varepsilon_{lm} \left[\left(\frac{\sigma_{lm}}{r_{lm}}\right)^{12} - \left(\frac{\sigma_{lm}}{r_{lm}}\right)^{6} \right] + \sum_{l,m} \frac{1}{4\pi\epsilon_0} \frac{\mathcal{Z}_l \mathcal{Z}_m}{r_{lm}} \,. \end{aligned} \tag{5-1}$$

Most of terms are the same as Eq. (4-1). The dihedral contributions are described not as the OPLS type but as the Ryckaert-Bellemans function, only because of its convenience for fitting. In Eq. (5-1), $\alpha, \beta, \gamma, \varepsilon, \sigma,$ and $\mathcal{Z}$ represent the unknown parameters. The potential is a nonlinear function of $\varepsilon, \sigma,$ and $\mathcal{Z}$, and these parameters cannot be fitted with the linear regression methods. To overcome these issues, we use an empirical value for σ [22], and estimate $\mathcal{Z}$ from the *ab initio*

charge analysis [23]. Thus, the remaining unknown parameters are $\alpha, \beta, \gamma,$ and ε. In the fitting procedure, we first perform the *ab initio* MD and obtain the force trajectories, coordinate trajectories, $r_{i,eq}$, and $\theta_{j,eq}$. For every trajectory, we input all the known parameters in Eq. (S1) i.e., $r, r_{eq}, \theta, \theta_{eq}, \phi, \sigma,$ and $\mathcal{Z}$, fitting the remaining ones to the force trajectories by the linear regression analysis. The practical fitting procedure is shown as the flowchart in Figure 5-1.

The fitting procedure must be carefully selected. When we use the interatomic force constants as objective functions, the fitting parameters are isolated and the simple linear regression is adequate. Yet in interatomic potential functions, structural factors are correlated and such multicollinearity results in very high standard errors. Partial least squares regression is the most promising solution, because it removes the correlation in both of the dependent and independent variables by maximizing the covariance between latent dependent and latent independent variables [24].

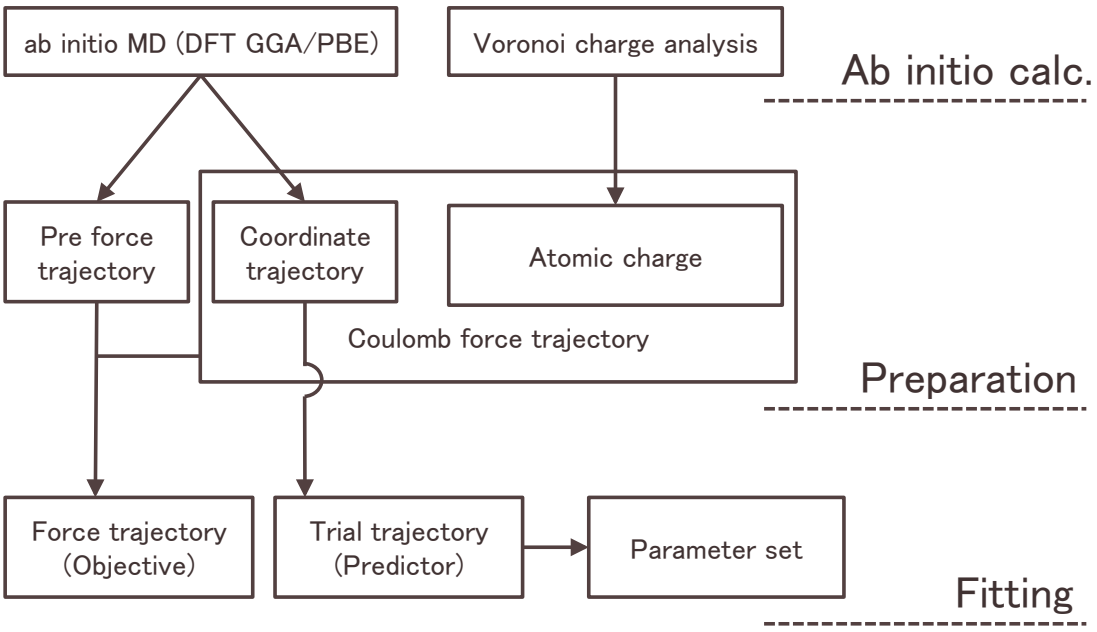

Fig. 5-1. Flowchart for the development of the empirical potential with interatomic potential functions.

MODIFICATIONS First, we test the validity of this interatomic potential fitted to *ab initio* MD results for the silicon crystal structure in the diamond cubic phase ($Fd\bar{3}m$). The force trajectories are calculated by using the density functional theory implemented in SIESTA, employing the Perdew-Burke-Ernzerhof exchange-correlation functional based on the generalized gradient approximation (GGA-PBE) [25], with the Troullier-Martins pseudopotentials. We adopt a $2 \times 2 \times 2$ supercell of the conventional Si unit cell $(Z = 8)$. The time step is set to 1.0 fs and the temperature is maintained at 300 K by means of the Nosé–Hoover thermostat. Assuming that non-bonded interactions are negligible compared with the bonded parts, i.e., that $\mathcal{Z}, \varepsilon = 0$, the parameters in the interatomic potential were fitted, through which we calculated the phonon dispersions. The frozen phonon method was applied to a $9 \times 9 \times 9$ supercell of the primitive unit cell $(Z = 2)$. The results are shown in Fig. 5-2 and compared with the experimental and *ab initio* results [20, 26]. The Eq. (5-1) potentials reproduced the experimental phonon dispersions in its own way, whose results are quite better than those of the conventional empirical force fields like the Keating valence force filed. However, the acoustic modes are still too steep and the energies around the Brillouin zone boundaries have some non-negligible errors, even for such simple crystal. The most direct way to improve the accuracy is expanding Eq. (5-1) into higher order. Accordingly, we have modified the potential function form as Eq. (5-2), where we have expanded the harmonic potential of each bond and angle to the 8th order, and several cross terms are introduced. The cross terms correspond to correlations between structural factors. For example, $\sum_{\text{angle}} \beta_j''(r_{j,1} - r_{j,1,eq})(r_{j,2} - r_{j,2,eq})$ indicates the coupling between the vibrations of two bonds in some angle component. We introduce four contributions as the cross terms: bond–angle couplings in angle components, bond–bond couplings in angle components, angle–angle couplings in dihedral components, and bond–bond–bond couplings in dihedral components.

$$
\begin{aligned}
E_{\text{total}} &= E_{\text{bond}} + E_{\text{angle}} + E_{\text{dihedral}} + E_{\text{vdW}} + E_{\text{Coulomb}} \\
&= \sum_{\text{bond}} \sum_{a=2}^{8} \alpha_{i,a}\left(r_i - r_{i,eq}\right)^a \\
&+ \sum_{\text{angle}} \left(\sum_{b=2}^{8} \beta_{j,b}\left(\theta_j - \theta_{j,eq}\right)^b + \beta_j'\left(r_{j,1} - r_{j,1,eq} + r_{j,2} - r_{j,2,eq}\right)\left(\theta_j - \theta_{j,eq}\right) \right. \\
&\left. + \beta_j''\left(r_{j,1} - r_{j,1,eq}\right)\left(r_{j,2} - r_{j,2,eq}\right) \right) \\
&+ \sum_{\text{dihedral}} \left(\sum_{c=1}^{5} \gamma_{k,c}(\cos\phi_k)^c + \gamma_k'\left(\theta_{k,1} - \theta_{k,1,eq}\right)\left(\theta_{k,2} - \theta_{k,2,eq}\right) \right. \\
&\left. + \gamma_k''\left(r_{k,1} - r_{k,1,eq}\right)\left(r_{k,2} - r_{k,2,eq}\right)\left(r_{k,3} - r_{k,3,eq}\right) \right) \\
&+ \sum_{l,m} \varepsilon_{lm} \left[\left(\frac{\sigma_{lm}}{r_{lm}}\right)^{12} - \left(\frac{\sigma_{lm}}{r_{lm}}\right)^{6} \right] + \sum_{l,m} \frac{1}{4\pi\epsilon_0} \frac{Z_l Z_m}{r_{lm}} \ .
\end{aligned}
\tag{5-2}
$$

We fit parameters bansed on Eq. (5-2), with which the phonon dispersion of the silicon crystal is calculated in the same manner as the above. The results are also shown in Fig. 5-2. Over a wide energy range, our results obtained via Eq. (5-2) potentially reproduce the experimental phonon dispersion well. The accuracy is almost the same as that of DFPT in lower energy region, yet at higher energy, some branches are only slightly underestimated. The comparison between the dispersions calculated with Eqs. (5-1) and (5-2) reveals the large contribution of the cross terms. However, when higher-order cross terms like $\sum_{\text{angle}} \beta_j'''\left(r_{j,1} - r_{j,1,eq}\right)^2\left(r_{j,2} - r_{j,2,eq}\right)^2$ are considered, they only marginally affect the vibrational energies and group velocities, meaning that Eq. (5-2) is necessary and sufficient.

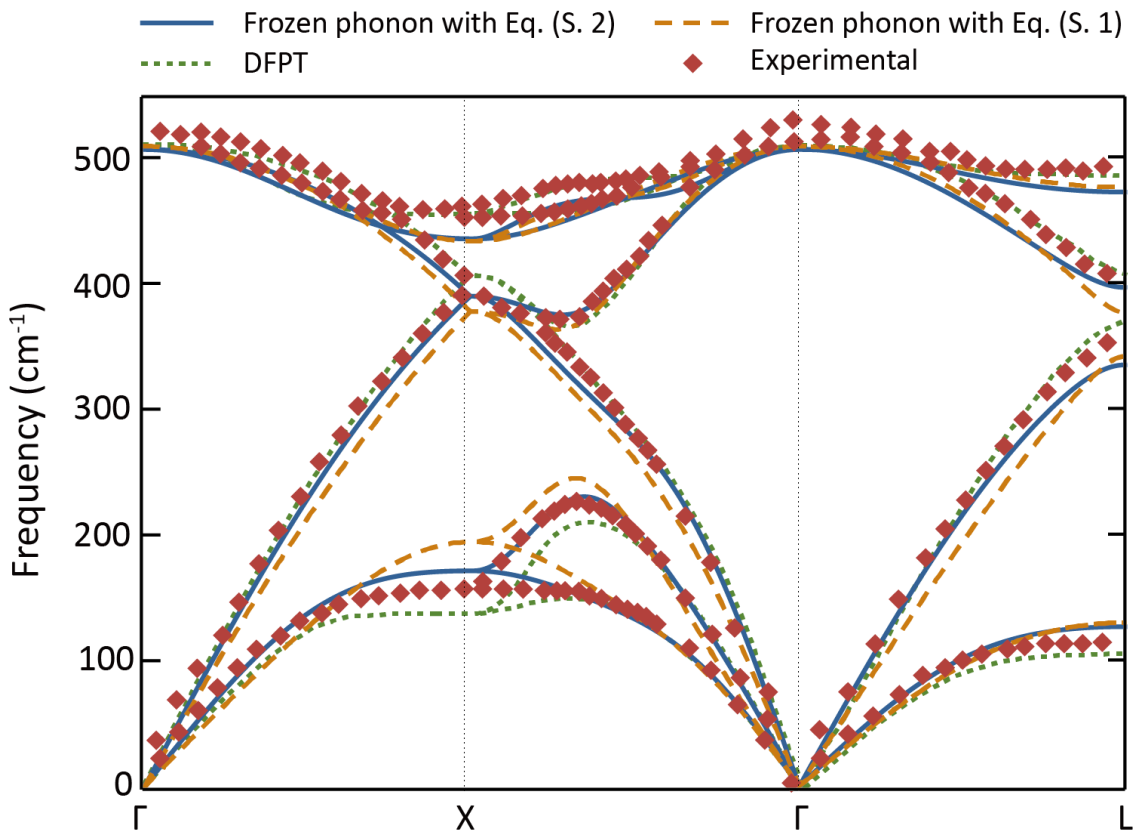

Fig. 5-2. Phonon dispersion relation of Si crystals evaluated with Eq. (5-1) (orange dashed line) and Eq. (5-2) (blue solid line). Experimental [26] (red diamonds) and DFPT [20] (green dotted line) results are also shown for comparison.

For further validation, the thermal conductivity of the silicon crystal is calculated. We employ the RNEMD method, which is performed for 5×10^6 steps with a 1.0 fs time step after thermalization for 10^5 steps. We used $3 \times 3 \times (150, 228, 300)$ supercells of the conventional unit cell and estimated the bulk thermal conductivity by the linear extrapolation method. The temperature dependence of thermal conductivities is shown in Fig. 5-3, together with the values previously reported in the literature [20, 27]; the agreement with both experimental and theoretical results is extremely encouraging with the results of NEMD calculations slightly underestimating the experimental ones. As previously reported, this underestimation is caused by the linear extrapolation for highly conductive materials and not by possible errors in the potential.

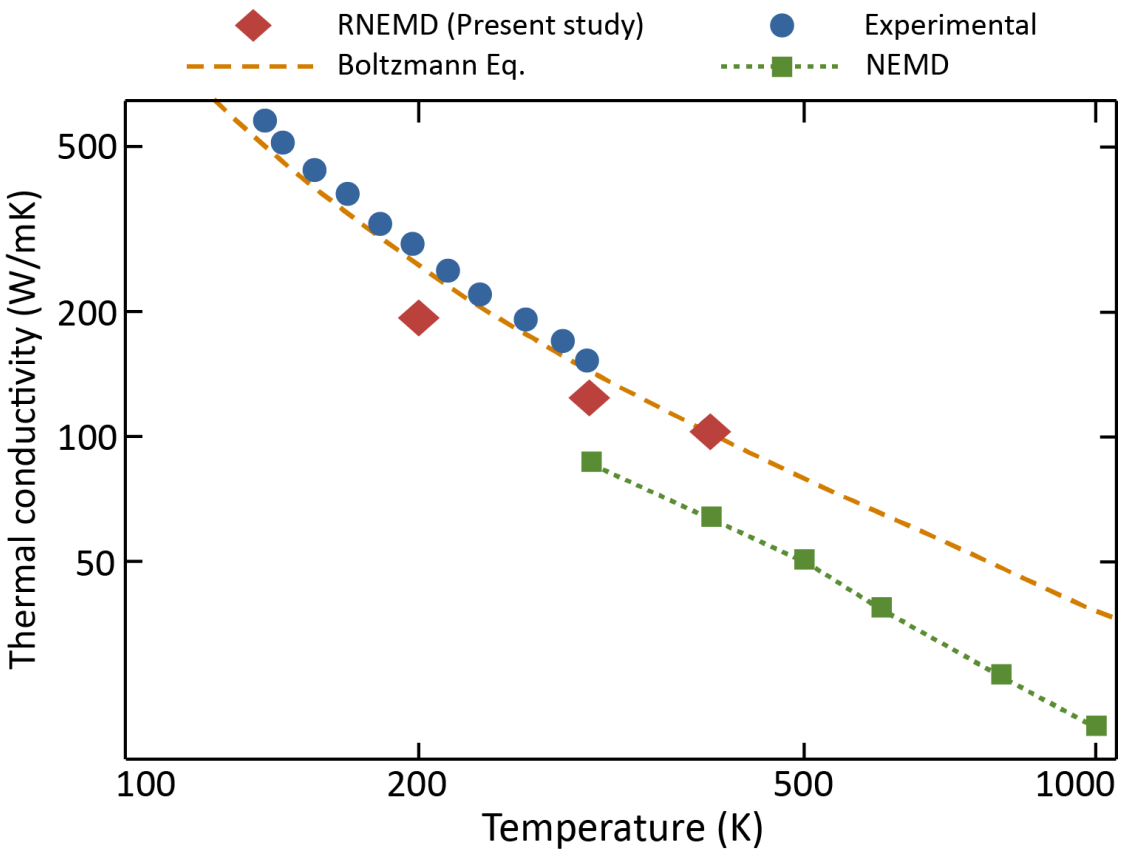

Fig. 5-3. Temperature dependence of the thermal conductivity of the silicon crystals evaluated with the RNEMD (red diamonds), Boltzmann equation [20] (orange dashed line), NEMD [20] (green squares), and in experiment [27] (blue filled circles).

HIBRID PEROVSKITES With Eq. (5-2), we develop the empirical potential of MAPI by fitting to the trajectories of *ab initio* MD. Similarly to the silicon crystal, the training set is based on the density functional theory with GGA functional, along with the Troullier-Martins pseudopotentials. Here we consider the tetragonal $(I4/mcm, Z = 4)$ unit cell of MAPI with 48 atoms (Fig. 5-4), using $3 \times 3 \times 2$ Monkhorst-Pack grids for k-point sampling. The time step is set to 0.5 fs and the temperature is maintained at 280 K by the Nosé–Hoover thermostat. In the fitting procedure, the results of the partial least squares regression are confirmed by 10-fold cross-validation. Note that, unlike the silicon crystal, non-bonded interactions are essential for ionic crystals including MAPI.

While the training data of GGA-PBE trajectories do not include the attractive vdW interactions, such attractive part is significantly smaller than the Coulomb interactions. We can expect that the fitting leads the intensity of the Lennard-Jones potential so as to reproduce the repulsive part mainly, which is very important in the empirical potential to compensate the excessive Coulomb interactions in the short-range deriving from the approximation of fixed atomic charges. Even though the attractive contribution of vdW interactions seems to be negligible, fitting with the empirical σ caused small errors to the long-range interactions, showing shrinking of the cages. We thus managed to expand σ by using the bare empirical vdW radii. The potential functions are fitted with such σ, whose high accuracy (95%) is estimated on the basis of the explained variance. The practical parameters are shown in Appendix. A.

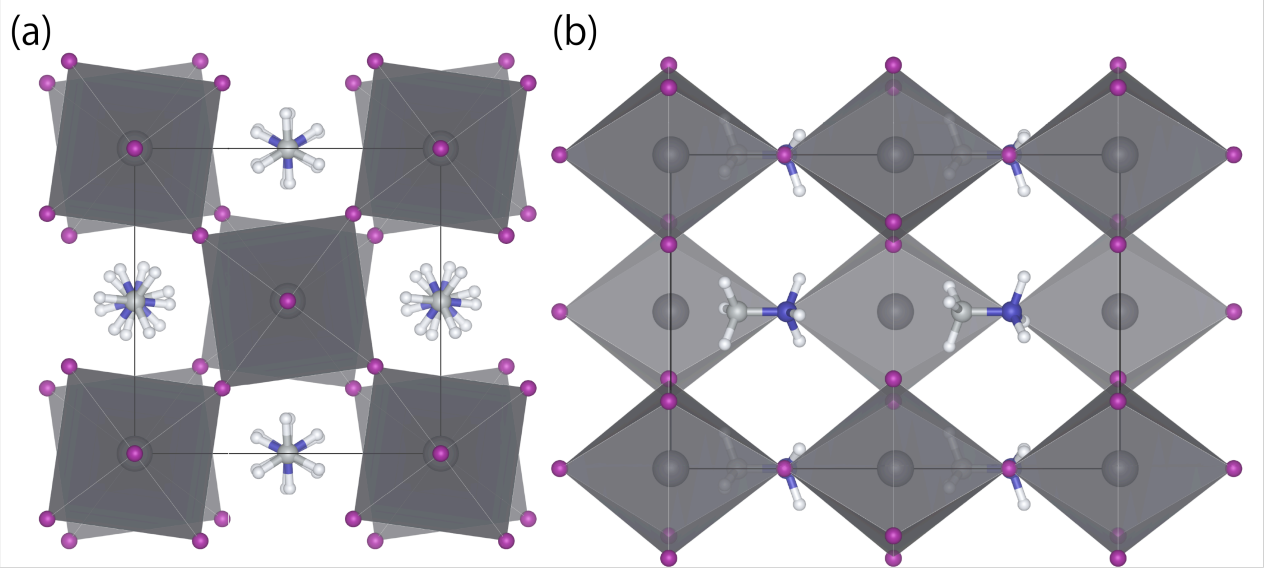

Fig. 5-4. (a) Lateral and (b) top view of the unit cell of MAPI in the tetragonal phase. (Gray: lead; purple: iodine; silver: carbon; blue: nitrogen; white: hydrogen atoms. Black solid line: unit cell)

5-2. Thermal transport properties

THERMAL CONDUCTIVITY With the developed potential, we evaluate the thermal conductivity of MAPI based on the RNEMD method. We calculate the size-dependent thermal conductivity by using $2 \times 2 \times (30, 60, 90)$ supercells of the tetragonal polymorph $(I4/mcm)$, the shortest model of which is shown in Fig. 5-5. First the atomic positions of the models are optimized, including the box shape and volume. Next, we thermalized the simulation box to the preset temperature with the *NVT* thermostat for 2×10^6 steps with a 0.5 fs time step. After removing the thermostat, we performed the RNEMD calculations for 10^7 steps with energy swapping each 1000 steps. The time steps in RNEMD are chosen based on the temperature difference convergence criterion. We check the change of the difference over time, whose results indicate that around 2.5 ns are required for conversion. Then 5 ns simulations are performed and we evaluate the mean temperature difference by averaging the difference after 2.5 ns.

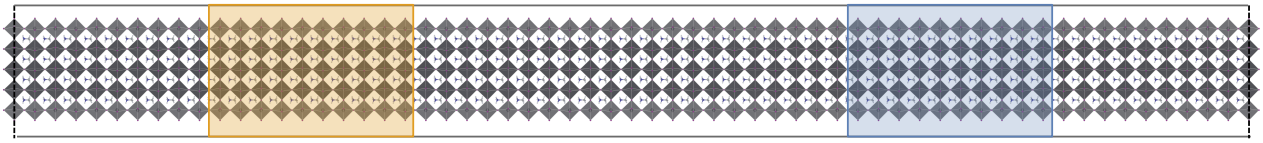

Fig. 5-5. $2 \times 2 \times 30$ supercell of the tetragonal MAPI. Hot and cool region in RNEMD are colored orange and blue, respectively.

The bulk thermal conductivity is evaluated by the linear extrapolation method. The bulk thermal conductivity is shown in Fig. 5-6, and its size dependency is also shown in the inset. We compared our results with previous experimental ones for MAPI [11] and with others for fully inorganic perovskite materials [12], observing very good agreement with the experimental thermal conductivity of MAPI single crystals; anyway these results are quite lower than those of fully inorganic perovskites over a wide temperature range.

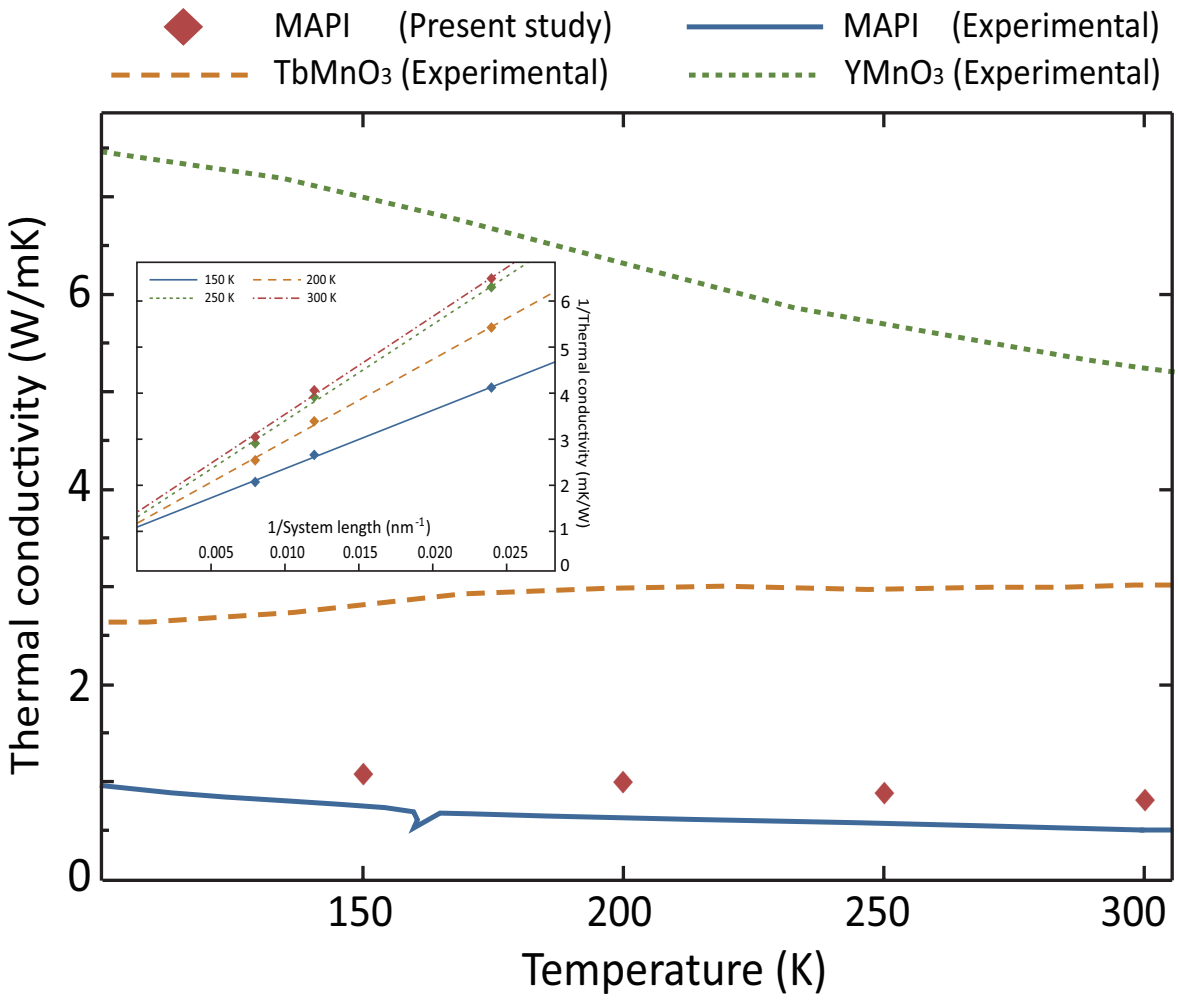

Fig. 5-6. Temperature dependence of the thermal conductivity of MAPI evaluated with RNEMD (red diamonds) and experimentally [11] (blue solid line). Experimental results of inorganic perovskites of $TbMNO_3$ (orange dashed line) and $YMnO_3$ (green dotted lines) fully inorganic perovskites [12]. The inset shows linear extrapolation to the bulk thermal conductivity of MAPI performed via thermal conductivities of finite systems.

DIFFERENT CATIONS The structural difference between MAPI and fully inorganic perovskites is represented by the A-site cation nature; thus, it is intuitive to ascribe the thermal conductivity suppression to the organic-inorganic interactions. To check whether motions of the MA cations are coupled with the inorganic host cages, we analyzed the thermal transport properties of the model structures shown in Fig. 5-7. In Model A, the embedded component is a diatomic molecule and the twisting degrees of freedom are truncated. Model B includes a single atom without rotational motions. Model C is the bare inorganic frame.

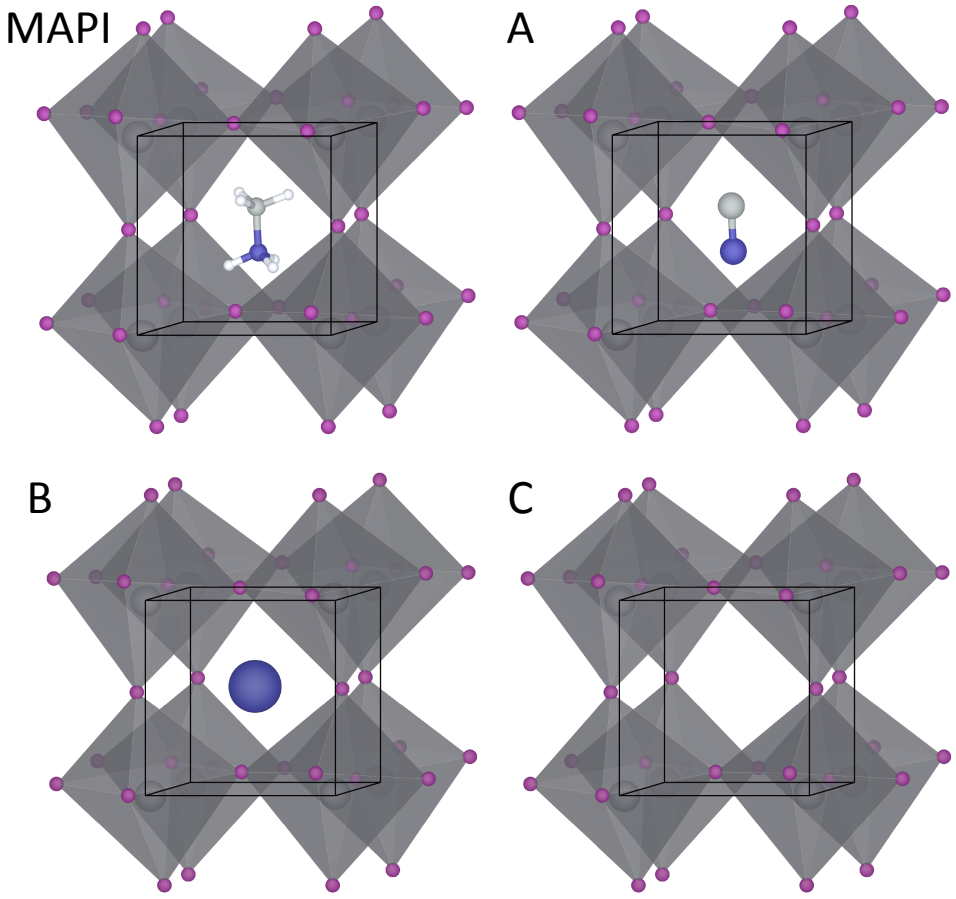

Fig. 5-7. Crystal structures of MAPI and of Models A, B, and C. Model A has a diatomic molecule, Model B has a single atom as embedded cation, while Model C is the bare inorganic frame.

In all the three systems, we modified atomic charges $(\mathcal{Z})$ to give a final neutral system and Lennard-Jones parameters (σ, ε) to maintain the volume of MAPI. In Model A, the atomic charges are neutralized in the functional groups, i.e. the charges of H atoms in -CH_3 (-NH_3) are summed in the C (N) atom. σ is the sum of the vdW radii and the bond length, e.g. $\sigma_{\mathrm{Pb-C}}$ is set as $\sigma_{\mathrm{Pb-C}} = \sqrt{2r_{\mathrm{vdW,Pb}} \times 2(r_{\mathrm{vdW,H}} + r_{\mathrm{C-H}})}$. The relaxed volume is thus calculated and ε is modified to keep the same volume of MAPI. In Model B, the atomic charge of the embedded atom is the sum of all charges of the atoms forming the methylammonium cation. $\sigma_{\mathrm{I-N}}$ is $\sigma_{\mathrm{I-N}} = \sqrt{2r_{\mathrm{vdW,I}} \times (2r_{\mathrm{vdW,H}} + r_{\mathrm{C-H}} + r_{\mathrm{C-N}} + r_{\mathrm{N-H}})}$. In Model C, we distributed the charges of the embedded molecules to I atoms. Such reduction may induce smaller anharmonic effects, but the subsequent overestimation of the thermal conductivity is expected to be rather small than the suppression effects caused by the embedded components. The related parameters are shown in Appendix. B.

The thermal conductivities are evaluated with the finite calculation model but not extrapolated to bulk values; they are reported for each model in Table 5-1, which shows that the thermal conductivity of Model C is larger than that of MAPI, but still low. Heavy atoms and weak bonds in the inorganic lattice thus contribute to the low thermal transport properties of MAPI. The results also show that the main difference is between Model A and Model B, meaning that the rotational motion of MA efficiently suppresses the thermal conductivity of the inorganic lattice.

Table. 5-1. Thermal conductivity of MAPI and of Models A, B, and C.

	MAPI	A	B	C
Degrees of freedom	twist+trans.+rot.	trans.+rot	trans.	none
Thermal conductivity (W/mK)	0.185	0.209	0.302	0.326

VIBRATIONAL DENSITY OF STATES For further understanding, we analyzed the vibrational properties of MAPI using MD simulations. Based on the Wiener–Khintchine theorem [28], the vDOS are evaluated as power spectra $P(\omega)$ of velocity autocorrelation functions. Velocities are mass weighted to normalize the intensity of spectra, so vDOS is expressed as:

$$P(\omega) = \frac{1}{2\pi}\int \frac{1}{N}\sum_{i=1}^{N} m_i \langle \boldsymbol{v}_i(\tau)\cdot \boldsymbol{v}_i(t+\tau)\rangle_\tau \, \mathrm{e}^{-i\omega t}\mathrm{d}t \,, \tag{5-1}$$

where ω is the angular momentum, N the number of atoms, m the atomic mass, $\boldsymbol{v}$ the velocity, τ the time, and t the time interval. To compare the vibration energies of organic and inorganic components, we calculate partial vDOS for two groups, Pb-I and MA. MAPI is thermalized at $150-250$ K at constant volume before the velocity sampling. Peak attributions are based on the normal modes of MAPI at the Γ point, viz., $\boldsymbol{q} = (0\ 0\ 0)$ where $\boldsymbol{q}$ is the phonon wave vector. The results are shown in Fig. 5-8 for two energy ranges, $400\text{-}3300\ \mathrm{cm}^{-1}$ and $0\text{-}400\ \mathrm{cm}^{-1}$, and their intensities are normalized by the highest peak in each energy region and each group. The vibration energies are consistent with spectroscopic results in previous studies [17-19, 29]. In the higher energy region, the main contribution to the spectra is associated only with the MA motions, and these peaks are attributed as bond stretching and angle deformation of MA cations. Increasing the temperature, the intensities of the peaks are reduced but their energies remain unaffected, meaning that these vibrations are not ideally harmonic, but that at the same time they do not couple with other vibrations via their anharmonic terms. Both Pb-I vibrations and MA motions are located in the lower energy region. The Pb-I spectra have two broad bands: a lower one located at $40\ \mathrm{cm}^{-1}$ with no energy shifts, and a higher band at $70\text{-}80\ \mathrm{cm}^{-1}$ that is clearly shifted to higher energy following a temperature increase, which is attributed to the longitudinal optic (LO) modes. MA components are also characterized by two bands: at $0\text{-}200\ \mathrm{cm}^{-1}$, we observe the band associated

with the translational and rotational motions. The highest peak in this band indicates the translations and shifts to higher energy as the temperature increases. The second band is delocalized at around $300\ \mathrm{cm}^{-1}$, which is attributed to the twisting motions and has no peak shift. The peak shifts with temperature mainly derive from the anharmonic contributions or from the thermal expansion of crystals [30]. Such results at constant volume suggest that anharmonic couplings occur between the translational motions of MA and LO modes of the Pb-I lattice, a feature that seems incompatible with the model analysis.

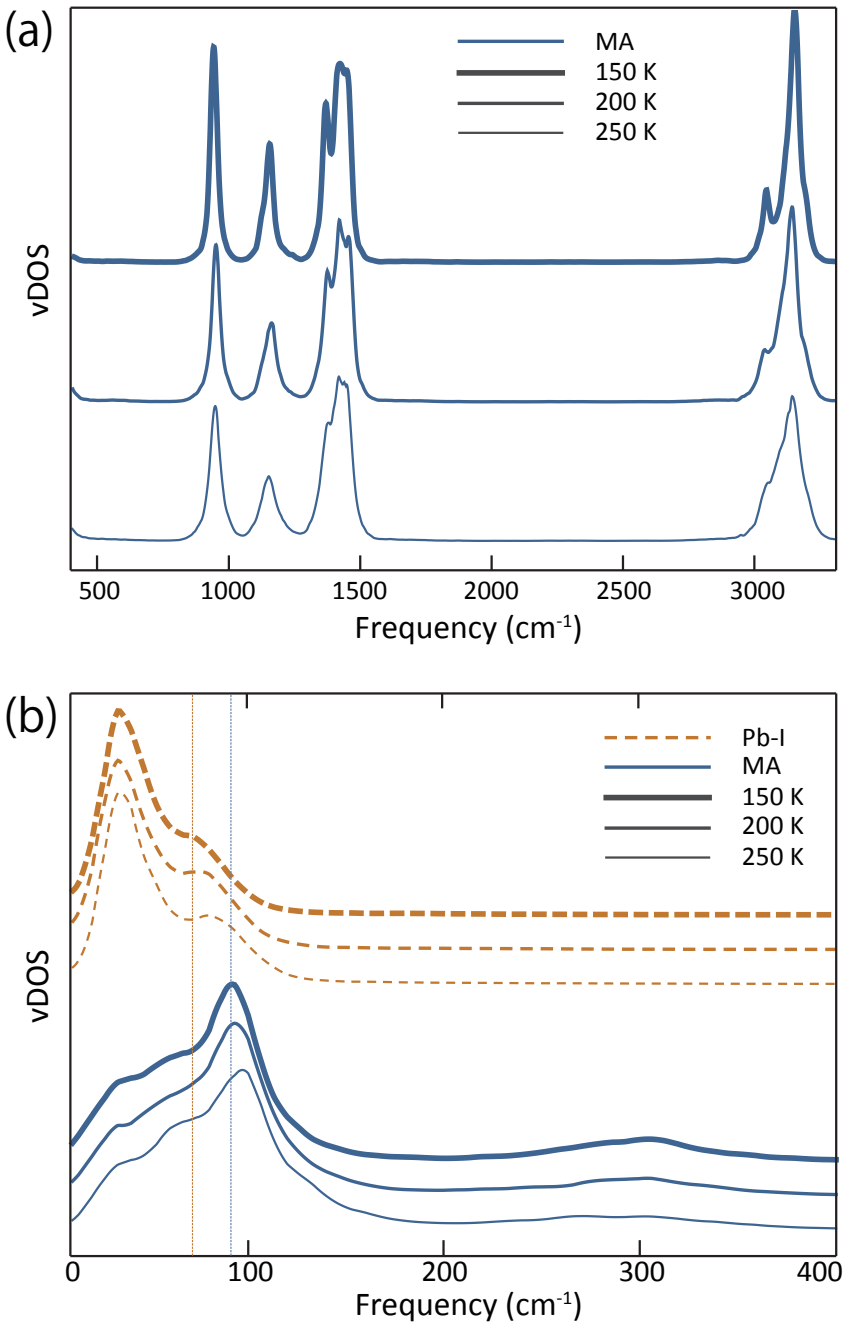

Fig. 5-8. Partial vibrational density of states of MAPI: MA (blue solid line) and Pb–I (orange dashed line) components. The energy range is divided into two regions: (a) 400 -3300 cm^{-1} and (b) 0-400 cm^{-1}. Their intensities are normalized considering the highest peak in each energy region and each group. Temperature is increased from 150 K (thickest line) to 250 K (thinnest line).

5-3. Suppression mechanism

The rotational motions suppress the thermal conductivity but the anharmonic couplings are mainly observed in the translations. A way to remedy this inconsistency stems from the phonon dispersion analysis. The phonon dispersions are directly measured from MD trajectories at 200 K, assuming an equipartition of vibrational energies [31]. We also impose the cubic crystal symmetry ($Pm\bar{3}m$) including a single MA cation in the unit cell, which allows us separate the intramolecular vibrations in the real space from the intermolecular interactions in the reciprocal lattice space. The results from Γ to X ($\boldsymbol{q} = (0\ 0\ 0)$ to $(0\ 0\ 0.5)$) are shown in Fig. 5-9. The partial phonon dispersions for Pb-I and MA are also evaluated from submatrices of the dynamical matrix. Fig. 5-9 also shows how phonon branches are classified based on their major contributions to vibrations. Thin lines correspond to Pb-I-dominant vibrations, and we observe that the Pb-I branches in the MAPI dispersion are almost the same as those of the Pb-I partial dispersion. These results are consistent with the fact that when two vibration systems with different mass are coupled, vibrational energies of the heavy system result almost unaffected. In the MA partial dispersion, the blue lines indicate the translational motions and the orange lines are the rotations. At the Γ point, these motions are distinct and symmetric; the N and C atoms have parallel vibrational vectors of the same length. When the energy increases along the wave vector and passes over the region A in Fig. 5-9, some of these vibrations appear to be asymmetric (green lines). This means that the translational and rotational motions are mixed and branch off into two asymmetric modes, N-atom dominant and C-atom dominant motions. This coupling corresponds to the deviation of molecular motions from the crystal symmetry, which may come from long-range interactions or weak ordering between molecular dipoles. In MAPI, the transverse optic (TO) modes of Pb-I are mainly coupled with the rotational motions of MA. There is a small energy difference between such coupled modes and only

limited energy shifts occur in MA branches. On the other hand, by comparing MAPI with MA, we can see that the translational branches are strongly shifted to higher energy because of the coupling with LO modes. These coupled modes are also described by the vDOS analysis. Similarly, also in MAPI, translational and rotational branches are mixed into asymmetric vibrations in almost the same wave vector region. Moreover, the strong energy shift results in a crossover between MA branches located in region B. This crossing becomes clear in the phonon dispersion, where the dynamical matrix is projected onto the normal modes at the Γ point (Fig. 5-9), revealing that the energy gap between the two phonon branches of MA in region B corresponds to an avoided crossing, where the translational motions switch to the rotations, and *vice versa*. Such mixing and crossing result in the coupling between LO and TO modes mediated by the interactions between the translational and rotational motions, respectively. The suppression effects of MA rotations and the anharmonic energy shift in the 70-80 cm^{-1} region suggest that these couplings limit the thermal conductivity of MAPI. That is, rotations do not directly scatter phonons, but the quite low thermal conductivity of MAPI is attributed to the interaction between LO and TO modes via the mixed/crossed translational and rotational motions of MA.

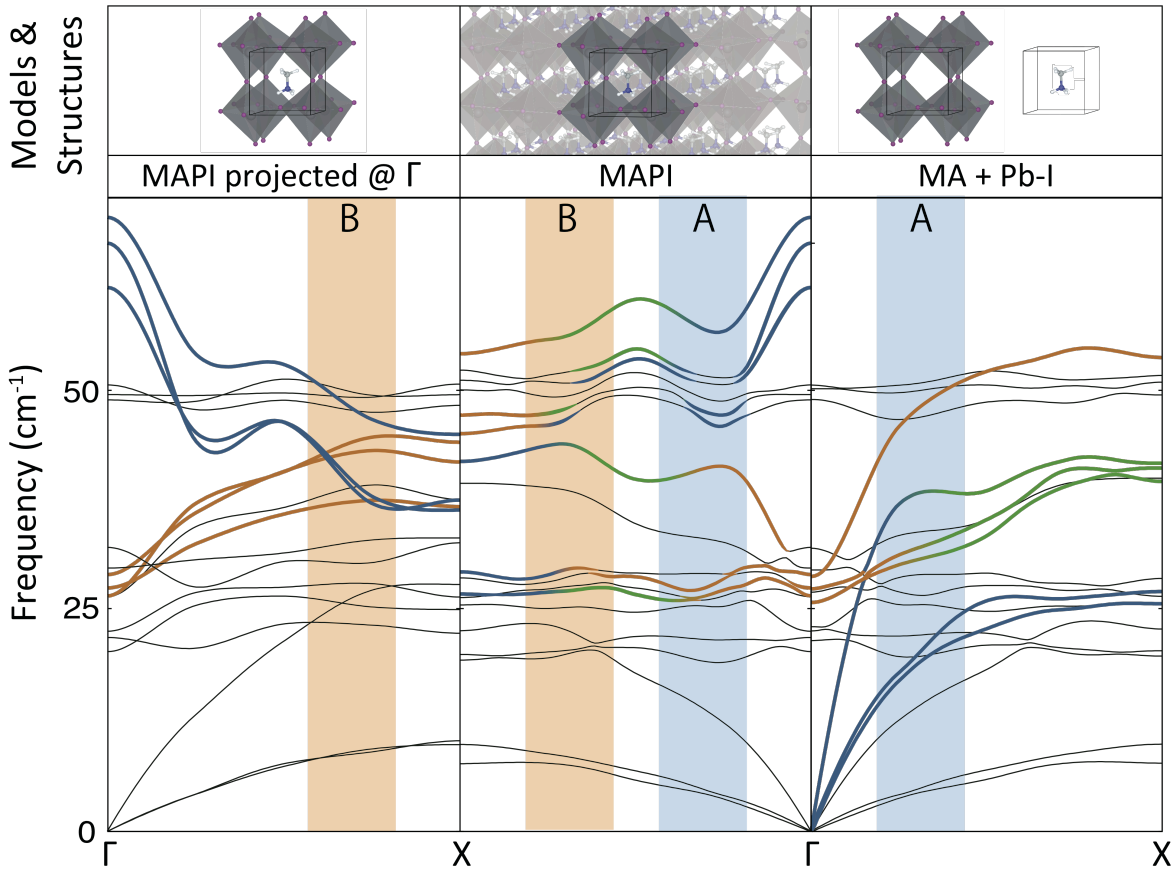

Fig. 5-9. Phonon dispersion relation of MAPI in the cubic phase (center) with partial components of Pb-I and MA (right) and their projection onto the normal modes at the Γ point (left). We classify the phonon branches based on their major contributions to vibrations: Pb-I (black thin line), MA translational (blue thick line), rotational (orange thick line), and mixed motions (green thick line). The mixing and crossing among MA branches are observed in the wave vector regions A and B, respectively.

5-4. Summary

We have presented the mechanism of the low thermal transport properties of MAPI. After developing an empirical potential of MAPI based on *ab initio* MD and analyzing its thermal conductivities with RNEMD methods, we compared the results with those from model systems that include different embedded cations. We found that the suppression of thermal conductivity mainly derives from the rotational motions of MA cations. The vDOS analysis showed that the vibrational energy shifts as the temperature increases, where anharmonic couplings occur. From the analysis of the phonon band structures, coupled translational and rotational motions of MA are found to interact with the Pb–I cages and build couplings between the isolated lattice vibrations, which suppress the phonon transport in MAPI.

The hybrid halide materials are known to have design possibility in wide compositional region. Now it is promising that the thermal conductivity of the hybrid organic-inorganic halides can be tailored based on the embedded molecules and their interaction between the inorganic lattices. The simplest way is deuterateing the MA cations, which slow the rotational motions and moderate the suppression effects, as shown in Table 5-2. The results shows that heavier the mass of the embedded component, higher the thermal conductivity. Moreover, the difference between the CD_3ND_3 and CH_3NT_3 also shows that the mass asymmetry has reduced effect on the suppression. The atom substitution is also intuitive way to control the organic-inorganic interactions, which is considered in the next chapter.

Table. 5-2. Thermal conductivity of $CD_3ND_3PbI_3$, $CT_3NT_3PbI_3$, and $CH_3NT_3PbI_3$.

	MAPI	$CD_3ND_3PbI_3$,	$CT_3NT_3PbI_3$	$CH_3NT_3PbI_3$
Embedded Molecular weight	32.1	38.1	44.1	38.1
Thermal conductivity (W/mK)	0.185	0.212	0.232	0.215

Appendix. A

Parameters in the developed potential for MAPI in the format of Eq. (5-2).

Bonds	Stable length (Angstrom)	Order 1	2	3	4	5	6	7	8
Pb-I	3.3500	0.0000	0.8046	−4.1355	−5.0679	22.897	193.73	341.76	180.48
C-H	1.1091	0.0000	32.855	−81.109	69.171	−4.9147	6.8536	333.52	−3082.2
N-H	1.0477	0.0000	34.192	−19.026	−983.86	595.08	166.33	-1.92×10^{5}	1.48×10^{6}
C-N	1.4884	0.0000	24.655	−118.16	32.514	312.11	590.76	−592.19	750.31

Angles	Stable angles (degree)	Order 1	2	3	4	5	6	7	8	Cross term bond-angle	bond-bond
I-Pb-I	90.000	0.0000	0.6464	−0.6804	1.5270	−1.3678	−0.9770	11.976	11.513	0.1694	−0.0275
Pb-I-Pb	180.00	0.0000	0.8772	21.822	158.91	508.766	788.30	580.84	165.35	−0.046	0.6943
N-C-H	108.85	0.0000	5.1269	−3.5359	1.0148	139.718	−210.77	−568.65	2297.9	1.4023	0.5808
H-C-H	110.08	0.0000	2.9532	−4.3932	3.2119	173.649	−37.827	−599.84	1320.2	0.8876	0.0159
C-N-H	110.93	0.0000	3.6410	1.2086	−12.096	−271.91	1031.3	−1196.0	568.52	0.7241	1.3283
H-N-H	107.97	0.0000	2.7614	−7.4678	−5.1374	455.802	247.58	−2644.9	4817.6	0.3739	0.7356

Dihedrals	Order 1	2	3	4	5	Cross term bond-bond-bond	angle-angle
H-C-N-H	−0.3521	0.0724	0.1577	−0.1063	−0.1045	−17.251	0.0135
Pb-I-Pb-I	0.0011	−0.0009	0.0034	0.001	−0.0022	0.136	0.0000

Long-range pairs	1 − 2	1 − 3	1 − 4
Weight	0.0000	0.5000	1.0000

Lennard-Jones		sigma	epsilon
Pb	H (−CH3)	4.4537	0.0046
I	C	4.1719	0.0111
I	N	3.9869	0.0210

Charges	
Pb	0.3690
I	−0.1910
C	0.0310
N	0.0050
H (−CH3)	−0.0180
H (−NH3)	0.0740

Appendix. B

Parameters modified from MAPI for Model. A, B, and C in the format of Eq. (5-2).

Model A:

	Lennard-Jones	sigma	epsilon
Pb	C	5.5648	0.0037
I	N	5.0659	0.0070

	Charges
Pb	0.3690
I	−0.1910
C	−0.0230
N	0.2270

Model B:

	Lennard-Jones	sigma	epsilon
Pb	N	5.7783	0.0021

	Charges
Pb	0.3690
I	−0.1910
N	0.2040

Model C:

	Charges
Pb	0.3690
I	−0.1230

Bibliography

[1] Kojima, A.; Teshima, K.; Shirai, Y. and Miyasaka, T. (2009). Organometal Halide Perovskites as Visible-Light Sensitizers for Photovoltaic Cells. *J. Am. Chem. Soc.* 131: 6050– 6051.

[2] Kim, H.-S.; Lee, C.-R.; Im, J.-H.; Lee, K.-B.; Moehl, T.; Marchioro, A.; Moon, S.-J.; Humphry-Baker, R.; Yum, J.-H.; Moser, J. E.; Grätzel, M. and Parkb, N.-G. (2012). Lead Iodide Perovskite Sensitized All-Solid-State Submicron Thin Film Mesoscopic Solar Cell with Efficiency Exceeding 9%. *Sci. Rep.* 2: 591.

[3] Zhou, H.; Chen, Q.; Li, G.; Luo, S.; Song, T.; Duan, H.-S.; Hong, Z.; You, J.; Liu, Y. and Yang, Y. (2014). Interface engineering of highly efficient perovskite solar cells. *Science* 345: 542-546.

[4] Jeon, N. J.; Noh, J. H.; Yang, W. S.; Kim, Y. C.; Ryu, S.; Seo, J. and Seok, S. I. (2015). Compositional engineering of perovskite materials for high-performance solar cells. *Nature* 517: 476-480.

[5] He, Y. and Galli, G. (2014). Perovskites for Solar Thermoelectric Applications: A First Principle Study of $CH_3NH_3AI_3$ (A = Pb and Sn). *Chem. Mater.* 26, 5394-5400.

[6] Rowe, D. M. (2006). General Principles and Basic Condiderations. *Thermoelectrics Handbook: Macro to Nano*, ch. 1. CRC Press. ISBN 0849322642.

[7] Giorgi, G.; Fujisawa, J.-I.; Segawa, H. and Yamashita, K. (2013). Small Photocarrier Effective Masses Featuring Ambipolar Transport in Methylammonium Lead Iodide Perovskite: A Density Functional Analysis. *J. Phys. Chem. Lett.* 4: 4213-4216.

[8] Xing, G.; Mathews, N.; Sun, S.; Lim, S. S.; Lam, Y. M.; Grätzel, M.; Mhaisalkar, S. and Sum, T. C. (2013). Long-Range Balanced Electron- and Hole-Transport Lengths in Organic-Inorganic $CH_3NH_3PbI_3$. *Science* 342: 344-347.

[9] Brivio, F.; Butler, K. T. and Walsh, A. (2014). Relativistic quasiparticle self-consistent electronic structure of hybrid halide perovskite photovoltaic absorbers. *Phys. Rev. B* 89: 155204.

[10] Kawai, H.; Giorgi, G.; Marini, A. and Yamashita, K. (2015). The Mechanism of Slow Hot-Hole Cooling in Lead-Iodide Perovskite: First-Principles Calculation on Carrier Lifetime from Electron-Phonon Interaction. *Nano Lett.* 15: 3103-3108.

[11] Pisoni, A.; Jaćimović, J.; Barišić, O. S.; Spina, M.; Gaál, R.; Forró, L. and Horváth, E. (2014). Ultra-Low Thermal Conductivity in Organic–Inorganic Hybrid Perovskite $CH_3NH_3PbI_3$. *J. Phys. Chem. Lett.* 5: 2488-2492.

[12] Zhou, J.-S. and Goodenough, J. B. (2006). Unusual Evolution of the Magnetic Interactions versus Structural Distortions in $R\mathrm{MnO}_3$ Perovskites. *Phys. Rev. Lett.* 96: 247202.

[13] Leguy, A. M. A.; Frost, J. M.; McMahon, A. P.; Sakai, V. G.; Kockelmann, W.; Law, C.H.; Li, X.; Foglia, F.; Walsh, A.; O'Regan, B. C.; Nelson, J.; Cabral, J. T. and Barnes, P. R. F. (2014). The dynamics of methylammonium ions in hybrid organic–inorganic perovskite solar cells. *Nat. Commun.* 6: 7124.

[14] Takabatake, T. and Suekuni, K. (2014). Phonon-glass electron-crystal thermoelectric clathrates: Experiments and theory. *Rev. Mod. Phys.* 86: 669-716.

[15] Nolas, G. S.; Cohn, J. L.; Slack, G. A. and Schujman, S. B. (1998). Semiconducting Ge clathrates: Promising candidates for thermoelectric applications. *Appl. Phys. Lett.* 73: 178-180.

[16] Nolas, G. S.; Morelli, D. T. and Teritt, T. M. (1999). SKUTTERUDITES: A Phonon-Glass-Electron Crystal Approach to Advanced Thermoelectric Energy Conversion Applications. *Annu. Rev. Mater. Sci.* 29: 89-116.

[17] Quarti, C.; Grancini, G.; Mosconi, E.; Bruno, P.; Ball, J. M.; Lee, M. M.; Snaith, H. J.;

Petrozza, A. and Angelis, F. D. (2014). The Raman Spectrum of the $CH_3NH_3PbI_3$ Hybrid Perovskite: Interplay of Theory and Experiment. *J. Phys. Chem. Lett.* 5: 279-284.

[18] Quarti, C.; Mosconi, E. and Angelis, F. D. (2015). Structural and electronic properties of organo-halide hybrid perovskites from ab initio molecular dynamics. *Phys. Chem. Chem. Phys.* 17: 9394-9406.

[19] Brivio, F.; Frost, J. M.; Skelton, J. M.; Jackson, A. J.; Weber, O. J.; Weller, M. T.; Gonñi, A. R.; Leguy, A. M. A.; Barnes, P. R. F. and Walsh, A. (2015). Lattice dynamics and vibrational spectra of the orthorhombic, tetragonal, and cubic phases of methylammonium lead iodide. *Phys. Rev. B* 92: 144308.

[20] Tadano, T.; Gohda, Y. and Tsuneyuki, S. (2014). Anharmonic force constants extracted from first-principles molecular dynamics: applications to heat transfer simulations. *J. Phys.: Condens. Matter* 26: 225402.

[21] Zhou, F. (2014). Lattice Anharmonicity and Thermal Conductivity from Compressive Sensing of First-Principles Calculations. *Phys. Rev. Lett.* 113: 185501.

[22] Batsanov, S. S. (2001). Van der Waals Radii of Elements. *Inorg. Mater.* 37: 871-885.

[23] Fonseca Guerra, C.; Handgraaf, J.-W.; Baerends, E. J. and Bickelhaupt. F. M. (2004). Voronoi Deformation Density (VDD) Charges: Assessment of the Mulliken, Bader, Hirshfeld, Weinhold, and VDD Methods for Charge Analysis. *J. Comput. Chem.* 25: 189-210.

[24] Mevik, B.-H. and Wehrens, R. (2007). The pls Package: Principal Component and Partial Least Squares Regression in R. *J. Stat. Soft.* 18: 2.

[25] Perdew, J. P.; Burke, K. and Ernzerhof, M. (1996). Generalized Gradient Approximation Made Simple. *Phys. Rev. Lett.* 77: 3865−3868.

[26] Kremer, R. K.; Graf, K.; Cardona, M.; Devyatykh, G. G.; Gusev, A. V.; Gibin, A. M.;

Inyushkin, A. V.; Taldenkov, A. N. and Pohl, H.-J. (2004). Thermal conductivity of isotopically enriched 28Si: revisited. *Solid State Commun.* 131: 499-503.

[27] Nilsson, G. and Nelin, G. (1972). Study of the Homology between Silicon and Germanium by Thermal-Neutron Spectrometry. *Phys. Rev. B* 6: 3777-3786.

[28] Thomas, M.; Brehm, M.; Fligg, R.; Vöhringer, P. and Kirchner, B. (2013). Computing vibrational spectra from *ab initio* molecular dynamics. *Phys. Chem. Chem. Phys.* 15: 6608-6622.

[29] Mattoni, A.; Filippetti, A.; Saba, M. I.; Caddeo, C. and Delugas, P. (2016). Temperature Evolution of Methylammonium Trihalide Vibrations at the Atomic Scale. *J. Phys. Chem. Lett.* 7: 529-535.

[30] Postmus, C.; Ferraro, J. R. and Mitra, S. S. (1986). Pressure Dependence of Infrared Eigenfrequencies of KCl and KBr. *Phys. Rev.* 174: 983-987.

[31] Kong, L. T. (2011). Phonon dispersion measured directly from molecular dynamics simulations. *Comput. Phys. Commun.* 182: 2201−2207.

CHAPTER 6

EFFECTS OF HALIDE SUBSTITUTIONS ON THERMAL TRANSPORT PROPERTIES OF ORGANIC-INORGANIC PROVSKITES

In the hybrid perovskites, small organic cations are embedded in inorganic cages, which provides both of easy processing methods like organic materials and comparable properties to inorganic candidates as optoelectronic, thermoelectric, or piezoelectric materials [1, 2]. Successive researching is performed about MAPI, showing that the excellent optoelectronic properties are attributed to their appropriate band gaps [3, 4], low exciton binding energies [5], and higher carrier mobilities based on small effective masses and long diffusion lengths. At the same time, the heat insulating properties of MAPI result from their soft and heavy inorganic lattice and vibrational couplings.

While such understanding of MAPI is getting deeper and deeper, the other exploring directions become more important to be considered, namely, the other organic-inorganic perovskite structures, as introduced in the summary of the previous chapter. It is known that perovskite structures have prominent design possibility in wide compositional region often described by the empirical Goldschmidt tolerance factor. This scheme is recently expanded to hybrid structures [6, 7], which showed that over 700 compounds can be made, promising enormous degrees of freedom for material design. In such range of material exploring, the most familier candidates are mono-substitutions; for example, formamidinium lead iodide or methylammonium lead bromide ($CH_3NH_3PbBr_3$: MAPBr). These simple substitutions are expected to stabilize hybrid structures [8] or improve the electronic properties [9-11], which are demonstrated in several experimental researches. In particular, their electronic properties are also analyzed in theoretical works mainly

based on the static first-principles calculations, showing modified band structures [12] and electron-phonon couplings [13].

On the other hand, dynamical properties in such substituted structures remain unclear especially at finite temperature. While sampling meta-stable structures have shown sound vibrational properties [14], stability of structures, phase transitions, vibrational and thermal properties are still difficult to be analyzed only with the first-principles calculations, indicating the definite importance of analysis based on molecular dynamics with empirical force fields. Fortunately, potential functions of MAPI are already developed in several researches as the pervious chapter. In order to expand the region of material exploring, the most direct and promising way is to extend these force fields to others in family of compounds and enhance their database.

The methodology developed in Chapter 5 is automatic and straightforward with high accuracy, but developed potential is often specific and limited to target materials, which may spoil the universality and transferability of database. So we adopt the simple potential functions for MAPI proposed by Alessandro M. *et al.* [15], and tune the parameters into other hybrid perovskites. Even we can begin with the MAPI potential, tuning all parameters is still too inconvenient to apply to large variety of perovskites. Now some simpler procedure for parametrization is required, accordingly in this research, we establish an appropriate guideline for reparametrization and extending data, holding MAPBr up as an example. Our procedure consists of step-by-step and physically-sound detuning of parameters with introducing several scalling factors, intended to reproduce typical results of DFT calculations and experiments including phase transitions. Developed potential for MAPBr is validated by classical analysis of the above reference properties, and its accuracy is assessed by compassion between one with MAPI force fields. Moreover we apply our force fields to the analysis of cation reorientation and vibrational density of states.

Comparing with previous MAPI results, we investigate the effects of the halide mono-substitution, focusing on the thermal transport properties.

This chapter is organized as follows. In Sec. 6-1, the potential function is introduced. The tuning procedures for MAPBr are also explained. The validations of the developed potential are performed in Sec. 6-2, in terms of the static energy properties. Atomic charges, cohesive energy and energy barriers for cation rotations are investigated. Sec. 6-3 confirms that our potential sufficiently reproduces the phase transition properties of MAPBr, observed in experiment. In Sec. 6-4, we discuss the vibrational properties and effects of halide substitution to them. The expected effects to the thermal conductivity are also investigated. Concluding rematks of this chapter are given in Sec. 6-5.

6-1. Potential development

Here we adopt the classical MYP interatomic model, where total energy is described by the sum of organic-organic, U_{OO}, organic-inorganic, U_{OI}, and inorganic-inorganic interactions, U_{II}. U_{OO} is based on the AMBER functional forms and follows the standard GAFF parametrization [16, 17]; U_{II} consists of the Buckingham potential with electrostatic interactions. U_{OI} is described as the sum of three terms, namely, the Buckingham potentials for (Pb,I)-(C,N) interactions, Lennard-Jones for (Pb,I)-(H), and electrostatic terms, as following:

$$U_{\mathrm{OI}} = \sum_{i,j}\left[A_{ij}e^{-r_{ij}/\rho_{ij}} - \frac{\sigma_{ij}}{r_{ij}^{6}}\right] + \sum_{i,j}\left[\frac{1}{4\pi\varepsilon_0}\frac{Z_i Z_j}{r_{ij}}\right] + \sum_{i,j}\epsilon_{ij}\left[\left(\frac{s_{ij}}{r_{ij}}\right)^{12} - \left(\frac{s_{ij}}{r_{ij}}\right)^{6}\right], \tag{6-1}$$

where A, ρ, and σ are the parameters of Buckingham potential, ε_0 the dielectric constant, Z the partial atomic charge, ϵ and s the parameters of Lennard-Jones potential, and r the distance. In the previous research, the parameters of MAPI are obtained by fitting on a data set based on the first principles calculations with the density functional theory (DFT). There are 46 parameters, and here we detune them to newly develop the potential of MAPBr. The practical procedure consists of the following three steps. Note that, in this procedure, we basically follow the concept of the MAPI model potential, viz., placing much importance to manage both of quantitative accuracy and simplicity of the model.

(i) We begin with reproducing the experimental lattice constant and DFT cohesive energy curve of the cubic MAPBr. In the MYP scheme, the stable lattice constant mainly depends on the Buckingham potential in U_{II}, while it is also affected by the electrostatic interactions moderately and the Buckingham part in U_{OI} slightly. Then we scales Buckingham parameters in U_{II} and atomic charges by introducing two scaling factors, viz., α for the former and β for the latter:

$$A_{\mathrm{II}} = \alpha A'_{\mathrm{II}}, \quad \rho_{\mathrm{II}} = \frac{1}{\alpha}\rho'_{\mathrm{II}}, \quad \sigma_{\mathrm{II}} = \frac{1}{\alpha}\sigma'_{\mathrm{II}}, \quad Z = \beta Z'. \tag{6-2}$$

Here $\alpha > 1$ and $\beta > 1$ affect on lattice shrinking. We can tune the lattice parameters only with α or β, but it requires too strong modifications, so in practice, we modified both parameters with considering the ratio between the atomic charges of MAPBr and MAPI obtained with *ab initio* charge analysis.

(ii) Then we evaluate the rotational barriers, defined mainly with U_{OI}. Now new scaling factor is introduced for the interactions between bromide atoms and cations, Br-(N, C), and ones for lead remain unchanged;

$$A_{\mathrm{OI}} = \frac{1}{\gamma}A'_{\mathrm{OI}}, \quad \rho_{\mathrm{OI}} = \frac{1}{\gamma}\rho'_{\mathrm{OI}}, \quad \epsilon_{\mathrm{OI}} = \frac{1}{\gamma}\epsilon'_{\mathrm{OI}}, \quad s_{\mathrm{OI}} = \frac{1}{\gamma}s'_{\mathrm{OI}}. \tag{6-3}$$

$\gamma > 1$ also results in short inorganic-organic interactions, yet unlike Eq. (6-2), the scaling factors on intensities are also inverse. Such scaling results in moderate modifications than the direct scaling, with which we expect to reduce the rotational barriers with suppressing effects to other properties, in this case, the lattice constant and cohesive energy curve. In this step, we mainly tunes γ, but also α to keep the experimental lattice constants.

(iii) Calculations with the current force field bring higher phase transition temperature, even though it reproduces the above static properties. It means that the energy barriers for rotations of cations and deformations of lattice are thermodynamically overestimated, and further refinements are required as similar as the case of MAPI. In MAPI parametrization, the definitive parameter for this modification is the length parameter in I-N interactions, and weaker interactions result in lower phase transition temperature. While the organic-inorganic interactions are also important for MAPBr force fields, things get more complicated: the static properties of shrinked

MAPBr is more sensitive to parameters and global refinements are inevitable. In this step, we modified A_{OI} and ρ_{OI} for Br-(N, C) interactions in addition to the three scaling parameters complementarily. The interactions between lead atoms and cations are still unchanged.

The above procedures is not designed to fit functions with enough fitting parameters, but based on the systematic and physically-sound manner. There are only five parameters: three for scaling and the rest for phase refinements, but we found that the force fields of MAPBr can be obtained sufficiently as validated in the following sections. The practical parameters are shown in Appendix.

6-2. Structural properties

In this section, we demonstrate the rationality of the developed MYP potential for MAPBr by evaluating three static properties: the atomic charge, cohesive energy curve and rotational barrier. The DFT data and MAPI results in the previous research [15] are also shown for comparison. We performed the one-shot classical simulations by using the DL_POLY code [18], where the cubic ($Pm\bar{3}m$, $Z = 1$) $8 \times 8 \times 8$ super cell of MAPBr is adopted. References are obtained as one-shot DFT with the cubic unit cell with $8 \times 8 \times 8$ Monkhorst-Pack grids for k-point sampling, where the VASP code [19, 20] is adopted with GGA-PBE functional.

ATOMIC CHARGES We calculated the *ab initio* charges based on Bader's analysis. The results are reported in Table 6-1, showing that MAPBr has a more ionic inorganic lattice than MAPI. Comparing between MAPI, the averaged ratio of the Bader charges in MAPBr is higher, which mainly comes from insignificant charges of C atoms. When they are excluded, the averaged ratio is 1.05, very close to the one of MYP potential corresponding to β.

Table. 6-1. Partial atomic charges of MAPBr and MAPI obtained by *ab initio* charge analysis and actual parameters in MYP potentials. The ratio between MAPBr and MAPI are also shown, whose averaged ratio are calculated based on their formula unit.

	Pb	Br/I	C	N	H	average
MAPBr (Bader)	1.0695	-0.6132	0.0949	-1.1946	0.6233	
MAPI (Bader)	0.8604	-0.5337	0.0413	-1.2010	0.6335	
ratio	1.24	1.15	2.30	0.99	0.98	1.16
MAPBr (MYP)	2.0909	-1.1639	0.7941	-1.1330	0.2899	
MAPI (MYP)	2.0300	-1.1300	0.7710	-1.1000	0.2815	
ratio	1.03	1.03	1.03	1.03	1.03	1.03

COHESIVE ENERGIES The cohesive energy curves are evaluated as a function of lattice spacing, shown in Fig 6-1. All energy curves are adjusted according to their cohesive energies, which are evaluated by fitting to the universal energy relation [15, 21], and the lattice spacing of DFT data is also shifted based on the experimental lattice constant. MYP stable lattice spacing $(5.91\ \text{Å})$ finely reproduces the experimental lattice constant, [22, 23] where the cohesive energy curvature is also consistent to the DFT result. The energy curves deviate from the one of DFT as the lattice spacing leaves from the stable configuration, which comes from the fact that the electrostatic interactions are approximated by the fixed point charges. In spite of this difference, the fitted universal energy relation gives the cohesive energy of MAPBr $(8.60\ \text{eV})$ and bulk modulus $(0.235\ \text{Mbar})$ in sufficient agreement with those of DFT data [22] (Table 6-2). Comparing with MAPI, MAPBr in cubic phase has the shorter lattice constant than that of MAPI $(6.27\ \text{Å})$ and higher cohesive energy than the opponent $(7.8\ \text{eV})$. Bulk modulus, B, of MAPBr is also higher $(0.18\ \text{Mbar}$ for MAPI), whose magnitude relation is also consistent with the previous measurements. Assuming isotropic homogeneous elastic materials, we can evaluate other mechanical properties: the Young's modulus, E, and the shear modulus, G, from the bulk modulus, with the following relations and the Poisson's ratio, τ:

$$B = E/3(1-2\tau),$$
$$G = E/2(1+\tau). \tag{6-4}$$

Here we adopt the DFT Poisson's ratio in the pervious research [22] and estimate the other properties, compared with the other experimental and theoretical results as shown in Table 6-2 [22, 24]. MYP potential is found to reproduce the stiffer mechanical properties of MAPBr than those of MAPI; while overestimates both of the experimental and theoretical results, which results from the point charge approximation.

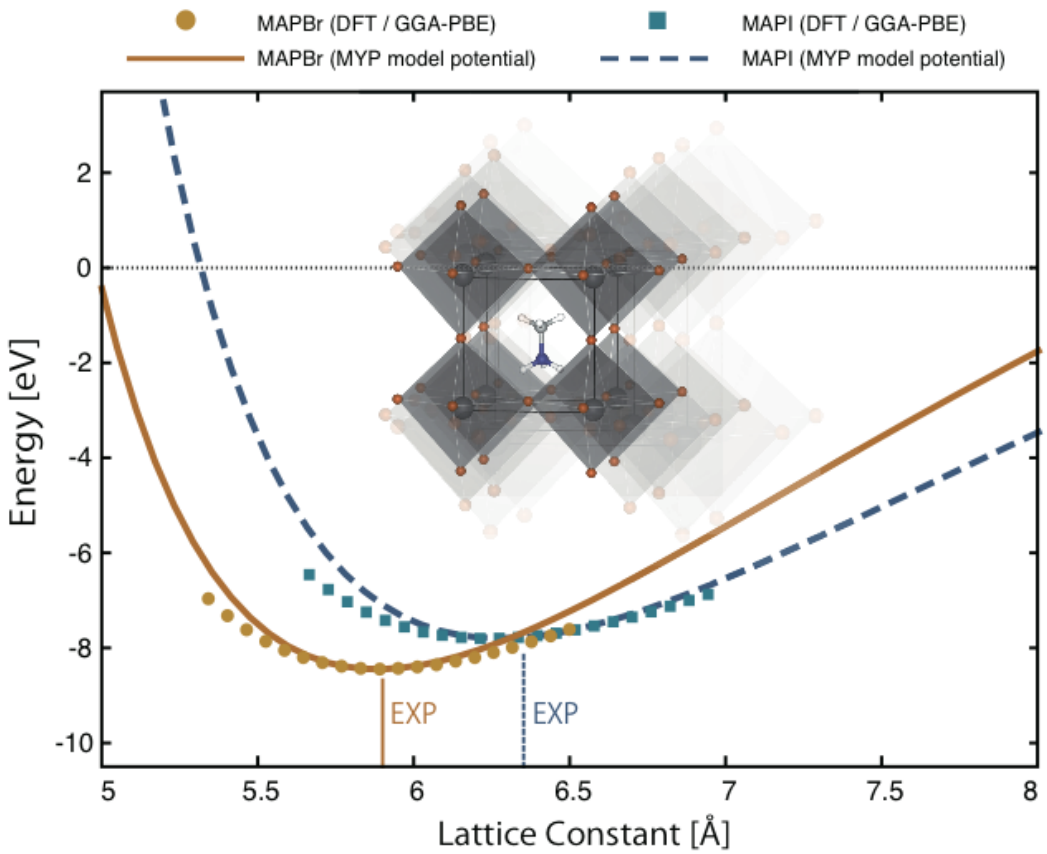

Fig. 6-1. Energy profile of cubic MAPBr with hydrostatic deformation. The origin of energy is defined with considering the cohesive energy. The MAPI results [15] and experimental lattice constant of cubic phase [22, 23] are also shown for comparison.

Table. 6-2. Mechanical properties of MAPBr and MAPI in experiments [24], DFT calculations [22], and MYP potential. Bold indicates the measured values in this work, and asterisk does the evaluated values with Eq. (6-4).

			phase	E (GPa)	B (GPa)	G (GPa)	τ
MAPBr	[24]	(EXP)	cubic	19.6	15.6*	7.6*	0.29 [22]
MAPI	[24]	(EXP)	tetra	14.0-1.43	13.9*	5.4*	0.33 [22]
MAPBr	[22]	(DFT)	cubic	29.1	22.6	10.4	0.29
MAPI	[22]	(DFT)	tetra	12.8	12.2	3.7	0.33
MAPI	[22]	(DFT)	cubic	22.2	16.4	8.7	0.28
MAPBr		(MYP)	cubic	29.6*	**23.5**	11.5*	0.29 [22]
MAPI		(MYP)	cubic	23.8*	**18.0**	9.28*	0.28 [22]

ROTATIONAL BARRIERS The static rotational barriers are also reported in Fig 6-2. In this observation, we also adopted cubic phase structures and rotated cations in (001) crystallographic plane with keeping its symmetry and most stable volume. Other calculation condition is the same as those of the cohesive energy analysis both for the classical and DFT calculations. We can see that the highest rotational barrier of MYP is 0.63 eV and it is almost identical to the DFT results. The previous research evaluated the barrier of MAPI [15], which is lower that that of MAPBr for whole angle range. The higher rotational barrier of bromide compounds comes from shorter and stronger organic-inorganic interactions; but we should take care of that this is not identical to the difficulties of rotations of cations at the finite temperature and not to the higher transition temperature. Without the rigid symmetry and periodicity, the lattice can be easily deformed with the position of cations, when the strong interactions also have a positive impact on rotations by making adequate meta-stable configurations. Indeed MAPBr has lower transition temperature from orthorhombic to tetragonal phase in experiment [23, 25], which our potential reproduce as shown in the following section. We can also find that there are convexoconcaves at around 90 and 270° only in the MYP energy profile. Similar to the cohesive energy curves, the point charge approximations make it difficult to modify the detailed barriers with keeping their heights. Yet at finite temperature, the cations rotate via various paths with thermal fluctuations, so such difference is expected to be thermally averaged and have less effect.

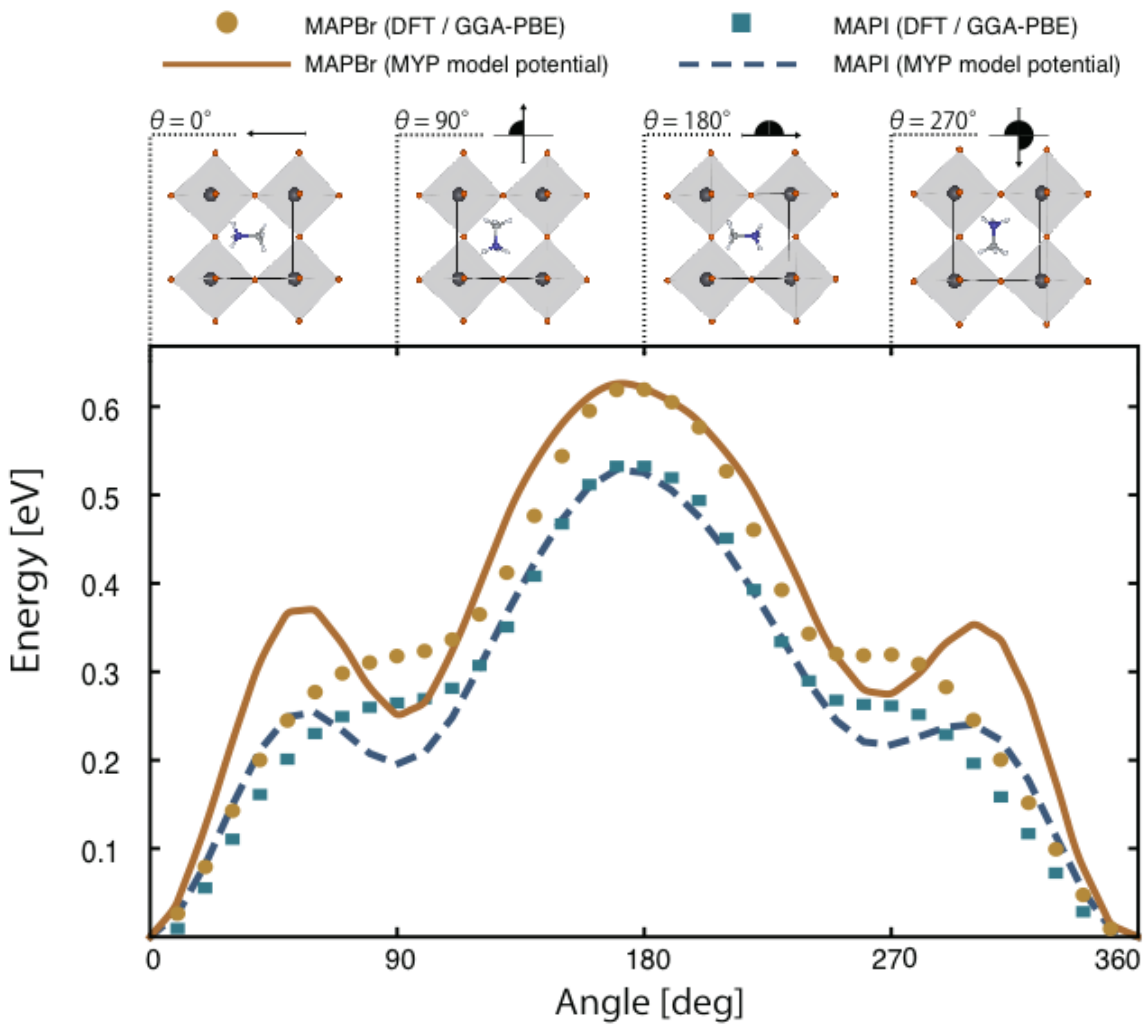

Fig. 6-2. Energy profile of MAPBr bulk during rotation of the molecular cations, which is also compared with the previous MAPI results [15]. The rotation is performed within a (001) crystallographic plane as shown in upper schematic figures.

6-3. Phase transitions

SHAPE DEFORMATION We move on to the phase transition properties of MAPBr. There are still several ambiguities of the phase transition in organic-inroganic halides, especially for MAPBr. In X-ray diffractions [23], MAPBr brings four different phases: the one at the lowest temperature is orthorhombic phase ($Pnma$) and stands till $140-150$ K; then it turns into the first tetragonal phase ($P4/mmm$); but is easily deformed into the second tetragonal phase ($I4/mcm$) at around 155 K; the last phase with the highest temperature appears from 237 K and has cubic symmetry ($Pm\bar{3}m$). In contrast, neutron diffraction has not shown distinguished pattern as $P4/mmm$ and implied an intermediate structure disordered more dynamically [26]. Yet at least, we can expect that there are roughly three phases, namely orthorhombic, tetragonal, and cubic, whose transition temperatures are located at around 150 K and 240 K. Then the structures with MYP potential are evaluated with different temperatures and check the reproducibility and limit of the potential in terms of their appearances, volumes, symmetry, and dynamics of cations. Every calculations start from the orthorhombic $4\times4\times4$ supercell and thermalized under the $N\sigma T$ Nosé-Hoover thermobarostat: with constant temperature and zero stress. Each system is equilibrated for at least 0.15 ns, whose properties are averaged over successive 0.15 ns. First, we pick up three typical structures at 50, 170, and 300 K to check the phase of MAPBr, shown in Fig. 6-3. While we can see that the structure at 50 K is in orthorhombic phase with characteristic octahedral tilt, $a^+b^-b^-$, one at 170 K is distorted only along c-axis, $a^0a^0c^-$, characterized as tetragonal phase [27, 28]. The 300 K snapshot is described as the averaged structures around 0.30 ns and clearly shows very symmetrical structures with no tilting, $a^0a^0a^0$. We also show the results at 155 K, where the phase is once transformed from orthorhombic to tetragonal-like phase but equilibrated into orthorhombic over simulation time. In the snapshot at 0.15 ns, the lattice shows partial $a^0a^0c^-$

tilts and rotations of cations. Such dynamics stands during 0.20 ns, and then the lattice turns into orthorhombic phase with a different tilting direction from the initial structure. The above qualitative observation is consistent to the experimental phase transition temperatures.

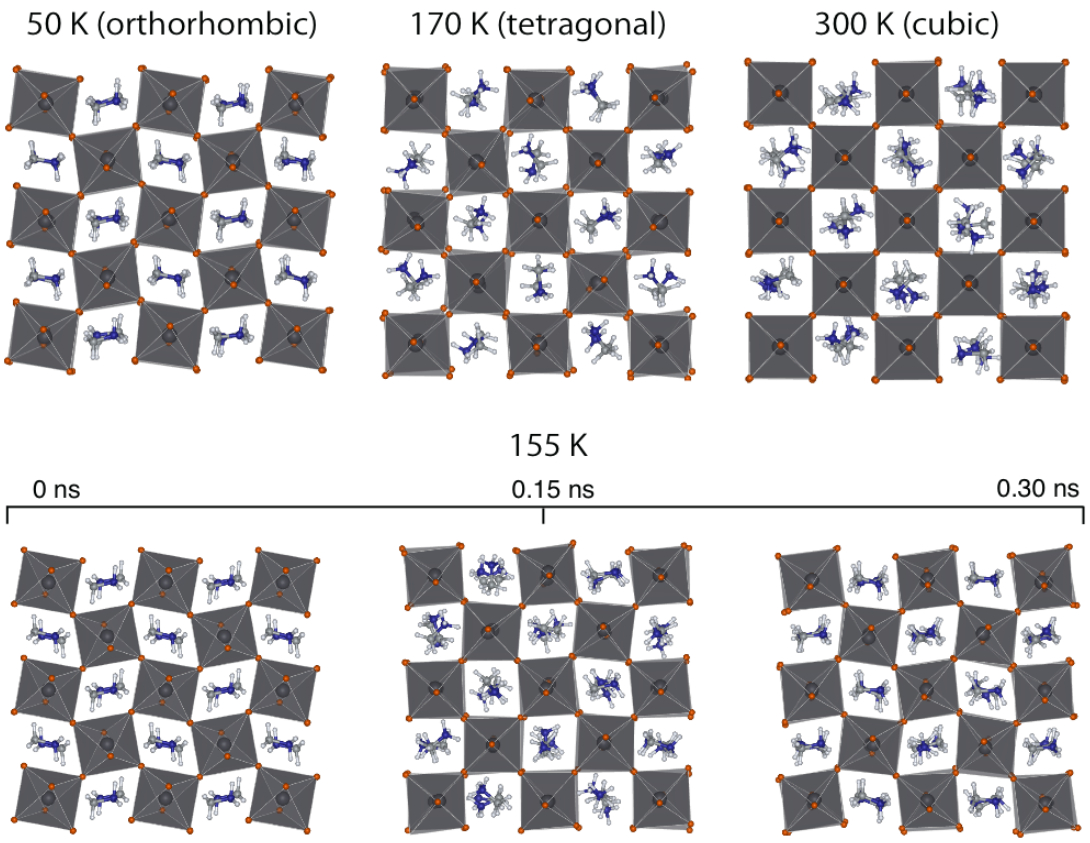

Fig. 6-3. (Top panel) MAPBr structure thermalized under different temperatures and zero stress. Inorganic frame at 300 K is averaged for 6 structures around 0.30 ns. (Bottom panel) Snapshots of MAPBr during $N\sigma T$ run. Deformed tetragonal-like structures are observed during rearrangement between orthorhombic structures.

The top panel of Fig. 6-4 shows the volume expansion of MAP(Br/I) with increasing temperature in terms of a pseudo cubic lattice constant, indicated by $V^{1/3}$. According to the static analysis of cohesive energy, the volume of MAPBr is little smaller than one of MAPI throughout the whole temperature. We can see that the volume increases with temperature especially at some temperature region: 140-170 K for MAPBr and 150-200 K for MAPI. The previous research

about MAPI suggested that this change of slope is related to the phase transition from orthorhombic to tetragonal [15], which is also consistent to MAPBr. The anisotropy of lattice is evaluated as the ratio between the largest and minimum lattice length, c/a, shown in the bottom panel of Fig. 6-4. At low temperature, c/a is higher than equality and corresponds to the low symmetric phase, $Pnma$. Passing over 140-170 K, c/a abruptly decrease to $\sim$1, indicating the phase transition from orthorhombic to tetragonal. There are no notable changes at the phase transition temperature to cubic phase, which is the limit of MYP potentials observed in MAPI previously [15]. Comparing with MAPI, the change of anisotropy in MAPBr has almost the same trend, but c/a in orthorhombic phase is slightly higher than that of MAPI. While the absolute value of c/a is much smaller than the computational or experimental results, the developed potential reproduce proper relative anisotropy [23].

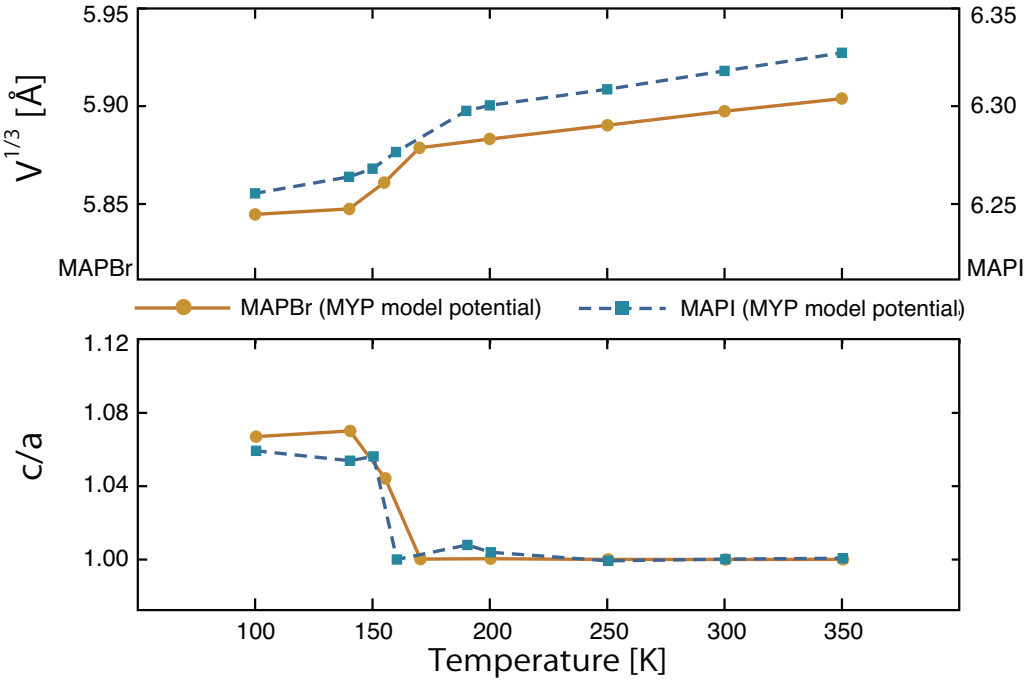

Fig. 6-4. Structure deformation with temperature increase in terms of pseudo cubic lattice constants $V^{1/3}$ (top panel) and isotropies evaluated with (c/a) (bottom panel). Results of MAPI are also shown for comparison.

ROTAIONAL DYNAMICS At the end of the validation, we discuss the detailed rotational dynamics of cations in MAPBr. To qualify an orientation of each molecule, the normalized direction vector of N-C backbone, $\boldsymbol{n}$, is evaluated in the polar coordinate system, as shown in the top of Fig. 6-5. Orange line indicates the orientation of cations towards orthogonal coordinates $\boldsymbol{x}, \boldsymbol{y}, \boldsymbol{z}$: *xy*-plane corresponds to (001) crystallographic plane and $\boldsymbol{z}$ is parallel to tetragonal tilting axis. Then $\boldsymbol{n}$ can be written as $\boldsymbol{n} = (\sin\theta\cos\varphi,\ \sin\theta\sin\varphi,\ \cos\theta)$, and $(\varphi, n_{\boldsymbol{z}} = \cos\theta)$ is mapped for 50-350 K. The segment of $(\varphi, n_{\boldsymbol{z}} = \cos\theta)$ map is identical to the surface element dS for rotations, whose cumulative frequency gives the fine distribution of cation orientations.

In the bottom of Fig. 6-5, we report the orientation map at each temperature. At the lowest temperature, cations are deeply trapped at the stable orthorhombic configurations and keep high symmetric positions around $(\varphi = 0, 180°, \cos\theta = 0)$: the distribution is symmetrical to $\cos\theta = 0$ axis and periodic with $180°$ to φ. The map shows distinct two robes symmetric to $\varphi = 0°$ and $\varphi = 180°$ axis respectively. This means the N-C backbones at low temperature are pinned at (001) plane and lined in alternate directions. Increasing to 100 K, the robes expand a little bit to $\boldsymbol{z}$ direction with thermal fluctuations, but the almost same trend is observed. First change occurs at 140 K, where we can see several spots around $(\varphi = -90, 90°, \cos\theta = 1, -1)$, located as x-shaped. It indicates that flipping to $\boldsymbol{z}$ direction begins to be occasionally allowed. However the barrier of such flipping is still high to overcome by fluctuations, and orientated configurations along $\boldsymbol{z}$ axis is separated from the most stable one of orthorhombic phase. Moreover, the center dots $(\varphi = -90, 90°, \cos\theta = 0)$ also come to stand out, meaning that via these orientations cations can be flipped from one to the other of orthorhombic stable positions. Such dots are completely isolated; indicating these flipping is rare and unstable at this temperature. At around 155 K, the phase transition temperature from orthorhombic to tetragonal, barrier towards $\boldsymbol{z}$ direction is broken and

clear x-shaped map appears. Center dot is also spread but a blank space between the x-shapes implies that the direct rotation in (001) plane is still bottlenecked. But now the edges of $\cos\theta = 1, -1$ connect two x-shapes and indirect flipping starts. The different features are found approaching to 170 K. We can see that the stable orientations for orthorhombic structures are now collapsed; in other words, x-shaped distributions are torn into two lines. Then the map shows four stripes distributed uniformly at $\varphi = -45, 45, 135, 215^{\circ}$ in (001) crystallographic plane, which indicates the linear paths for free rotations along $\boldsymbol{z}$-axis. The above features correspond to that cations are located at one of four positions evenly distributed in (001) plane and isotropically rotate along $\boldsymbol{z}$-axis, which is suggested just in tetragonal phase with $a^0a^0c^-$ tilting [29, 30]. So we can conclude that the change of orientation map between 155 and 170 K specifies the phase transition from orthorhombic to tetragonal. It is also note that the configurations sampled between the stripes are mainly located at $\cos\theta = 0$ and weakly connect the stable orientations with each other. So flipping between the four positions in (001) plane seems to be already allowed. After the tetragonal transition, while there are little changes with temperature increase, the blank space between stripe distributions are gradually filled from the mentioned $\cos\theta = 0$ path. It means that the molecular cations begin to rotate in all directions as energy barriers are thermalized, resulting in isotropic orientations, tiltings, and cubic phase.

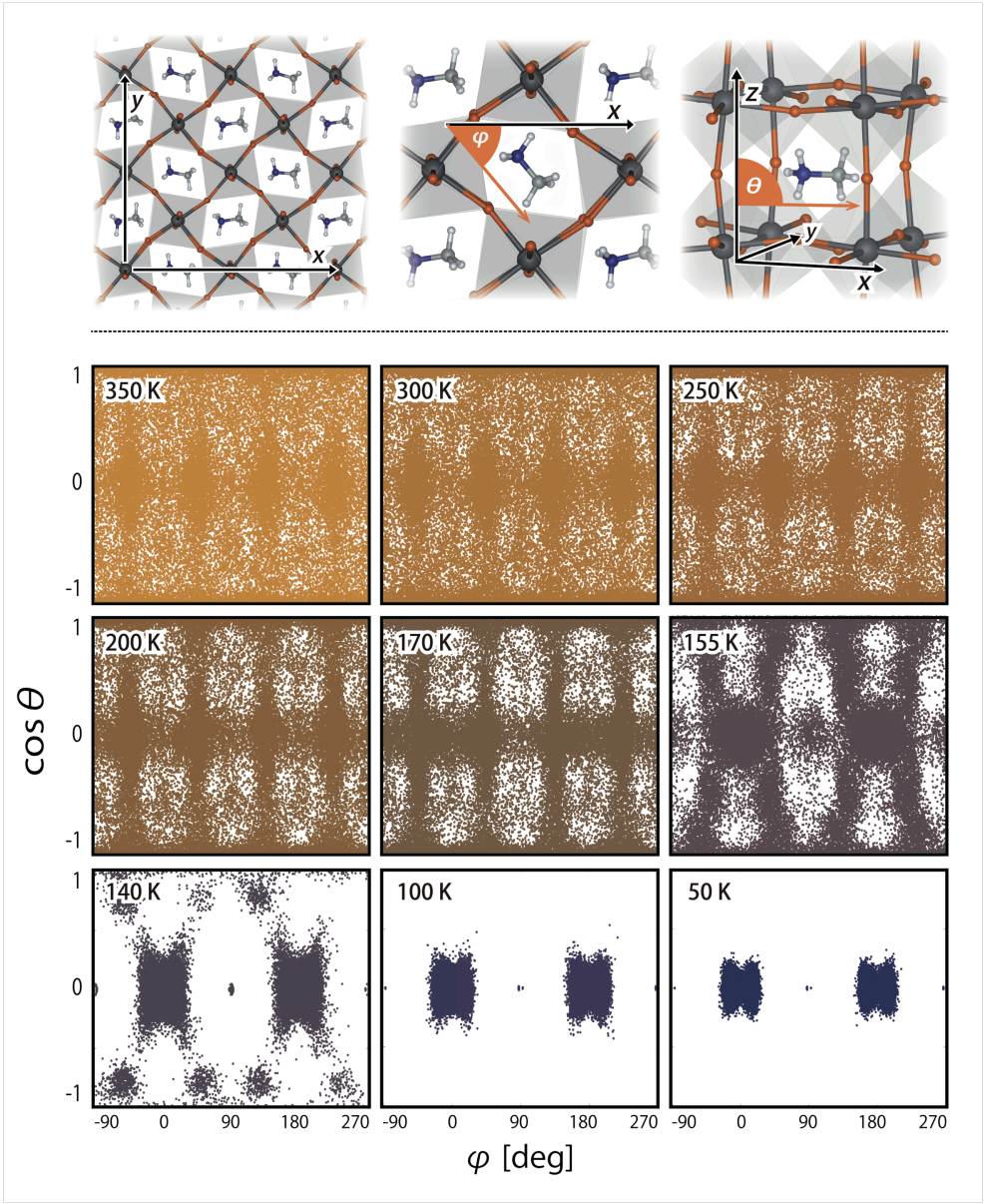

Fig. 6-5. (Top panel) Polar coordinate system in orthorhombic MAPBr whose axis along ***z***-axis in orthogonal coordinates. Orientations of molecular cations are described as orange lines and evaluated with φ and θ shown as partial orange circles. (Bottom panel) Distribution maps of molecular orientations, $(\varphi, n_z = \cos\theta)$, at several temperatures between 0 and 350 K. Maps are shown in two-color gradation according to their temperatures.

6-4. Vibrational mode properties

ROTATIONAL TIMES In order to further characterize the rotational dynamics of cations, we calculate the molecular reorientational time τ in MAPBr crystal at room temperature. This quantity can be extracted from the orientational auto correlation function defined as $\langle n_i(0) \cdot n_i(t) \rangle$, where $n_i(t)$ is the instantaneous direction of *i*-th MA cation and the average is performed over all different initial times and all molecular cations in the crystal [15]. If the directions of molecules are uncorrelated and the molecules are able to rotate, then the corresponding autocorrelation function is a decreasing exponential function of time. The reorientational times τ correspond to the decay times where autocorrelation functions are reduced by a factor e^{-1} as shown in Fig. 6-6.

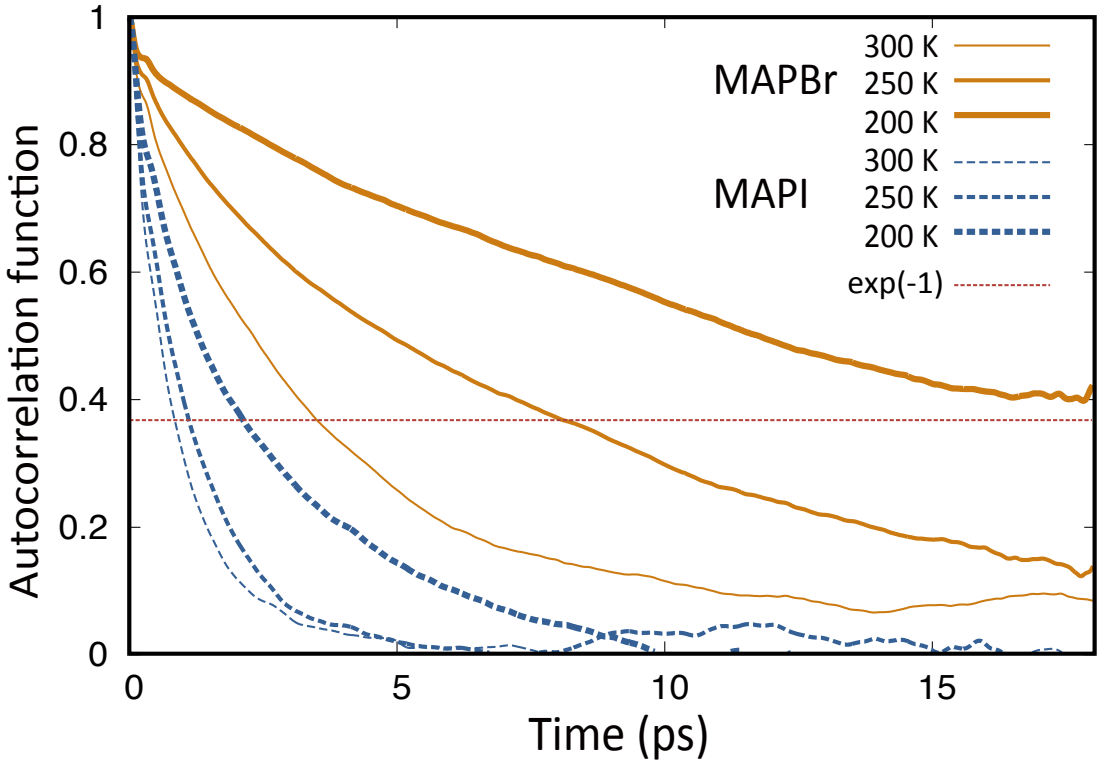

Fig. 6-6. Autocorrelation functions of MAPBr with three different temperatures. The red dotted line corresponds to e^{-1} used for evaluation of reorientation times. Results of MAPI are also shown for comparison [15].

For MAPBr at room temperature the MYP potential gives $\tau \sim 3.2$ ps in good agreement with the experimental time of 2.73 ps obtained from a millimeter-wave spectroscopy [23]. Furthermore, by performing a series of calculations in the range (300-200 K) it is possible to estimate an activation energy $E_a \sim 90$ meV that compares to the literature value of 77.5 meV [23]. Comparing with MAPI, the reorientation times of bromide compounds are clearly longer at any temperatures, which is consistent with the tight hybrid interactions and the higher energy barriers of the bromide compounds.

DENSITY OF STATES Finally, we evaluate the detailed vibrational properties of MAPBr. On the basis of Wiener-Khintchine theorem, Eq. (5-1), vDOSs are evaluated as power spectra $P(\omega)$ of velocity autocorrelation functions. The results with MYP potential for MAPI is reported to overestimate the experimental and *ab-initio* results in the low energy region, and the comparison between them needs a scaling factor, 1.27 [15]. We found that MAPBr bare results also overestimate the pervious data in the low energy region so scaled them in the same way. All calculations are performed with orthorhombic $4 \times 4 \times 4$ supercell and thermalized at 100-350 K with zero stress before the velocity sampling. The results of MAPBr are shown in Fig. 6-7, with those of MAPI for comparison, where the contribution of inorganic cage and molecular cations are separated.

First, we can see that the overall shape of vDOS for MAPBr is similar to the one of MAPI. The inorganic contribution is located in the only lower energy region and several molecular violations coupled with the inorganic lattice are located in the successive region. Increasing the temperature, the intensities of peaks are reduced and the energy shifts are observed, shown as dotted line in Fig. 6-7. As mention as the previous chapter, such shifts in the constant volume simulation

suggest that anharmonic couplings occur between these peaks, viz., the higher inorganic branches and lower molecular vibrations. Passing the phase transition temperature from orthorhombic to tetragonal, the both spectra are suddenly attenuated, and below $500\ \mathrm{cm}^{-1}$, only three branches survive in the molecular contribution. One is the rotational mode (R in Fig 6-5), another is the mixed motion called as X in the recent analysis [31], and the other is the twisting motion (Tw). While the appearance is almost identical, the energy of each branch in MAPBr is changed from MAPI. We can see that the inorganic contribution in MAPBr have higher energies than those in MAPI, which corresponds to the fact that iodine has the heavier atomic mass than bromide. At the same time, the characteristic molecular branches in the low energy region also have the same trend, implying that these vibrations are coupled with phonons of the inorganic frame. R branches in MAPBr have $9.45\ \mathrm{cm}^{-1}$ higher than those of MAPI; X is $12.7\ \mathrm{cm}^{-1}$ higher; for Tw $2.02\ \mathrm{cm}^{-1}$. These differences are observed in the experimental and DFT Raman analysis [14, 32, 33], for example, the difference in X peaks between MAPBr and MAPI is reported as 14-15 cm^{-1} [14], which is totally consistent to our results and indicates MYP potential with 1.27 scaling is robust also for anion substitutions. Another characteristics in MAPBr can be found in X and Tw branches. At low temperature, these branches have two distinctive peaks respectively; yet in MAPI, these peaks are easily dispersed and merged, found as Tw at 100 K. Conversely, MAPBr vDOS shows that distinctive peaks stand even at higher temperature, observed at 140 K for Tw, and 350 K for X. Now we expect that stable Tw and X indicate the small anharmonicity of organic-inorganic interactions in MAPBr, associated with the higher heat tolerance and thermal conductivity of this material.

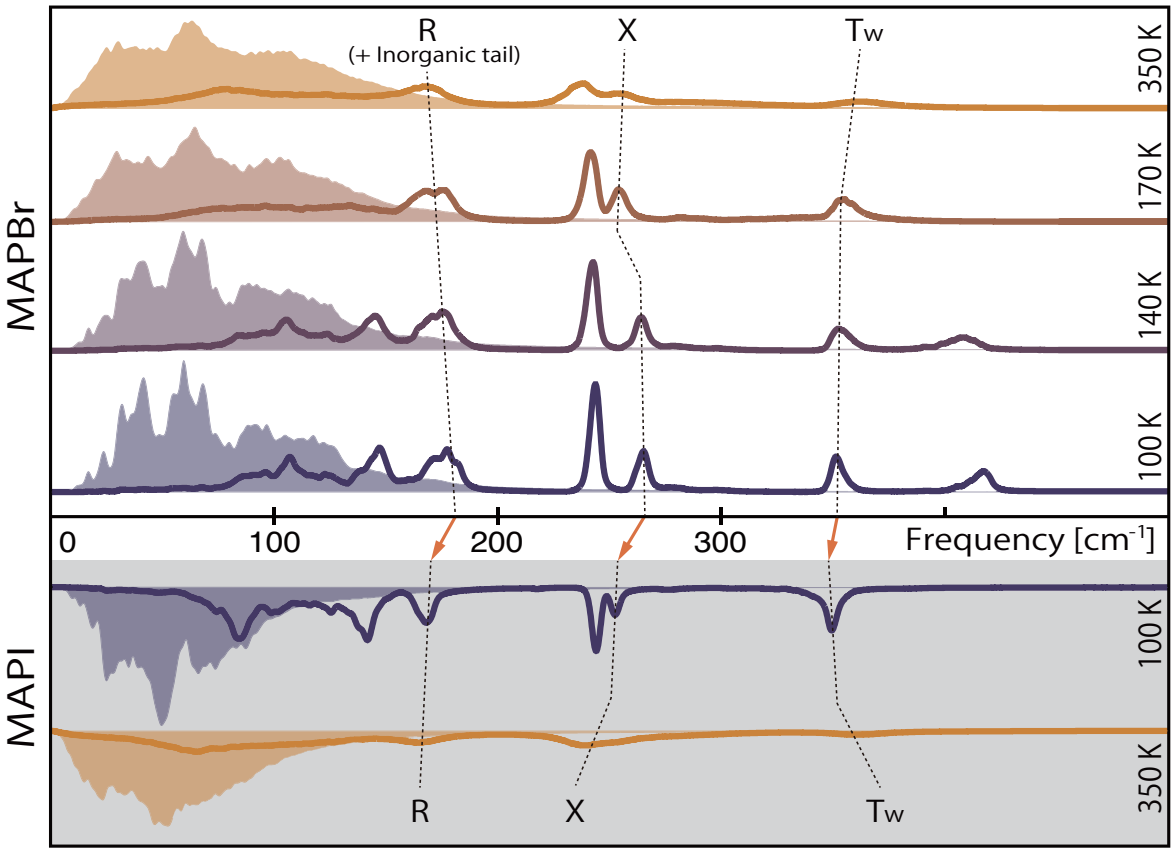

Fig. 6-7. Partial vDOSs of MAPBr (bright panel) and MAPI (shade panel): inorganic (filled area) and molecular (line) contributions. The energy range is focused on the lower energy region, 0-500 cm^{-1}, where the scaling factor should be induced. Temperature increase is shown as two-color gradation from 100 to 350 K.

5-4. Summary

In summary, we have proposed the reparameterization procedures for MAPBr from the force fields of MAPI. The operation consists of only three steps, (i) to shrink the inorganic frame, (ii) to enhance the rotational barrier, and (iii) the refinement for phase transitions. There are five free parameters, including three scaling parameters: α for inorganic interactions, β partial atomic charges, and γ hybrid interactions; with two Buckingham parameters related to bromide. We have found that the proper selection of fitting parameters brings MAPBr force fields with sufficient accuracy even by such simple procedure. The validation of the developed potential is performed both for the static and dynamical properties, showing the consistent lattice constant, cohesive energy curve, energy barrier for cation rotations, and phase transition temperatures related to detailed dynamics of molecules. The comparison with MAPI results provides the valid relationship between them: MAPBr has shorter lattice constant, higher cohesive energy, lower phase transition temperatures, and lager anisotropy in orthorhombic phase.

As a benchmark, we applied the developed potential to the reorientational time and density of states analyses and found that the experimental and DFT results are well reproduced with the universal scaling factor, which provides the robust basis for successive thermal and structural analysis of MAPBr. Specifically, the reorientation time of cations in bromide compounds is relatively slow according to the tight hybrid interactions in MAPBr. The stable Tw and X modes correspond to the small coupling via such interactions. Based on the analysis in the previous chapter, these characteristics are expected to result in the higher heat tolerance and thermal conductivity of this material. Adjusting the rate of substitution is now one of the promising methods to tailor the thermal properties of hybrid perovskite structures, and continuous studies of the substituted perovskites are required.

At last, the proposed detuning procedure does not depend on bromide nature in itself. So we can probably apply this method to other anion substitution such as methylammonium lead chloride. It is also expected that such straightforward procedure for reparameterization can be established for other substitutions: metal atoms and molecular cations substitutions. Combinations of such procedures evolve the force fields database about hybrid perovskite structures, which also makes a promising way to the new material design.

Appendix

We report all detuned parameters of MYP model potential for MAPBr. The parameters are written according to the format of FIELD file of the DL_POLY code.

```
MAPBr
UNITS           kcal
MOLECULES   3
Lead
        nummol  256
        atoms  1
        Pb   207.2   2.0909
FINISH
Bromide
        nummol  768
        atoms  1
        Br   79.904 -1.1639
FINISH
        nummol  256
        atoms  8
        H 1.0080 0.5562
        H 1.0080 0.5562
        H 1.0080 0.5562
        N 14.0100   -1.133
        C 12.0100   0.79413
        H3   1.0080 0.02369
        H3   1.0080 0.02369
        H3   1.0080 0.02369
        bonds  7
                harm   5 6   677.400   1.0910
                harm   5 7   677.400   1.0910
                harm   5 8   677.400   1.0910
                harm   4 1   738.000   1.0330
```

```
        harm    4 2   738.000   1.0330
        harm    4 3   738.000   1.0330
        harm    4 5   587.200   1.4990
    angles  12
        harm    7 5 8    78.0000   110.7400
        harm    6 5 7    78.0000   110.7400
        harm    6 5 8    78.0000   110.7400
        harm    3 4 5    92.4000   110.1100
        harm    2 4 3    81.0000   108.1100
        harm    2 4 5    92.4000   110.1100
        harm    1 4 2    81.0000   108.1100
        harm    1 4 3    81.0000   108.1100
        harm    1 4 5    92.4000   110.1100
        harm    4 5 6    98.0000   107.9100
        harm    4 5 7    98.0000   107.9100
        harm    4 5 8    98.0000   107.9100
    dihedrals 9
        cos   3 4 5 6 0.1556 0.0000 3.0000 0.833   0.500
        cos   3 4 5 7 0.1556 0.0000 3.0000 0.833   0.500
        cos   3 4 5 8 0.1556 0.0000 3.0000 0.833   0.500
        cos   2 4 5 6 0.1556 0.0000 3.0000 0.833   0.500
        cos   2 4 5 7 0.1556 0.0000 3.0000 0.833   0.500
        cos   2 4 5 8 0.1556 0.0000 3.0000 0.833   0.500
        cos   1 4 5 6 0.1556 0.0000 3.0000 0.833   0.500
        cos   1 4 5 7 0.1556 0.0000 3.0000 0.833   0.500
        cos   1 4 5 8 0.1556   0.0000   3.0000 0.833   0.500
FINISH
vdw 21
Pb Pb   buck      74933300.5606326      0.123246948356808    0.000000
Pb Br   buck      110223.38165565       0.302100469483568    0.000000
Br Br   buck      24274.90558983        0.45286103286385  654.4127155
Pb N    buck      32690390.937995       0.150947      0.000000
Pb H    lj  0.014 2.26454
Pb C    buck      32690390.937995       0.150947      0.000000
```

```
Pb H3  lj  0.014                2.70999
Br N   buck  94836.351975893  0.3352375  0.000000
Br H   lj  0.05125             2.45535714285714
Br C   buck  94836.351975893  0.3352375  0.000000
Br H3  lj 0.05125               2.76785714285714
N  N   lj  0.1700              3.25000
N  H   lj  0.0517              2.15950
N  C   lj  0.1364              3.32480
N  H3  lj  0.0517              2.60500
H  H   lj  0.0157              1.06910
H  C   lj  0.0414              2.23440
H  H3  lj  0.0157              1.51450
C  C   lj  0.1094              3.39970
C  H3  lj  0.0414              2.67980
H3 H3  lj  0.0157              1.96000
CLOSE
```

Here the scaling factors in Eqs. (6-2) and (6-3) are $\alpha = 1.065$, $\beta = 1.03$, and $\gamma = 1.12$. As mentioned in the reparameterization step (iii), we modified $(A_{\mathrm{OI}}, \rho_{\mathrm{OI}})$ for Br-(N,C) from (100836.351975893, 0.3057375) to (94836.351975893, 0.3352375). Such modifications are less than 10 % but strongly affects to the phase transition temperatures. Especially, ρ_{OI} is crucial and fourth decimal place is still important.

Bibliography

[1] Kim, Y.-J.; Dang, T.-V.; Choi, H.-J.; Park, B.-J.; Eom, J.-H.; Song, H.-A.; Seol, D.; Kim, Y.; Shin, S.-H.; Nah, J. and Yoon, S.-G. (2016). Piezoelectric properties of $CH_3NH_3PbI_3$ perovskite thin films and their applications in piezoelectric generators. *J. Mater. Chem. A* 4: 756-763.

[2] Coll, M.; Gomez, A.; Mas-Marza, E.; Almora, O.; Garcia-Belmonte, G.; Campoy-Quiles, M. and Bisquert, J. (2015). Polarization Switching and Light-Enhanced Piezoelectricity in Lead Halide Perovskites. *J. Phys. Chem. Lett.* 6: 1408-1413.

[3] Tanaka, K.; Takahashi, T.; Ban, T.; Kondo, T.; Uchida, K. and Miura, N. (2003). Comparative study on the excitons in lead-halide-based perovskite-type crystals $CH_3NH_3PbBr_3$ $CH_3NH_3PbI_3$. *Solid State Commun.* 127: 619−623.

[4] Giorgi, G.; Fujisawa, J.-I.; Segawa, H. and Yamashita, K. (2014). Cation Role in Structural and Electronic Properties of 3D Organic-Inorganic Halide Perovskites: A DFT Analysis. *J. Phys. Chem. C* 118: 12176-12183.

[5] D'Innocenzo, V.; Grancini, G.; Alcocer, M. J. P.; Kandada, A. R. S.; Stranks, S. D.; Lee, M. M.; Lanzani, G.; Snaith, H. J. and Petrozza, A. (2014). Excitons versus free charges in organo-lead tri-halide perovskites. *Nat. Commun.* 5: 3586.

[6] Kieslich, G.; Sun, S. and Cheetham, A. K. (2014). Solid-state principles applied to organic-inorganic perovskites: new tricks for an old dog. *Chem. Sci.* 5: 4712-4715.

[7] Kieslich, G.; Sun, S. and Cheetham, A. K. (2015). An extended Tolerance Factor approach for organic-inorganic perovskites. *Chem. Sci.* 6: 3430-3433.

[8] Schmidt, L. C.; Pertegás, A.; González-Carrero, S.; Malinkiewicz, O.; Agouram, S.; Espallargas, G. M.; Bolink, H. J.; Galian, R. E. and Pérez-Prieto, J. (2014). Nontemplate

Synthesis of $CH_3NH_3PbI_3$ Perovskite Nanoparticles. *J. Am. Chem. Soc.* 136: 850-853.

[9] Edri, E.; Kirmayer, S.; Cahen, D. and Hodes, G. (2013). High Open-Circuit Voltage Solar Cells Based on Organic-Inorganic Lead Bromide Perovskite. *J. Phys. Chem. Lett.* 4: 897-902.

[10] Noh, J. H.; Im, S. H.; Heo, J. H.; Mandal, T. N. and Seok, S. I. (2013). Chemical Management for Colorful, Efficient, and Stable Inorganic-Organic Hybrid Nanostructured Solar Cells. *Nano Lett*. 13: 1764-1769.

[11] Eperon, G. E.; Stranks, S. D.; Menelaou, C.; Johnston, M. B.; Herz, L. M. and Snaith, H. J. (2014). Formamidinium lead trihalide: a broadly tunable perovskite for efficient planar heterojunction solar cells. *Energy Environ. Sci.* 7: 982-988.

[12] Butler, K. T.; Frost, J. M. and Walsh A. (2015). Band alignment of the hybrid halide perovskites $CH_3NH_3PbCl_3$, $CH_3NH_3PbBr_3$ and $CH_3NH_3PbI_3$. *Mater. Horiz.* 2: 228-231.

[13] Wright, A. D.; Verdi, C.; Milot, R. L.; Eperon, G. E.; Perez-Osorio, M. A.; Snaith, H. J.; Giustino, F.; Johnston, M. B. and Herz, L. M. (2016). Electron-phonon coupling in hybrid lead halide perovskites. *Nat. Commun.* 7: 11755.

[14] Leguy, A. M. A.; Goni, A. R.; Frost, J. M.; Skelton, J.; Brivio, F.; Rodriguez-Martinez, X.; Weber, O. J.; Pallipurath, A.; Alonso, M. I.; Campoy-Quiles, M.; Weller, M. T.; Nelson, J.; Walsh, A. and Barnes, P. R. F. (2016). Dynamic disorder, phonon lifetimes, and the assignment of modes to the vibrational spectra of methylammonium lead halide perovskites. *Phys. Chem. Chem. Phys.* 18: 27051-27066.

[15] Mattoni, A.; Filippetti, A.; Saba M. I. and Delugas, P. (2015). Methylammonium Rotational Dynamics in Lead Halide Perovskite by Classical Molecular Dynamics: The Role of Temperature. *J. Phys. Chem. C* 119: 17421-17428.

[16] Ponder, J. W. and Case, D. A. (2003). Force fields for protein simulations. *Adv. Protein Chem.*

66: 27-85.

[17] Wang, J.; Wolf, R. M.; Caldwell, J. W.; Kollman, P. A. and Case, D. A. (2004). Development and testing of a general AMBER force field. *J. Comput. Chem.* 25: 1157-1174.

[18] Todorov, I. T.; Smith, W.; Trachenko, K. and Dove, M. T. (2006). DL_POLY_3: new dimensions in molecular dynamics simulations via massive parallelism. *J. Mater. Chem.* 16: 1911-1918.

[19] Kresse, G. and Furthmüller, J. (1996). Efficiency of *ab-initio* total energy calculations for metals and semiconductors using a plane-wave basis set. *Comput. Mater. Sci.* **1996**, *6*, 15−50.

[20] Kresse, G. and Furthmüller, J. (1996). Efficient iterative schemes for *ab initio* total-energy calculations using a plane-wave basis set. *Phys. Rev. B* 54: 11169−11186.

[21] Rose, J. H.; Smith, J. R.; Guinea, F. and Ferrante, J. (1984). Universal features of the equation of state of metals. *Phys. Rev. B* 29: 2963-2969.

[22] Feng, J. (2014). Mechanical properties of hybrid organic-inorganic $CH_3NH_3BX_3$, (B = Sn, Pb; X = Br, I) perovskites for solar cell absorbers. *APL Mater.* 2: 081801.

[23] Poglitsch, A. and Weber, D. (1987). Dynamic disorder in methylammoniumtrihalogen-oplumbates (II) observed by millimeter-wave spectroscopy. *J. Chem. Phys.* 87: 6373-6378.

[24] Rakita,Y.; Cohen, S. R.; Kedem, N. K.; Hodes, G. and Cahen, D. (2015). Mechanical properties of $APbX_3$ (A = Cs or CH_3NH_3; X = I or Br) perovskite single crystals. *MRS Commun.* 12: 623-629.

[25] Knop, O.; Wasylishen, R. E.; White, M. A.; Cameron, T. S. and Oort, M. J. M. V. (1990). Alkylammonium lead halides. Part 2. $CH_3NH_3PbX_3$ (X = Cl, Br, I) perovskites: cuboctahedral halide cages with isotropic cation reorientation. *Can. J. Chem.* 68: 412-422.

[26] Swainson, I. P.; Hammond, R. P.; Soullière, C.; Knop, O. and Massa, W. (2003). Phase

transitions in the perovskite methylammonium lead bromide, $CH_3ND_3PbBr_3$. *J. Solid State Chem.* 176: 97-104.

[27] Glazer, A. M. (1972). The classification of tilted octahedra in perovskites. *Acta Cryst.* B28: 3384-3392.

[28] Howard, C. J. and Stokes, H. T. (1998). Group-Theoretical Analysis of Octahedral Tilting in Perovskites. *Acta Cryst.* B54: 782-789.

[29] Oku, T. (2015). Crystal structures of $CH_3NH_3PbI_3$ and related perovskite compounds used for solar cells. *Solar Cells - New Approaches and Reviews*, ch. 3. InTech. ISBN 9789535121848.

[30] Kawamura, Y.; Mashiyama, H. and Hasebe, K. (2002). Structural Study on Cubic-Tetragonal Transition of $CH_3NH_3PbI_3$. *J. Phys. Soc. Jpn.* 71: 1694-1697.

[31] Caddeo, C.; Melis, C.; Saba, M. I.; Filippetti, A.; Colombo, L.; Mattoni. A. (2016). Tuning the thermal conductivity of methylammonium lead halide by the molecular substructure. *Phys. Chem. Chem. Phys.* 18: 24318-24324.

[32] Niemann, R. G.; Kontos, A. G.; Palles, D.; Kamitsos, E. I.; Kaltzoglou, A.; Brivio, F.; Falaras, P. and Cameron, P. J. (2016). Halogen Effects on Ordering and Bonding of $CH_3NH_3^+$ in $CH_3NH_3PbX_3$ (X = Cl, Br, I) Hybrid Perovskites: A Vibrational Spectroscopic Study. *J. Phys. Chem. C* 120: 2509-2519.

[33] Ledinský, M.; Löper, P.; Niesen, B.; Holovský, J.; Moon, S.-J.; Yum, J.-H.; Wolf, S. D.; Fejfar, A. and Ballif, C. (2015). Raman Spectroscopy of Organic-Inorganic Halide Perovskites. *J. Phys. Chem. Lett.* 6: 401-406.

CHAPTER 7

CONCLUDING REMARKS

In this thesis, we investigated the structural effects on the thermal transport properties and proposed the design guidelines to control them. In order to go beyond the supplementary control with superstructures, our aim focused on finding some structural factors for controlling thermal properties, which should lead to innovative materials. The first-principles or classical calculation is accordingly employed as to be appropriate to the required system sizes or accuracies, which enable us to discuss the variety of the structural dependencies. We begin with the SWCNT, one-dimensional conductor, and its chirality dependence, and develop the discussion to the complex structures including the non-bonded interactions: DWCNT, MAPI, and MAPBr, summarized as follows.

In Chapter 3, we adopted the SWCNT models and focused on their ballistic phonon transports, which is especially important in the nanoscale devices. In particular, the chirality dependence of their thermal transport properties is investigated by using the NEGF method with the first-principles calculations. It is found that chirality of CNT affects their thermal properties via the modification of their vibrational density of states and the localization or polarization of phonon modes. Such effects result in the different thermal conductances and the different length of quantized plateaus at low temperature, which cannot be explained wholly only by the radial dependence. In spite of the definite dependence, the chirality effects on the thermal properties are less significant than those on others like electronic properties, indicating that the thermal design of tubular structures based on their chirality seems not feasible.

Chapter 4 discussed about the multi-walled effects on the thermal properties by holding

DWCNT up as an example, where the non-bonded interactions are introduced along the non-conducting direction. For comparison, the constitutive SWCNTs and their ideal parallel circuit are also investigated. The results of the thermal conductance showed that the non-bonded interactions are effective in the suppression of thermal transport especially at low temperature, and reduced conductance corresponds to one of the outer layer SWCNT. We analyzed such behaviors by using the coupled vibration model, elucidating that the *in-phase* modes govern the thermal transport properties at low temperature and they can be tailored by the intensities of the non-bonded interactions and the weight ratios of components.

The above studies raise the possibility of composite structures with the non-bonded interactions and high weight ratios, and organic-inorganic hybridizations are the typical systems meeting such requirements. The organic-inorganic hybrid halide perovskites are observed to have the quite low thermal conductivity in experiment, and Chapter 5 aimed to understand the suppression mechanism in MAPI. For considering the uncrystallized motion of methylammonium cations, we proposed the procedure to develop the empirical force fields with high accuracy by fitting to the first-principles calculations. With the developed potential function, the thermal conductivities of MAPI and the models with different embedded components are calculated. Comparison between the results showed that the rotational motions of cations are coupled with the translations, via which the separated optical phonon modes in the inorganic lattice become to be coupled with each other, resulting the suppression of the thermal transport properties. This mechanism indicates the possibility of thermal design based on the motions of organic molecules and the inorganic-organic interactions, which is confirmed by the deuterated models.

In Chapter 6, we further validated the control possibility proposed in Chapter 5, by studying the halide substitution of hybrid perovskites. MAPBr is adopted, which empirical force

fields are developed by detuing those of MAPI. The detuning procedures are designed to achieve both of the accuracy and the transferability in order to accept the enormous degrees of freedom for material design in the hybrid perovskite structures. We validate the detuning procedures in terms of the structural properties, phase transitions, and the rotational motions of cations. The developed force field showed that the vibrational modes of organic molecules in MAPBr have higher energies and less anharmonicity than those in MAPI, which correspond to the high thermal transport properties. Applying the proposed detuning procedures to other hybrid perovskites and studying the effects of the combination of substitutions leads to a wide variety of the thermal properties, which plays an important role to overcome the impending limits of the existing devices with simple crystalline materials.

In this wise, the standpoint of coupled vibrations is found to make easy to understand the mechanism of the thermal properties, with which the survey now suggests to utilize the hybrid structures for new materials with controllable thermal properties. While its fundamental mechanism in scattering phonons is similar as one of the phonon-glass, the hybrid design is distinguished for a large number of degrees of freedom for material design. The most novel contribution of this thesis is rather attributed to the development of the general approach to analyze and improve the thermal properties of such hybrid structures theoretically. The subsequent explorations would lead to practical materials with further controllability of thermal properties, when the proposed methodology should be a ladder of success. Finally, we will mark the next step here. The thermal design based on the hybrid structures strongly depends on the vibrational properties on the embedded organic molecules. It means that the larger degrees of freedom in the organic vibrations are expected to result in the more flexible control of the thermal properties, which requires the stable inorganic lattice with the large void spaces. Metal-organic frameworks (MOFs) are bright

candidates meeting such conditions. MOFs can contain macromolecules, and the void size can be controlled by organic ligands in addition to the host-guest interactions. The large flexibility of material design in MOFs itself also seems to make it possible to control the thermal transport in nanoscale devices.

PUBLICATIONS STEMMING FROM THIS WORK

[1] Hata, T.; Kawai, H.; Ohto, T. and Yamashita, K. (2013). Chirality dependence of quantum thermal transport in carbon nanotubes at low temperatures: A first-principles study. *J. Chem. Phys*. 139: 044711.

[2] Hata, T.; Kawai, H.; Jono, R. and Yamashita, K. (2014). Multi-wall effects on the thermal transport properties of nanotube structures. *Nanotechnology* 25: 245703.

[3] Hata, T.; Giorgi, G. and Yamashita, K. (2016). The Effects of the Organic–Inorganic Interactions on the Thermal Transport Properties of $CH_3NH_3PbI_3$. *Nano Lett.* 16: 2749-2753.

[4] Hata, T.; Giorgi, G.; Yamashita, K.; Caddeo, C. and Mattoni, A. (2017). Development of a Classical Interatomic Potential for $MAPbBr_3$. *J. Phys. Chem. C* accepted. DOI: 10.1021 /acs.jpcc.6b11298.